nks

Numerical analyses of a water pool under loadings caused by a condensation induced water hammer

Antti Timperi, Timo Pättikangas, Kim Calonius, Jari Tuunanen
Juha Poikolainen & Arja Saarenheimo

VTT Industrial Systems, Finland

March 2004

Abstract

Three-dimensional simulations of a rapidly condensing steam bubble in a water pool have been performed by using the commercial computational fluid dynamics (CFD) code Star-CD. The condensing bubble was modelled by using a mass sink in a single-phase calculation. The pressure load on the wall of the pool was determined and transferred to the structural analyses code ABAQUS. The analyses were done for a test pool at Lappeenranta University of Technology.

The structural integrity of the pool during steam experiments was investigated by assuming as a test load the rapid condensation of a steam bubble with a diameter of 20 cm. The mass sink for modelling the collapse of the bubble was determined from the potential theory of incompressible fluid. The rapid condensation of the bubble within 25 ms initiated a strong condensation water hammer. The maximum amplitude of the pressure load on the pool wall was approximately 300 kPa. The loads caused by the high compression waves lasted only about 0.4 ms. The loadings caused by larger bubbles or more rapid collapse could not be calculated with the present method.
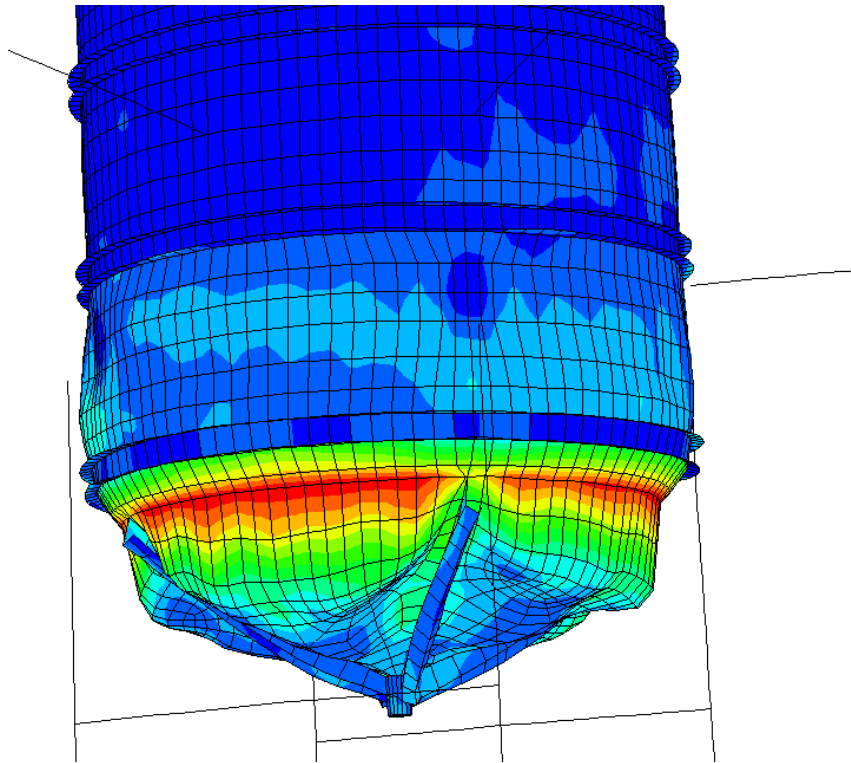
Key words

Condensing steam bubble, structural analysis, Star-CD, ABAQUS

NUMERICAL ANALYSES OF A WATER POOL UNDER LOADINGS CAUSED BY A CONDENSATION INDUCED WATER HAMMER

Foreword

Espoo

Authors

Table of Contents

Nomenclature

A	surface area
a	speed of sound in water $a = 1470$ m/s
$B(a,b)$	beta function
C	constant $C = 1,138 - 1,45$
D	diameter
d_t	diameter of blowdown pipe
E	internal energy of steam, Young's modulus
f	natural frequency of oscillating bubble
g	gravitational constant
h	enthalpy
$I_\mathrm{x}(a,b)$	incomplete beta function
l	length of blowdown pipe
M_s	steam mass
m	mass
Ma	Mach number Ma $= v/a$
p	pressure
p_∞	pressure in blowdown vessel
p_0	pressure far away from bubble
p_B	pressure on the bubble surface
Δp_B	pressure difference causing collapse of steam bubble
$\Delta p_\mathrm{F}(r,t)$	fluid pressure outside bubble at a large distance r from bubble center at time t
Q	volumetric flow rate
R	radius
r	radial position
$R(t)$	bubble radius at time t
R_0	initial diameter of bubble
R_p	inside radius of pipe
t	time
t_tot	total time of bubble collapse
V	volume
v	velocity
v_ave	average velocity of collapsing bubble surface $v_\mathrm{ave} = R_0/t_\mathrm{tot}$
W	flow work of system
x	position
$x(t)$	normalized bubble volume $x(t) = (R(t)/R_0)^3$

Greek symbols

Δ	difference
ε	strain
κ	gas constant $\kappa = 1.4$
μ	coefficient $\mu = 0.9147$
ν	Poisson ratio
ρ	density
σ	stress

Subindexes

d	bubble
i	interface
in	inlet
max	maximum
min	minimum
out	outlet at steam-water interface
p	plastic
pool	pool
s	steam
t	pipe
wall	inner wall of the pool

Abbreviations

CFD	computational fluid dynamics
fps	frames per second
FSI	fluid-structure interaction
FE	finite element
FEM	finite element method
LOCA	loss-of-coolant accident
MARS	monotone advection and reconstruction scheme
MDOF	master degree of freedom
MOI	method of image

1 Introduction

In light water reactors, it would be desirable to understand better the loads originating from the reactor pressure suppression pools. Large loads could occur, for instance, during a loss-of-coolant accident (LOCA) in a boiling water reactor where large amount of air and steam would be injected into the pressure suppression pool. The injection causes different kinds of pressure loads to the pool structures. Severe loads are caused by water hammers induced by rapidly condensing large steam bubbles. Such bubbles may in certain conditions occur near the outlet of the blowdown pipes as pure or nearly pure steam is injected into the pool.

Several extensive experiments have been performed, where the loads during blowdown of air and steam have been determined. In Marviken, full scale containment experiments were performed almost three decades ago (Anon, 1977). Recently, Meier (1999) performed small scale experiments with air and steam and developed a two-dimensional computational fluid dynamics (CFD) model. In this context, the first numerical models for the fluid-structure interactions were also developed already two decades ago. Giencke (1979, 1981) estimated the pressure distributions during a steam bubble collapse by using the potential theory of incompressible fluid. A numerical model for the suppression pool based on the volume of fluid (VOF) method was developed by Nichols and Hirt (1979). Models for the fluid-structure interaction were also developed by Huber et al. (1979) and Landram et al. (1982). A thermal-hydraulic model for the steam condensation was developed by Sargis et al. (1978).

Injection of air and steam into a water pool is investigated experimentally at Lappeenranta University of Technology in the POOLEX project of the SAFIR programme (Safety of Nuclear Power Plants – Finnish National Research Programme). In the first experimental series, air was injected into the pool through a vertical pipe submerged in water. Experimental and numerical simulation results of the tests with air are presented in Laine (2002), Pättikangas and Pokela (2003) and Calonius et al. (2003). In the second series, preliminary experiments with steam has been conducted.

Previously, two-dimensional CFD simulations of water hammer in the pool have been performed (Pättikangas et al., 2000; Raussi, 2001). Pressure load in a water pool caused by a closing valve was resolved. In addition, possibilities of modelling condensation induced water hammers with the aid of a mass sink were discussed. The two-dimensional pressure loads were transferred to axisymmetric structural analyses model, which was used for the analyses of stresses and strains of the pool (Saarenheimo et al., 2000).

In the present work, the behaviour of a rapidly condensing steam bubble in a water pool is investigated with three-dimensional CFD simulations. The simulations are carried out by performing a single-phase calculation, where the condensing steam bubble is modelled with a mass sink. The pressure loads due to the condensing bubble are transferred from the computational fluid dynamics code Star-CD to the structural analyses code ABAQUS (ABAQUS, 2002). The structural behaviour of the pool under the pressure transient is numerically solved with a three-dimensional finite element (FE) model. The main aim of this work is to solve numerically the behaviour of the pool in a case of a rapidly condensing steam bubble. Another goal is to ensure that the future experiments with injected steam at Lappeenranta University of Technology are safe and correctly instrumented before they are carried out. Some comparison of the numerical results with the preliminary tests is done.

The experimental set-up is described in Chapter 2. Chapter 3 contains a literature survey of alternative methods for calculating the blowdown of steam into the pool. The three-dimensional CFD simulation results are described in Chapter 4. The three-dimensional FE model and the results from different analyses are presented in Chapter 5. Chapter 6 contains discussion on the bi-directional fluid-structure interaction. Analyses of the results of the preliminary experiments are described in Chapter 7. Finally, Chapter 8 contains a summary and discussion on the results.

2   Experimental Set-up

In the POOLEX project of the Finnish Research Programme on Nuclear Power Plant Safety (SAFIR), injection of air and steam into a water pool is investigated experimentally at Lappeenranta University of Technology. The pool constructed for the experiments is illustrated in Figures 1 and 2. The experimental set-up is presented more thoroughly in Laine (2003).

Figures 3 and 4 show some details of the pool that have to be taken into consideration in the structural analyses.
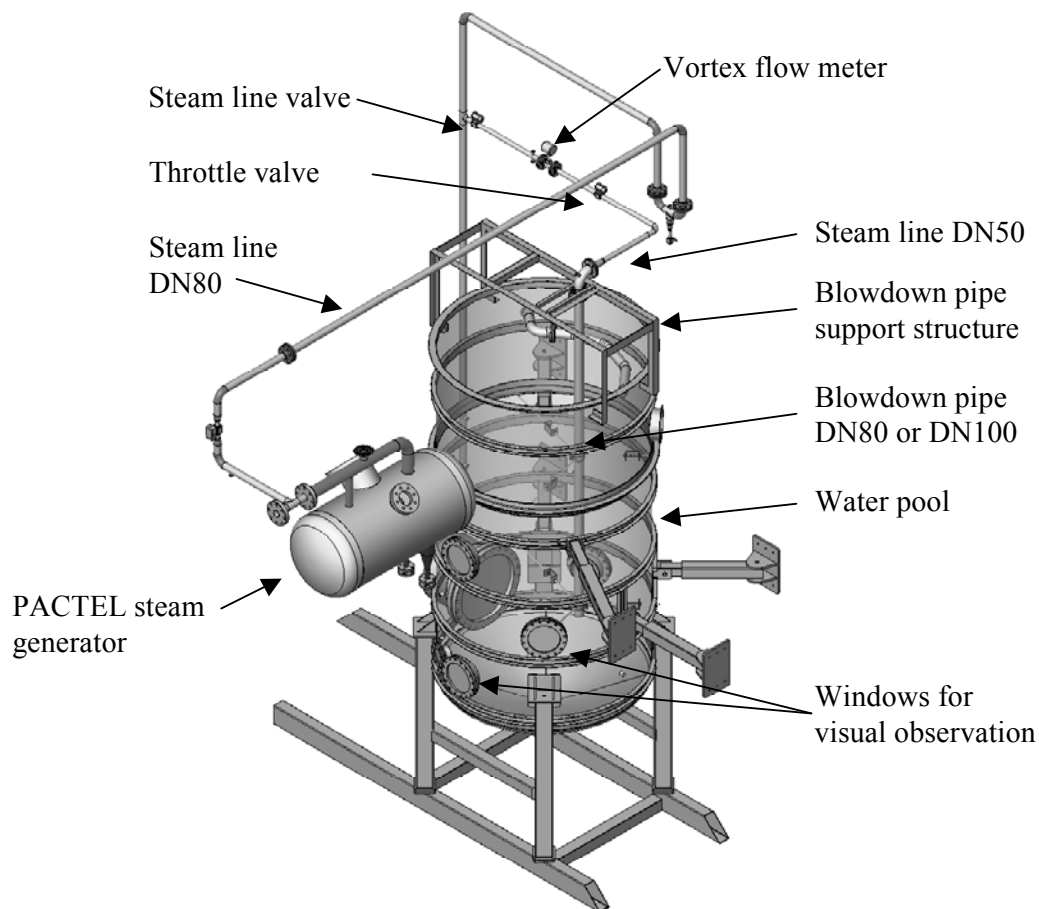
Figure 1. Experimental set-up in the POOLEX project at Lappeenranta University of Technology. The height of the pool is about 5 m and the diameter is 2.4 m. (Laine, 2003)

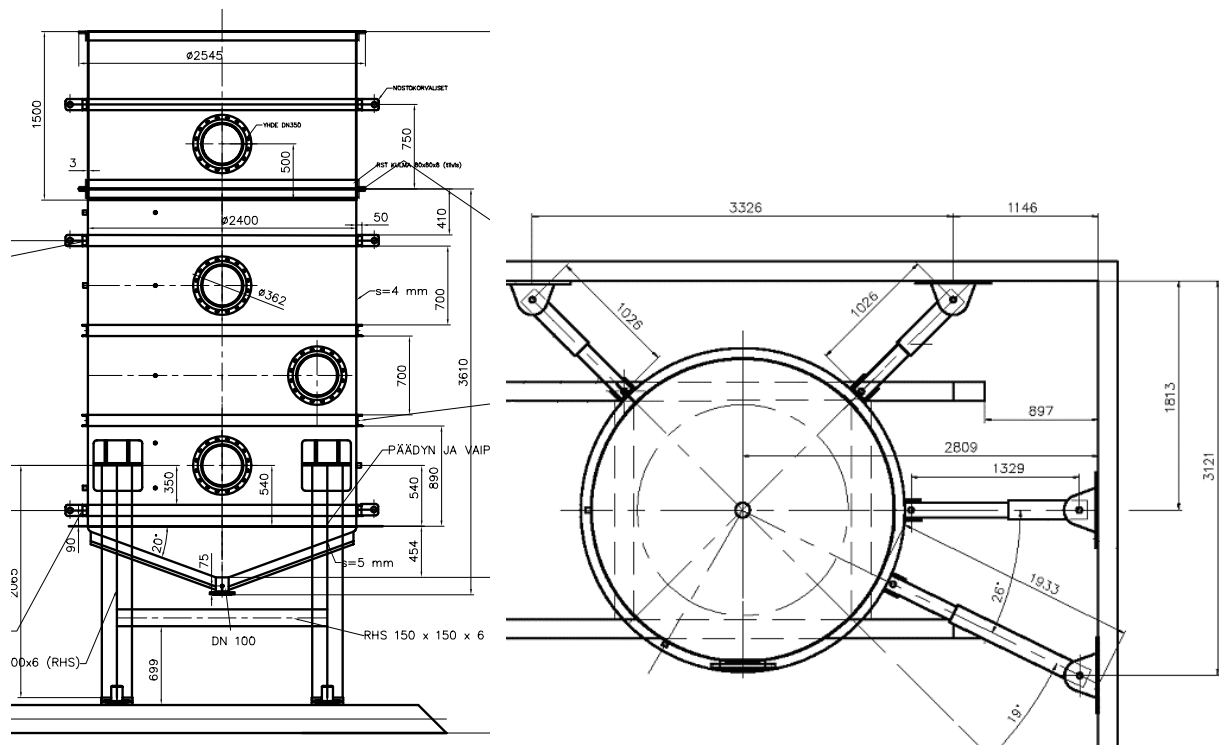*Figure 2. Construction of the pool in the POOLEX project at Lappeenranta University of Technology. On the right: the pool is supported to the concrete wall of the testing room by five lateral supports. (Laine, 2003)*

Figure 3. On the left: One of the five side stay joints on the concrete wall. On the right: U-profile bracing welded around the pool wall.

Figure 4. On the left: One of the four bearers that support the pool on the floor (notice the disc spring). On the right: The bearer is welded to the pool wall.

3 Alternative Methods for Calculating the Steam Blowdown

The purpose of the literature survey was to find alternative methods for calculation of blowdown of steam to a pressure suppression pool. The alternative methods are needed, when the reliability of the results of the CFD calculations are evaluated.

3.1 Bubble Size and Frequency

The simplest way to estimate the bubble size (volume) in a water pool during blowdown is to assume that the gas bubble is a sphere and to use the correlation

$$V_d = C \frac{Q^{1,2}}{g^{0,6}} \, , \tag{1}$$

where Q is the volumetric flow rate of gas (m^3/s), C is a constant between 1,138 – 1,45, and g is the acceleration of gravity (Davidson and Schüler, 1960). This correlation does not take into account the heat and mass transfer from the steam bubble surface, which in reality has significant effects on the bubble size.

Another way is to use the equation of Moody (1986), which gives an equation for bubble size D_d for large pipes

$$D_d = \frac{Q^2}{g D_t^4} \, , \tag{2}$$

where D_t is the diameter of the pipe.

In the case of chugging, an oscillating bubble is formed to the mouth of the pipe. The frequency of the oscillating bubble has to be estimated when calculating the loads to the pool

structures. In the thesis of Meier, an equation is presented for the natural frequency of the oscillating bubble (Meier, 1999):

$$f = \frac{1}{2\pi}\sqrt{\frac{\kappa p_\infty}{R_0 \rho} \cdot \frac{-3d_t^2 + 48R_0^2}{3d_t^2(l - R_0) + 16R_0^3}} \;,$$ (3)

where $\kappa = 1,4$ is the gas constant, p_∞ is the pressure in the blowdown vessel, d_t is the diameter of the blowdown pipe, l is the length of the blowdown pipe, R_0 is the reference diameter of the bubble and ρ is density.

$$R_0 = \left(\frac{3}{8\pi}V_d\right)^{1/3}$$ (4)

$$f = 0{,}8787 \frac{g^{0,6}}{Q^{0,2}}$$ (5)

3.2 Methods of Calculating the Pressure Field

If the pressure field in the pool during blowdown is calculated, the first alternative for calculation of steam or air blowdown to a water pool is to use the method of image (MOI). This method, together with the use of Green's function, is described in report of Wood and Sun (1980). The use of MOI -method requires information about the dynamics of the bubble (radius and pressure).

The second alternative for determining the pressure fields is to use programmes available from public sources, such as the OECD/NEA data-bank. Examples of these are PELE-IC (McMaster et al., 1979, 1979 and 1981; Gong et al., 1979) and KONDAS, which were developed already in 1970-1980. PELE-IC was written in FORTRAN. The characteristics of the programme are presented in Table 1.

PELE-IC was ordered from NEA data bank and tested. After modifications the programme worked, but the modules describing the steam condensation were missing. Hence, it turned out that it can't be used for the steam blowdown calculations.

Table 1. Characteristics of PELE-IC programme.

– Two-dimensional semi-implicit Eulerian hydrodynamics program for the solution of incompressible flow coupled to flexible structures
– Calculation of fluid-structure interactions and bubble dynamics of a pressure suppression system following a loss-of- coolant accident (LOCA)
– The solution strategy is to first solve the Navier-Stokes equations explicitly using values from the previous time-step.
– The pressure field is iterated upon until the incompressibility condition for each computational cell is satisfied within prescribed limits.
– The structural motion is computed by a finite element code from the applied pressure at the fluid-structure interface.
– The shell structure algorithm uses conventional thin-shell theory with transverse shear.
– The finite-element spatial discretization employs piecewise-linear interpolation functions and one-point quadrature applied to conical frustra. The Newmark implicit time integration method is used as a one-step module.
– The fluid code then uses the position and velocity of structure as boundary conditions.
– The fluid pressure field and the response of the structure are corrected iteratively until the normal velocities of fluid and structure are equal.
– The effects of steam condensation and oscillatory chugging on structures are calculated according to a simplified theory of condensation on a free surface due to C.S. Landram.

The third alternative is to use the equations from Sargis, Stuhmiller and Wang (1978).

Sargis et al. presented a thermal-hydraulic model to describe in a fundamental way the steam chugging phenomenon, which may occur in light water reactor pressure suppression pools. The model appeals to the basic conservation laws to describe each aspect of the process and the resulting formulation is therefore relatively free of empiricism. The schematic drawing of the method is presented in Figure 5.
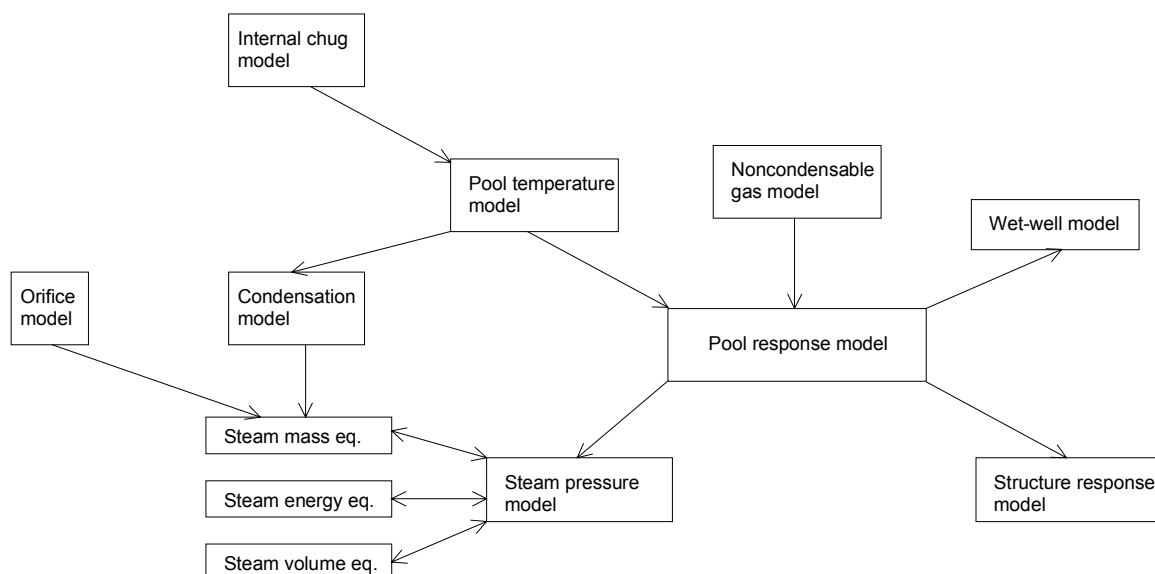

Figure 5. Schematic drawing of a chugging model.

The basic equations of the method are the conservation equation for steam mass

$$\frac{dM_s}{dt} = \dot{m}_{in} A_{in} - \dot{m}_{out} A_{out} - \dot{m}_{wall} A_{wall} \, , \tag{6}$$

the conservation equation for steam energy

$$\frac{dE}{dt} = -\frac{dW}{dt} + \dot{m}_{in} A_{in} h_{in} + \dot{m}_{out} A_{out} h_{out} + \dot{m}_{wall} A_{wall} h_{wall} \, , \tag{7}$$

and the conservation equation for the steam volume

$$\frac{dV_s}{dt} = \begin{cases} \pi R_p^2 v_i & x_i < x_p \\ & \\ \pi R_p^2 v_i + 2\pi (x_i - x_p)^2 v_i & x_i > x_p \end{cases} \, , \tag{8}$$

where M_s is steam mass (kg), $\dot{m}_{in}$, $\dot{m}_{out}$ and $\dot{m}_{wall}$ are the steam mass flux at the inlet, outlet and wall (kg/m^{2}s), A_{in}, A_{out} and A_{wall} are the inlet area, surface area of steam-water interface and surface area of downcomer wall (m^2), h_{in}, h_{out} and h_{wall} are the enthalpy of added steam mass at inlet, enthalpy of the steam mass at interface and enthalpy of steam mass condensing on downcomer walls (J/kg). E is the internal energy of steam (J/kg), W is the system flow work (J/kg). V_s is the volume of steam (m^3), v_i is the velocity of the interface (m/s), x_i is the interface position measured from the orifice plate, R_p is the inside radius of the pipe (m).

These equations, together with the equations for pool response, pool temperature distribution, wetwell pressure, wall pressure and structure response can be solved numerically. Examples of calculated and measured values are presented in Sargis et al. (1978).

Table 2. Additional references about steam bubble behaviour in the water pool.

Aya, I. & Nariai, H. (1987) *Boundaries Between Regimes of Pressure Oscillation Induced by Steam Condensation in Pressure Suppression Containment.* Nuclear Engineering and Design 99 (1987), 31-40.
Aust, E., Niemann, H.-R. & Schultheiss, G. F. (1987) *Simulation of Small Break LOCA Effects on BWR-Pressure Suppression Systems.* Nuclear Engineering and Design 102 (1987), 229-234.
Campos, F.B. Lage, P.L.C. *Heat and mass transfer modeling during the formation and ascension of superheated bubbles* (COPPE/UFRJ);
International Journal of Heat and Mass Transfer, v 43, n 16, May, 2000, p 2883-2894
Utamura, M. (1985) *Mechanism of Pressure Oscillation Due to Steam Condensation in Water.* Fluids Engineering Division, FED-Vol. 30, ASME 1985, 85-95.
Lee, C. K. B. & Chan, C. K. (1982) *Steam Chugging Analysis in Single-Vent Vapor Injection.* Heat Transfer 1982, Proceedings of the 7th International Heat Transfer Conference, Munich, Germany, v 4, 3-7.
Steam bubble formation and detachment at a submerged orifice in sub-cooled water, Proc. of 9th Int. Heat Transfer Conf., 1990, Jerusalem, Vol.6, pp101-106
BASHIR H.A. "*The formation and detachment of steam bubbles formed at submerged orifices in sub cooled water*" Phd thesis, Energy Systems Division, Department of Mechanical Engineering, University of Strathclyde, 1996
Kusunoki, T., Kikushima, K. & Nariai, H. (1997) *Vapor Condensation in Subcooled Water at Large Vapor Mass Flux.* 5th International Topical Meeting on Nuclear Thermal Hydraulics, Operations and Safety (NUTHOS-5), Apr. 14-18, 1997, Beijing, China, KK3-1 - KK3-6.
Available from China Nuclear Information Centre
A Model for Steam Bubble Formation in Flowing Subcooled Water by WB Chen and RBH Tan, CHEMECA 2000 Opportunities and Challenges for the Resources and Processing Industries, 9-12 July 2000, Perth, Western Australia.

4 Wall Loading Caused by a Large Collapsing Steam Bubble

It would be desirable to analyse the collapse of a large steam bubble by using a proper two-phase model for the mixture of steam and water. The commercial CFD codes contain two alternative models that could potentially be used for modelling of the large collapsing steam bubbles: the volume of fluid model and the Eulerian two-phase model. The volume of fluid method was previously used for modelling injection of large air bubbles in a water pool (Pättikangas and Pokela, 2003). After testing the phase change models of the current volume of fluid models of Fluent and Star-CD, the more simple single-phase approach was chosen for the present work.

The collapsing steam bubble was modelled with a single-phase calculation, where the collapsing bubble was modelled with a mass sink. The mass sink was estimated from an analytical model describing the collapse of a large steam bubble in an infinite water pool. The pressure wave caused by the water hammer induced by the bubble collapse is resolved and used as load in the structural analyses in the following sections.

4.1 Collapse of a Steam Bubble

We first review some main features of a large collapsing steam bubbles. The special case of a spherical bubble in an infinite fluid was already solved by Rayleigh by using the potential theory of an incompressible fluid (Lamb, 1975; Pättikangas et al., 2000). We consider a spherical steam region initially of radius R_0 in an infinite region of water with a density ρ. The pressure difference causing the collapse is assumed to be constant: $\Delta p_B = p_0 - p_B$, where p_0 is the pressure far away from the bubble and p_B is pressure on the bubble surface.

The equation of motion for the surface of the bubble is integrated by using the potential of the flow velocity. It is found that the bubble surface collapses with the velocity

$$\dot{R}(t) = -\left(\frac{2\Delta p_B}{3\rho}\right)^{1/2}\left(\frac{R_0^3}{R(t)^3} - 1\right)^{1/2},$$
(9)

where $R(t)$ is the radius of the bubble at time t and $\dot{R}$ stands for the time derivative. The radius of the bubble is determined by

$$t = R_0\left(\frac{\rho}{6\Delta p_B}\right)^{1/2} B(\frac{5}{6},\frac{1}{2})[1 - I_x(\frac{5}{6},\frac{1}{2})],$$
(10)

where $B(a,b)$ is the beta function, $I_x(a,b)$ is the incomplete beta function (Abramowitz and Stegun, 1972) and the normalised bubble volume is $x(t) = (R(t)/R_0)^3$. The total time of collapse is

$$t_{tot} = \mu R_0\left(\frac{\rho}{\Delta p_B}\right)^{1/2},$$
(11)

where $\mu \approx 0.9147$. The average velocity of the collapsing bubble surface is $v_{ave} = R_0/t_{tot}$. Note that the average velocity does not depend on the initial radius of the bubble.

The mass flux at the surface of the bubble is

$$\dot{m}(t) = -4\pi\left(\frac{2}{3}\Delta p_B\rho\right)^{1/2} R(t)^{1/2}\left(R_0^3 - R(t)^3\right)^{1/2}.$$
(12)

The main features of the collapsing bubble are illustrated in Figure 6, where a bubble having initially a radius of $R_0 = 10$ cm is considered. The radius collapses to the value zero within a time of $t_{tot} \approx 25$ ms. When the radius of the bubble decreases, the velocity of the surface increases. The velocity approaches infinity when the radius approaches zero. This non-

physical divergence is caused by the assumption of an incompressible fluid, which becomes invalid roughly when the Mach number Ma $= v/a$ becomes larger than 0.3, i.e., $v > 440$ m/s.

The mass flux at the surface of the bubble is shown in Figure 6(c). The mass flux has its maximum value when the radius of the bubble is $R = R_0/4^{1/3}$. This corresponds to the volume of the bubble of $V = V_0/4$.

In the following, a rapid condensation of a steam bubble is modelled with a single-phase calculation by applying the mass sink of Equation (12) into the water pool. The mass sink shown in Figure 6(c) is applied inside the bubble with the radius shown in Figure 6(a). This produces the flow velocity shown in Figure 6(b) through the "surface" of the bubble.

Usually, the steam contains at least some amount of air. The amount of non-condensable gas determines the minimum size that the bubble can achieve. In the following, we assume that the steam contains 0.8 % of air, which means that the minimum radius of the bubble is $r_{min} = 2$ cm. The presence of air also removes the divergence in the velocity of the bubble surface.

The pressure transient caused by the collapsing bubble consists of two different phases (Giencke, 1981). The early phase of the collapse consists of a fairly long period of under pressure, which pushes water into the region of the bubble. At the end of the collapse, a rapid over pressure occurs because water flowing into the centre of the bubble is stopped rapidly when the bubble is filled.
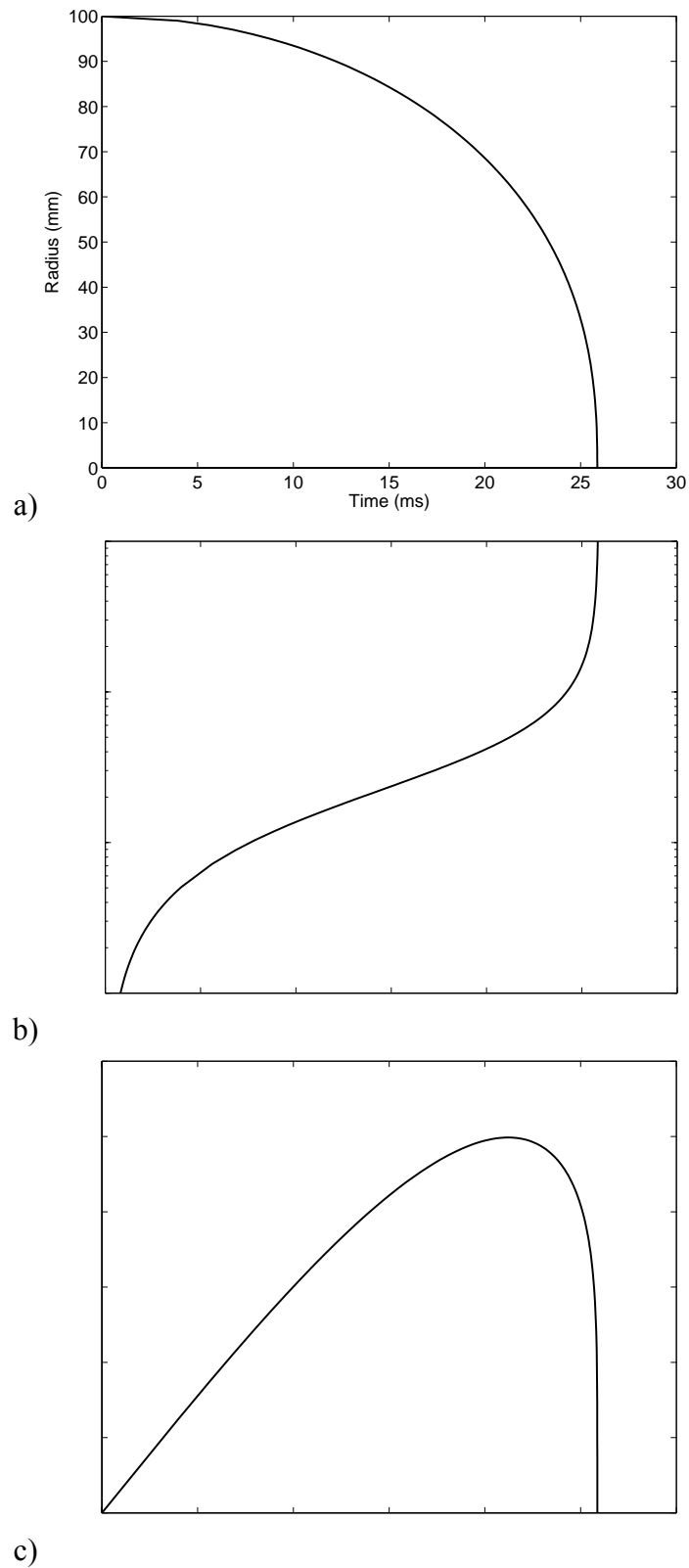
a)

b)

c)

Figure 6. Collapse of a spherical bubble in an incompressible fluid when the bubble pressure is assumed constant $\Delta p_B = 12.5$ kPa. (a) Radius of the bubble. (b) Velocity of the surface of the bubble. (c) Mass flux at the surface of the bubble ($\rho = 1000$ kg/m^3).

4.2 Results of CFD Simulations

In the following, simulation results for a condensation water hammer caused by a collapse of a large steam bubble are presented. The rapid condensation of the bubble is modelled with the mass sink located just below the lower end of the steam pipe at $x = 0.3$ m, $y = 0$ and $z = 0.90$ m. In this calculation, the water level is at $z = 2.87$ m. The speed of sound in water is $a = 1470$ m/s.

The simulation was performed with the commercial Star-CD code, version 3.150A, which can handle the rapid pressure transients during the water hammer. The motion of the wall was ignored in the flow simulation and pressure boundary condition was used at the water surface. The numerical mesh had about 80 000 grid cells. The monotone advection and reconstruction scheme (MARS) was used for discretisation of the momentum equations. The Crank-Nicholson method was used for the temporal discretisation with the time step of 0.005 ms.

The flow velocity during the collapse of the bubble is illustrated in Figure 7. The mass sink modelling the collapse makes the water flow towards the bubble centre with increasing velocity. At $t = 9$ ms, the maximum flow velocity is about 0.9 m/s. The flow velocity towards the centre of the bubble increases achieving the value of 6 m/s at time 21 ms. At the end of the collapse, the flow velocity decreases rapidly.

The relative pressure during the collapse of the bubble is shown in Figure 8. In the early phase of the collapse, an under pressure occurs near the bubble, which is evident at time $t = 5$ and 9 ms. A hint of the pipe submerged into the pool can be seen above the collapsing bubble. At time $t = 14$ ms, a spherical wave with over pressure emerges around the collapsing bubble. This spherical wave hits the pool wall less than a millisecond later and traces of it can still be seen at $t = 15$ ms.

The under pressure is strongest roughly at time $t = 21$ ms after which the over pressure stage starts. The bubble radius reaches its minimum value $r_{min} = 2$ cm, and the water flowing towards the bubble centre rapidly slows down. A spherical compression wave is initiated, and can be seen at time $t = 21.8$ and 22.0 ms. The wave hits the pool wall at time $t = 22.4$ ms and reflections of it can still be seen at 23.0 ms.

The wall loading caused by the condensation water hammer is shown in Figure 9. At time $t = 15.0$ ms, an over pressure wave hits the pool wall with an amplitude of 90 kPa. At the end of the collapse, $t = 22.4$ ms, a higher amplitude compression wave hits the wall. The maximum amplitude of this pressure wave is about 300 kPa. The loads caused by these compression waves only last for a very short time, about 0.4 ms.

The pressure loading of the pool wall was transferred from Star-CD to ABAQUS for structural analyses. Since the mesh used in the CFD calculation is different from the structural analyses mesh, the pressure load had to be interpolated from the CFD mesh to the structural analyses mesh. The interpolation was performed with the in-house interpolation tool D2A previously written for this purpose (Silde and Pättikangas, 2001). The interpolation tool has previously been used with DET3D and Fluent codes. In this work, the necessary enhancements were written and tested so that D2A can also be used with Star-CD. The technical details of transferring the pressure load from Star-CD to ABAQUS are described in the Appendix.
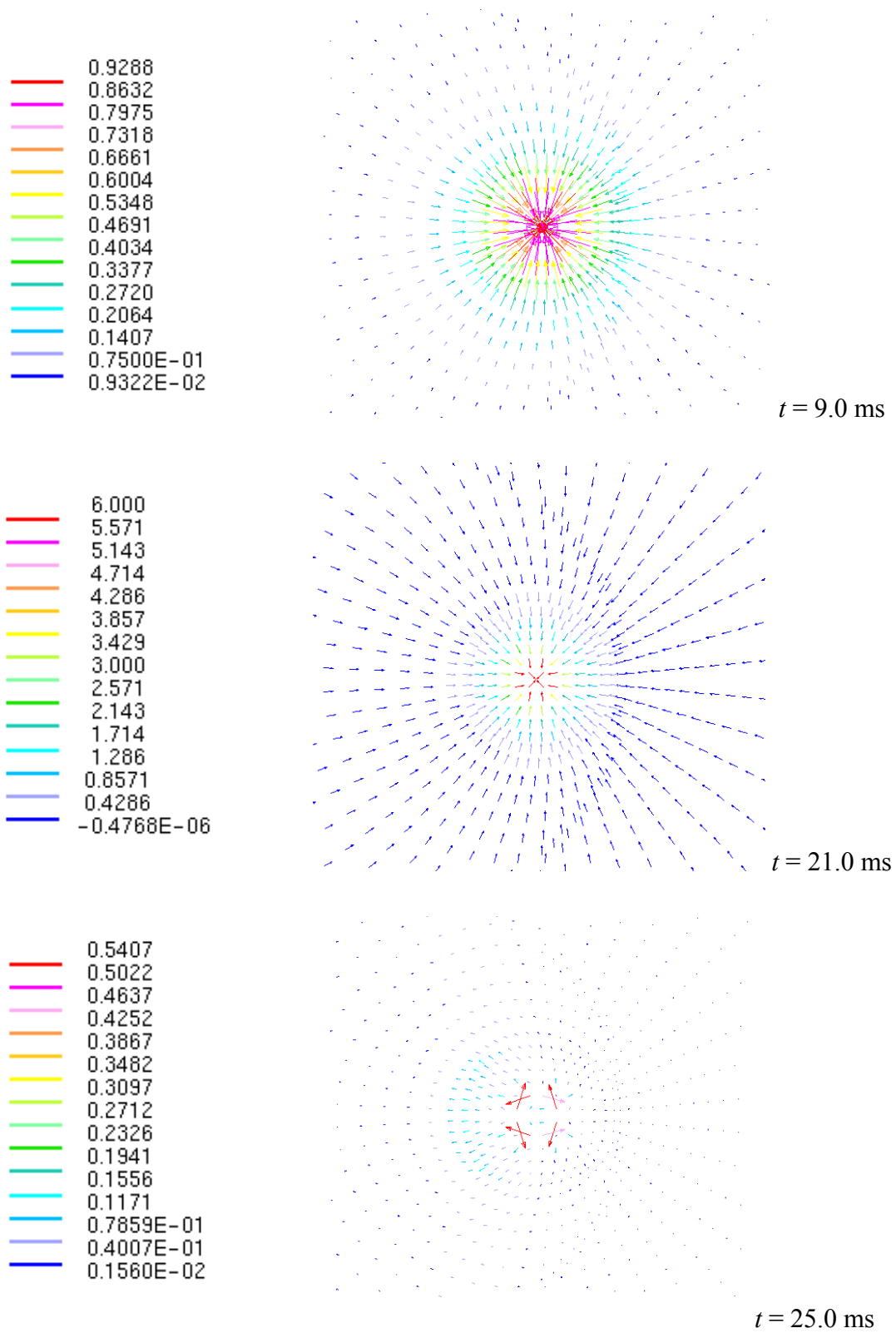
Figure 7. Magnitude of flow velocity (m/s) during the collapse of the void bubble at different instants of time.
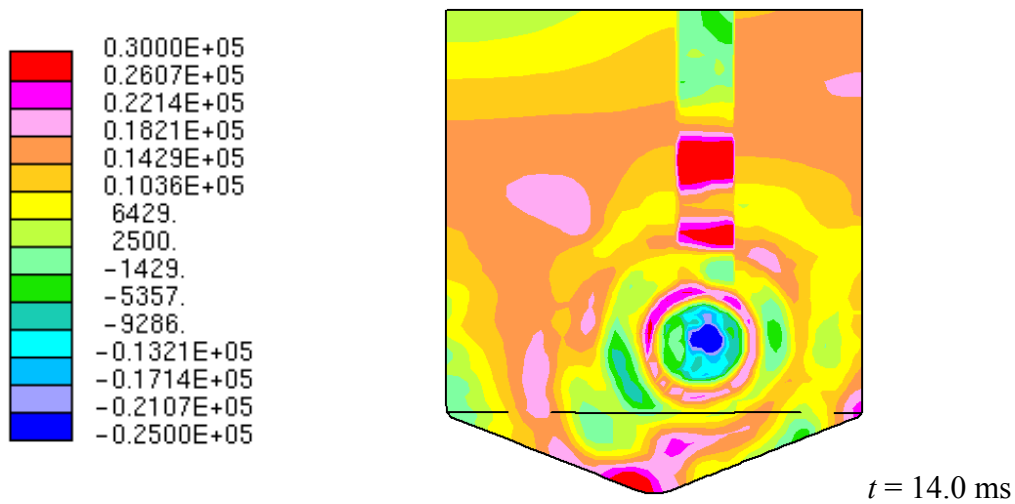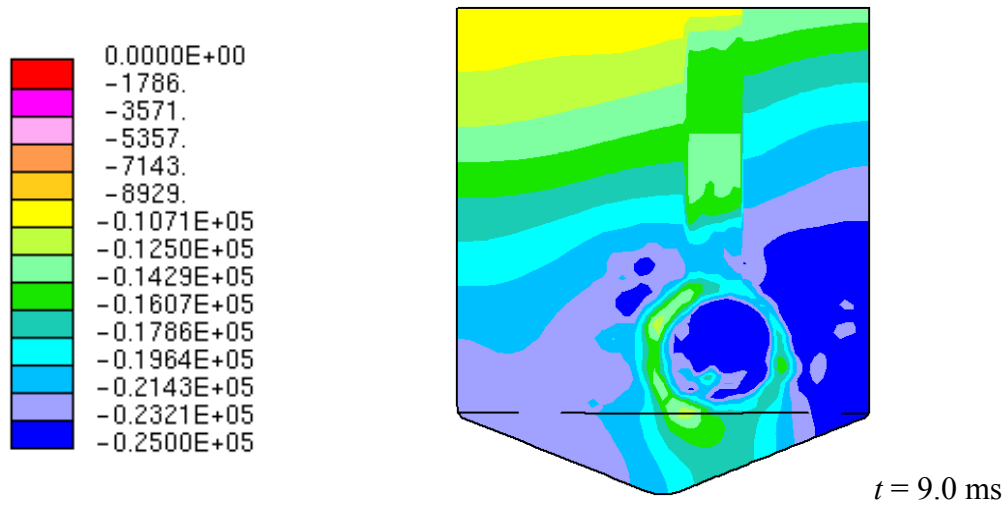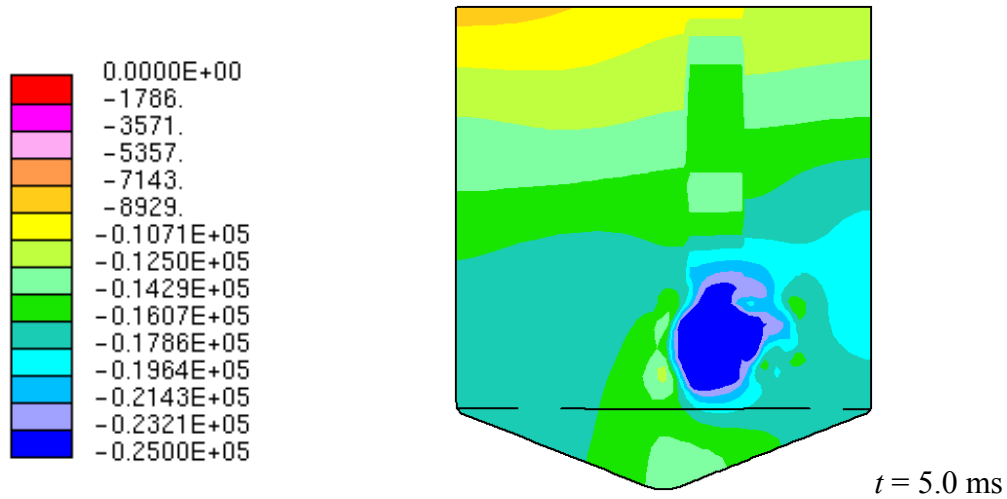
Figure 8. Relative pressure (Pa) during the collapse of a void bubble at different instants of time. The hydrostatic pressure and the atmospheric pressure are not included in the values shown (Continues on the following pages).
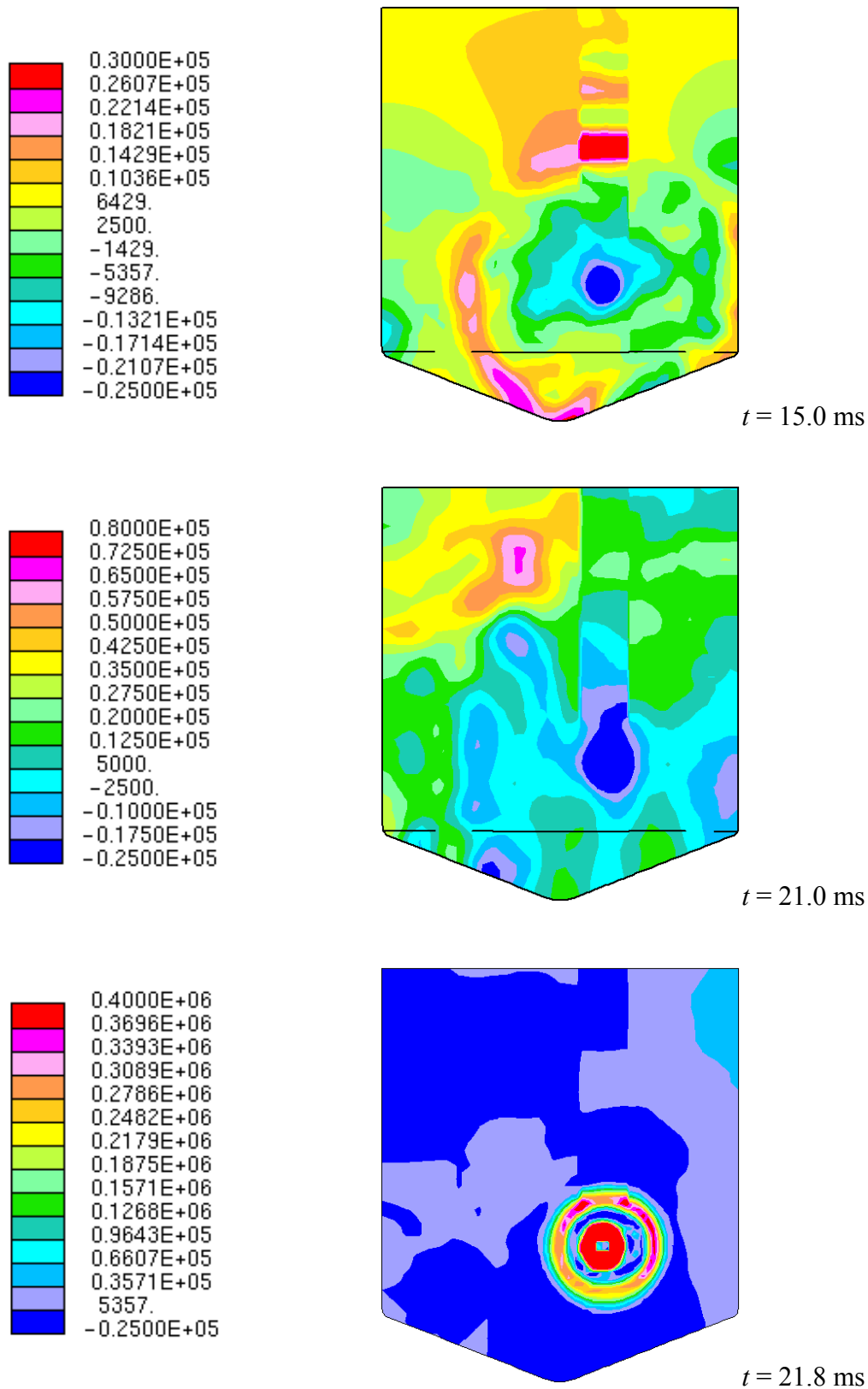
t = 15.0 ms

t = 21.0 ms

t = 21.8 ms

Figure 8. Continues from the previous page.
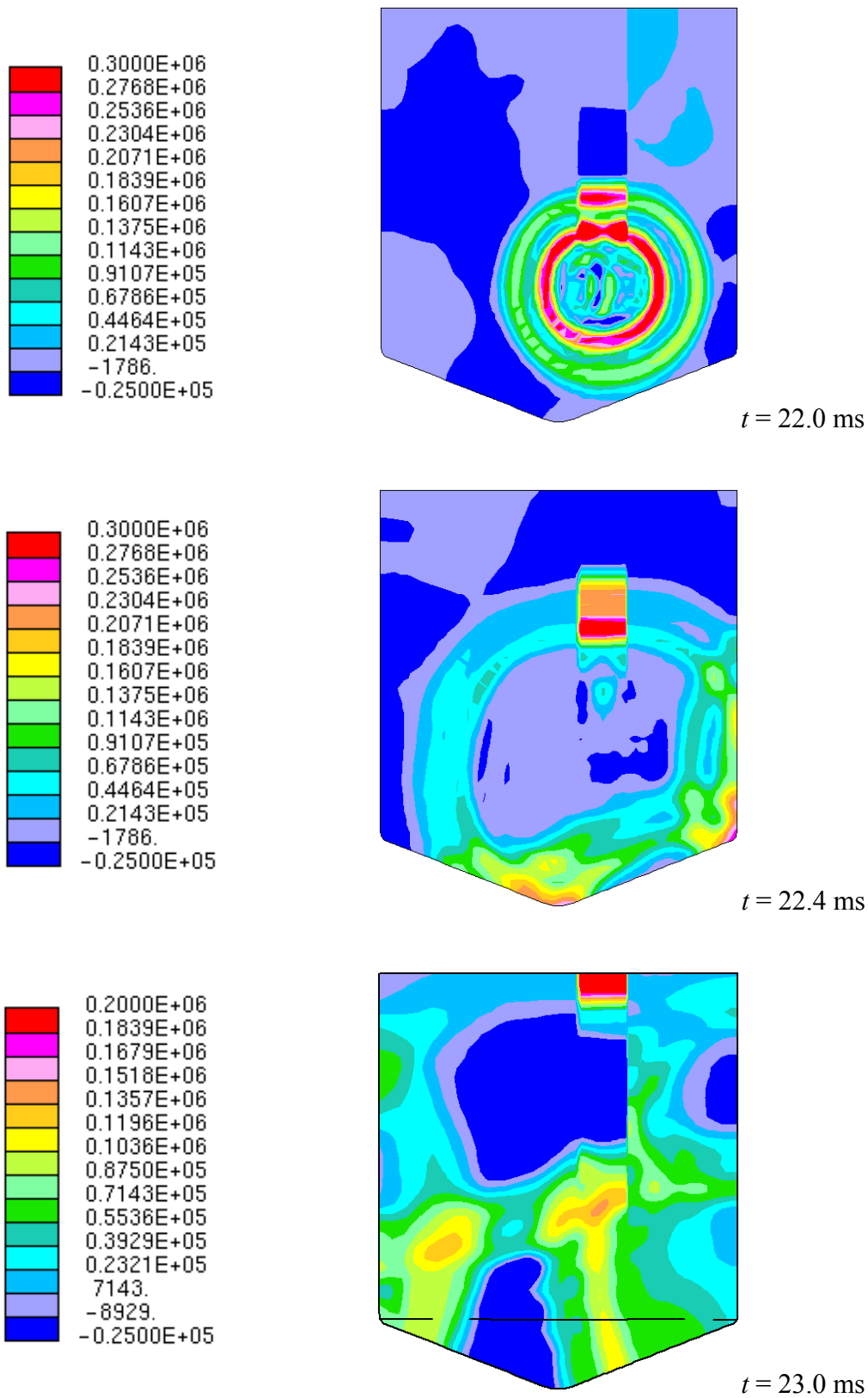
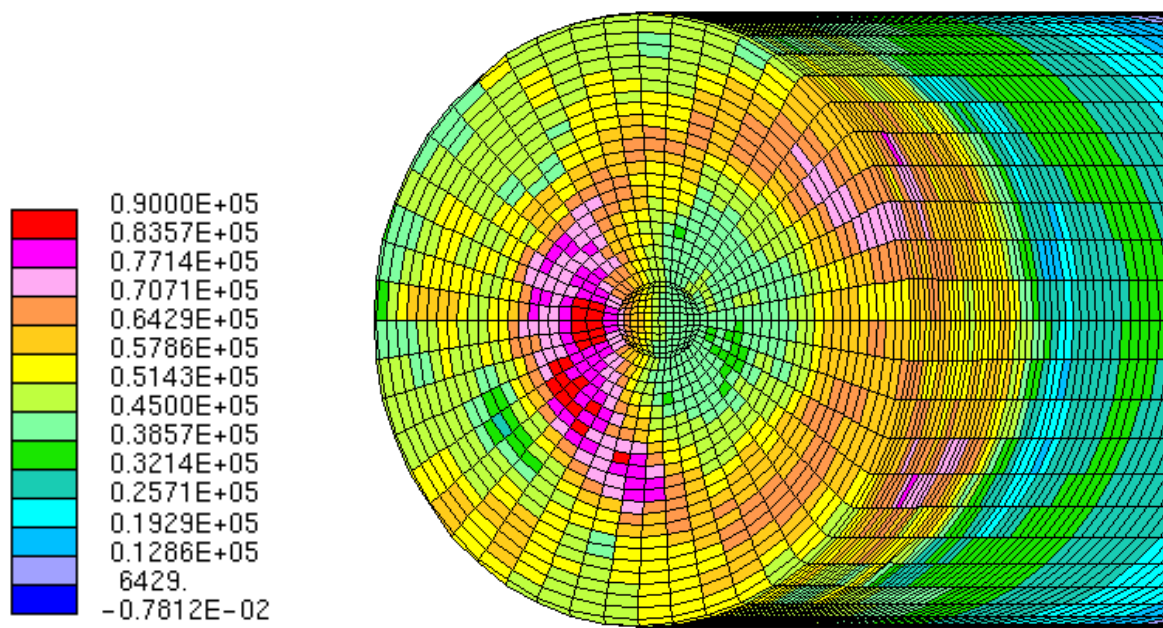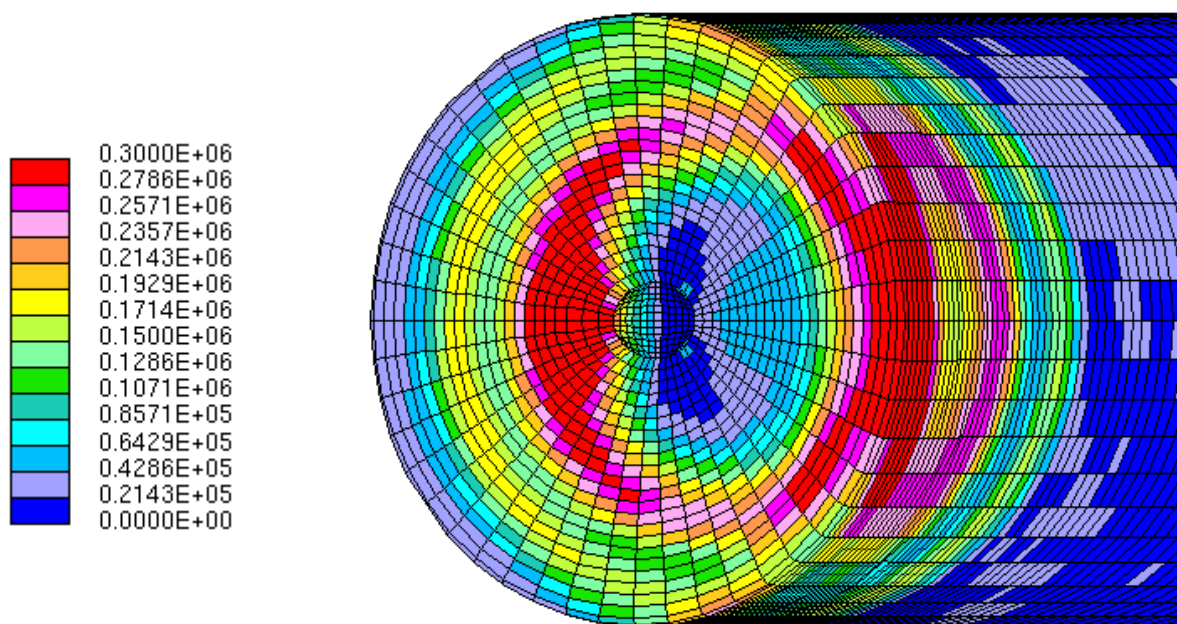t = 22.0 ms

t = 22.4 ms

t = 23.0 ms

Figure 8. Continues from the previous page.

t = 15.0 ms

t = 22.4 ms

Figure 9. Wall loading (Pa) at two different instants of time.

4.3 Discussion on the CFD Results

It is instructive to compare the simulation result to the analytical solutions of the pressure in an infinite water pool. An approximate solution for the fluid pressure outside the bubble at a large distance r from the bubble centre is (Lamb, 1975; Giencke, 1981)

$$\Delta p_{\mathrm{F}}(r,t) = p(r,t) - p_0 = \frac{R}{r}\left(\frac{1}{2}\rho\dot{R}^2 - \Delta p_{\mathrm{B}}\right).$$ (13)

In the early phase of the collapse, the fluid pressure has the value $\Delta p_{\mathrm{F}} = -\Delta p_{\mathrm{B}}\, R/r$. In the final phase of the collapse, the fluid pressure is determined by the kinetic energy term $(1/2)\rho\dot{R}^2$ which increases rapidly.

In Figure 10, the fluid pressure in an infinite pool is shown at two different distances from bubble centre. In the early phase of the CFD simulation, the magnitude of under pressure is somewhat larger than in the analytical result for the infinite pool. This is because in the finite pool of the simulation, the fluid removed by the collapsing bubble can not be replaced as easily as in an infinite pool.
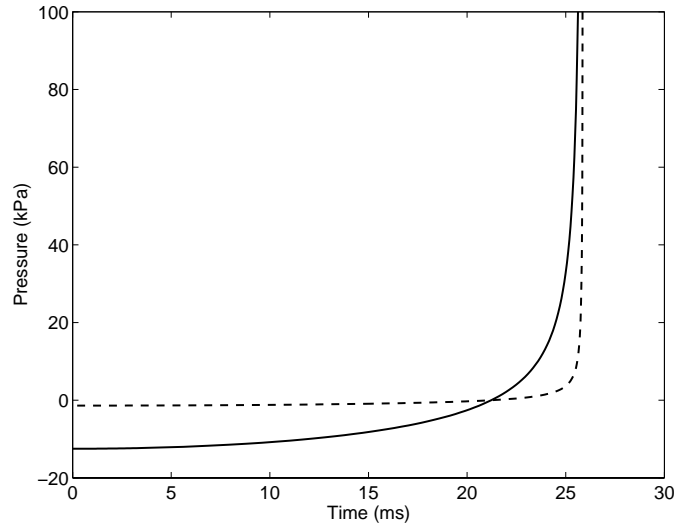

Figure 10. Fluid pressure (kPa) in an infinite water pool at two different distances from the centre of the collapsing bubble: r = 0.1 m (solid line) and r = 0.9 m (dashed line).

In the late phase of the CFD simulation, the pressure increases rapidly as is expected from the analytical result. In the simulation, the maximum value of the pressure is $p_{\mathrm{max}} = 16.4$ MPa in the centre of the collapsing bubble at time $t = 21.6$ ms. The maximum value occurs in a region having a radius of $r_{\mathrm{min}} = 2$ cm. The wall is at the distance $r = 0.9$ m from the bubble centre. According to Equation (13), the wall pressure should be $p_{\mathrm{wall}} = p_{\mathrm{max}}\, r_{\mathrm{min}}\,/\,r$, which leads to the estimate $p_{\mathrm{wall}} = 360$ kPa. This is quite close to the value found in the simulation (see Fig. 9).

The maximum flow velocity at the end of the bubble collapse can also be estimated from Equation (13). The maximum velocity is $v_{\mathrm{max}} = (2\, p_{\mathrm{max}}\,/\rho)^{1/2}$, which gives the result $v_{\mathrm{max}} = 180$ m/s. This is still in the validity region of the potential theory model for the collapsing bubble.

The present analyses has the pressure difference causing the collapse as the fit parameter, which in the analyses above had the value $\Delta p_B = 12.5$ kPa. The approximation for the fluid pressure in Equation (13) shows that the value of the pressure difference affects the result only in the early phase of the bubble collapse. Later the result is dominated by the kinetic energy term in Equation (13). The pressure difference affects, however, the total time of collapse as can be seen in Equation (11). A higher pressure difference would lead to somewhat faster collapse.

The effect of the finite pool size on the pressure load has been investigated by Antony-Spies (1979) and Giencke (1981). The finite size of the pool does not affect the collapse of the bubble if the size of the bubble is much smaller than the size of the pool, i.e., if $R_0 / R_{pool} \ll 1$. The results suggest that the finite size of the pool affects the wall loading in the simulation discussed above. Especially, in the under pressure phase of the bubble collapse the magnitude of the fluid pressure is larger than it would be in an infinite pool. In a finite pool, the collapse time of the bubble should also be longer than in an infinite pool. Giencke (1981) has suggested a method for taking into account the effect of the pool size on the collapse time.

In the present work, the constant bubble pressure assumption of Rayleigh has been used (Lamb, 1975). Experimental results suggest, however, that the assumption of a linear bubble pressure $p \sim t$ could be a better approximation (Giencke, 1981). The assumption of linear bubble pressure also leads to a longer collapse time than the assumption of constant pressure. However, the slope of the linear correlation for the bubble pressure has to be determined experimentally.

5 FE Analyses

The structural analyses are conducted with finite element method (FEM). A complex three-dimensional structural model is used. The FE analyses are conducted with ABAQUS Version 6.3 (ABAQUS, 2002).

5.1 Material Properties

Three different materials are used in the pool and its supporting structures. The pool itself and the L-profile stiffening the upper edge of the pool are stainless steel SS2333, the U-profile bracings around the pool are normal steel S235JRG2 and the rectangular beams are normal steel S355J2H. The material properties at different temperatures are listed in Tables 3 and 4.

Table 3. Elastic material properties at different temperatures. [GPa]

	SS2333		S355J2H		S235JRG2	
T	E	ν	E	ν	E	ν
25	200	0.3	206	0.3	206	0.3
100	195	0.3	-	-	-	-
200	185	0.3	-	-	-	-

Table 4. Plastic material properties at different temperatures. Stress and corresponding plastic strain. [MPa]

	SS2333		S355J2H		S235JRG2	
T	σ	ε_p	σ	ε_p	σ	ε_p
25	200	0	315	0	195	0
25	210	0.002	325	0.002	205	0.002
25	240	0.01	355	0.01	235	0.01
100	137	0	295	0	180	0
100	147	0.002	305	0.002	190	0.002
100	163	0.01	325	0.01	210	0.01
200	113	0	256	0	165	0
200	123	0.002	265	0.002	175	0.002
200	137	0.01	275	0.01	185	0.01

5.2 FE Model

A complex model with different element types was created for three-dimensional structural analyses. The geometry of the model corresponds relatively accurately to the real pool and its supporting structures. An elastic-plastic material model with von Mises yield function and isotropic yield hardening was adopted. The material properties are presented in Chapter 5.1.

The dynamic FE analyses presented in this chapter are divided into three cases listed in Table 5. The first two cases are either with (Case 2) or without (Case 1) the mass of water included in the density of the pool wall. In Case 3 the vertical displacement of the lower ends of the four vertical supports are fixed to examine the effect of the disc springs under them, in this case the mass of water is not included. Since some mass should be added to the pool wall to account for the inertia of the water, the results from Case 1 and 2 are compared with each other to show the effect of the added mass. Case 1, without the mass of water, is assumed to be a better approximation during a single pressure impact.

Table 5. Different cases of the dynamic analyses.

CASE	MASS OF WATER	SPRINGS
1	no	yes
2	yes	yes
3	no	no

5.2.1 Mesh and Boundary Conditions

The pool is meshed with 4-node doubly curved general-purpose shell elements with finite membrane strains, triangular 3-node finite membrane strains shell elements are used in some few necessary locations. Reduced integration with hourglass control is used except in the case of the bracing rings, where full integration is employed. The size of the shell elements is on the average 50×50 mm. Every node has six active degrees of freedom - three translational and three rotational.

The beams are meshed with 2-node linear beam elements. The length of the elements is 100 mm. The nodes have six active degrees of freedom.

Number of elements in the whole model is 6585, number of nodes is 7310 and total number of variables in the model is 39828. The pool mesh and a detailed picture of the pool bottom mesh are shown in Figure 11. The effect of mesh refinement at pool bottom is presented in Chapter 5.4. Notice: the two horizontal beams in the middle of the four vertical supports in Fig. 11 are situated to the adjacent gaps in the real structure, see also Fig. 1.

The upper ends of the vertical supports are fully fixed to the pool surface at an area corresponding to the welded plates of the real structure. The vertical supports are also fixed with two nodes of the lowest pool bracing at corresponding locations. Constraints between the side stay ends and pool vary from pinned (translations fixed, rotations free) to fully fixed.

The disc springs under the supports are modelled with nonlinear springs. The force-displacement values for the springs according to SMS 2313 DIN 2093 No 4444 are shown in Table 6. Only horizontal translations of the support ends are fixed at the location of the springs in Case 1 and 2, in Case 3 also vertical translation is fixed. Translations of the outer ends of the side stays are fixed with all rotations free.
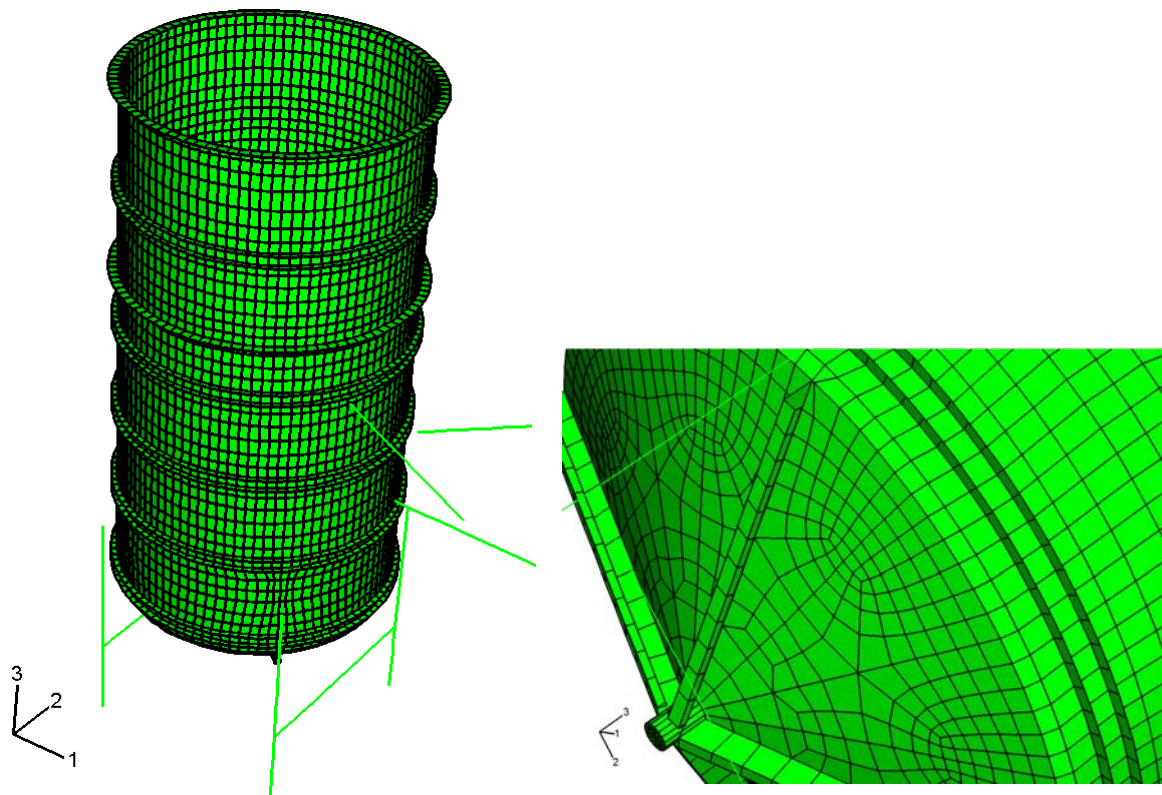

Figure 11. The pool mesh and the supports. On the right: a detail of the pool bottom mesh, notice the stiffening bracings.

Table 6. Force-displacement values of the disc springs (SMS 2313 DIN 2093 No 4444).

FORCE [kN]	DISPLACEMENT [mm]
58.756	1.4
106.099	2.8
145.357	4.2
194.014	6.2

5.2.2 Loads

The transient inner wall pressure presented in Chapter 4 was transferred from the CFD calculation to ABAQUS structural analyses code. Interpolation of the inner wall pressure to the structural analyses mesh was performed using the in-house D2A interpolation programme (Silde and Pättikangas 2001). The motion of the pool wall was not taken into account in the CFD calculation, i.e., mesh on the coupling surface did not move during the simulation. The data file written by the interpolation programme contains the transient pressure load on each element of the ABAQUS mesh on the coupling surface. The transferring of the pressure load from Star-CD to ABAQUS is described more closely in the Appendix.

Figures 13 and 14 show the pressures written by the interpolation programme for input to ABAQUS for elements 1, 256 and 492 of the pool mesh (hydrostatic pressure included). Locations of these three elements can be seen in Figure 12. The time interval between the pressure values in the input file is 10 µs (see Fig. 14).
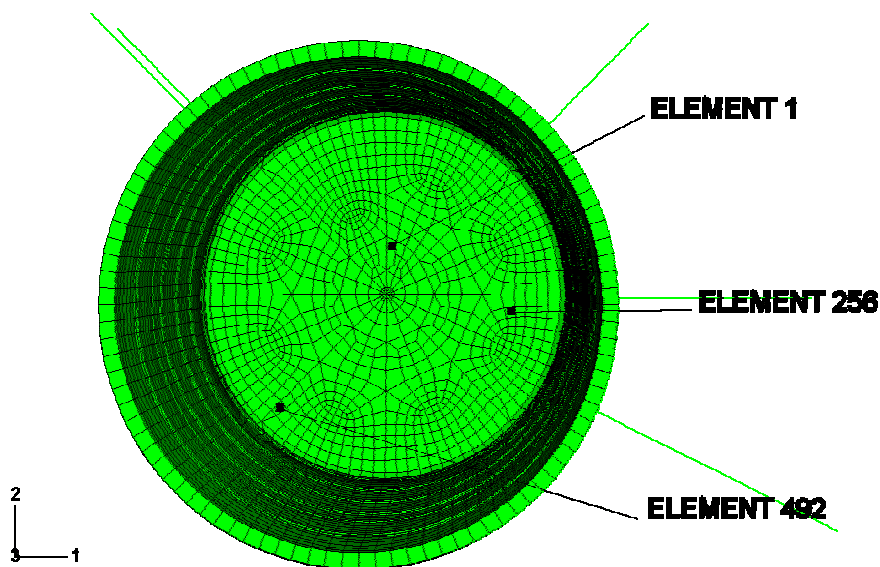

Figure 12. Locations of pool mesh elements 1, 256 and 492.
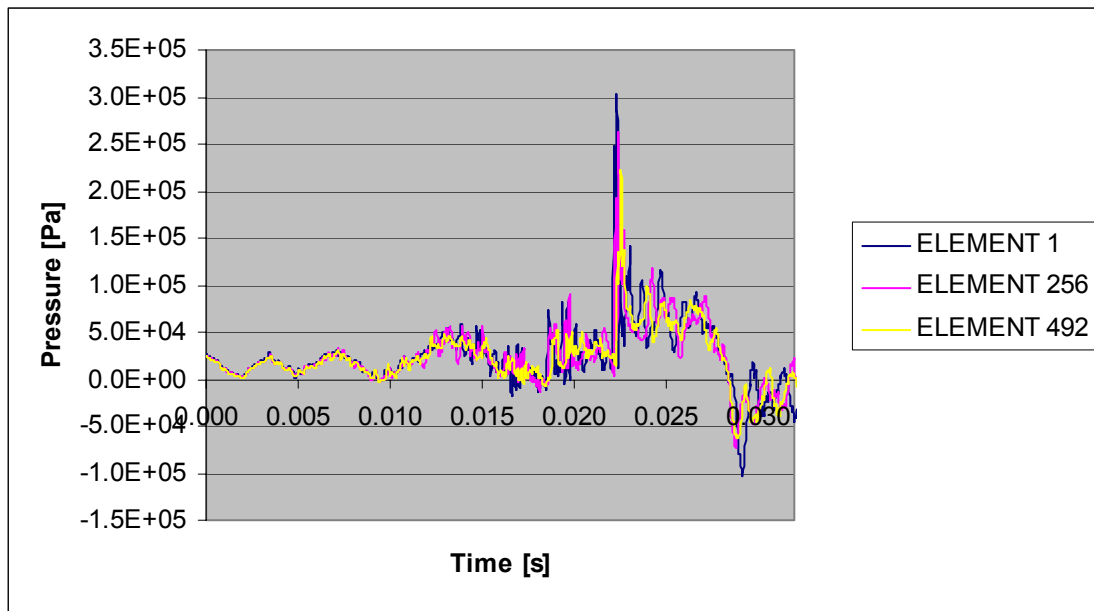
Figure 13. Pressures transferred from CFD analyses as a function of time for pool mesh elements 1, 256 and 492 (hydrostatic pressure included). Maximum pressure is approximately 310 kPa.
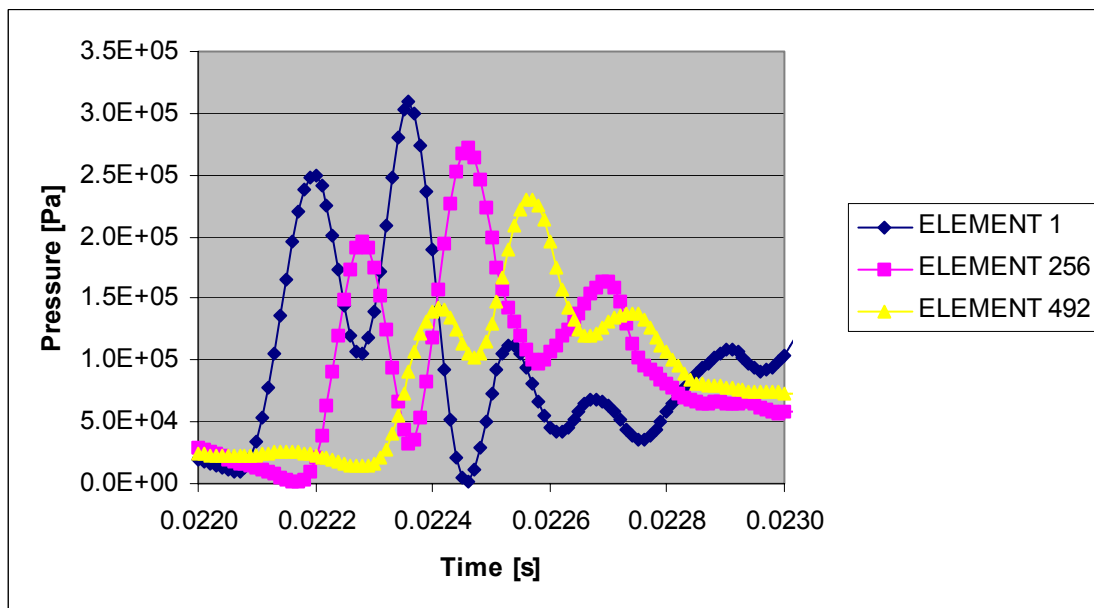

Figure 14. Pressures transferred from CFD analyses as a function of time for pool mesh elements 1, 256 and 492 during period 22 - 23 ms (hydrostatic pressure included). The dots represent the distinct pressure values at different instances of time (interval 10 μs). Maximum pressure is approximately 310 kPa.

5.3 Eigenvalue Extraction

The eigenvalue extraction is done for two structural models, Case 1 (without mass of water) and Case 2 (mass of water included).

In Case 1 the total mass of the model is 2455 kg. Table 7 shows the first 15 eigenfrequencies for the structure, the lowest frequency is approximately 12 Hz. Figures 15 - 22 show the undeformed shape and selected eigenmodes of the structure in Case 1. Notice the mode numbering in the legend of Figures 15 - 22: the originally first five calculated were erroneous due to the boundary conditions of the supports. Mode 7 (40.487 Hz) is mainly vertical motion of the whole structure due to the springs under the supports. Natural frequency for a mass-spring oscillator calculated according to the mass of the structure and initial stiffness of the springs is approximately 41.63 Hz.

Table 7. Eigenmodes of the pool without mass of water (Case 1).

| MODE	FREQUENCY [Hz]	MAIN PARTICIPATION FACTOR	GENERALISED MASS
1	12.245	X- & Y-rotation	1188.930
2	16.210	Z-rotation	1496.370
3	22.924	X- & Y-rotation	299.953
4	31.822	X- & Y-rotation	290.893
5	37.277	Y-rotation	781.235
6	38.437	X-rotation	299.776
7	40.487	Z-translation	1776.670
8	43.811	X-rotation	688.479
9	58.653	Y-rotation	136.587
10	62.768	X- & Y-rotation	147.209
11	79.880	Y-rotation	245.094
12	85.745	Y-rotation	213.061
13	94.095	Y-rotation	301.484
14	95.216	Y-rotation	310.725
15	96.617	Z-rotation	136.275
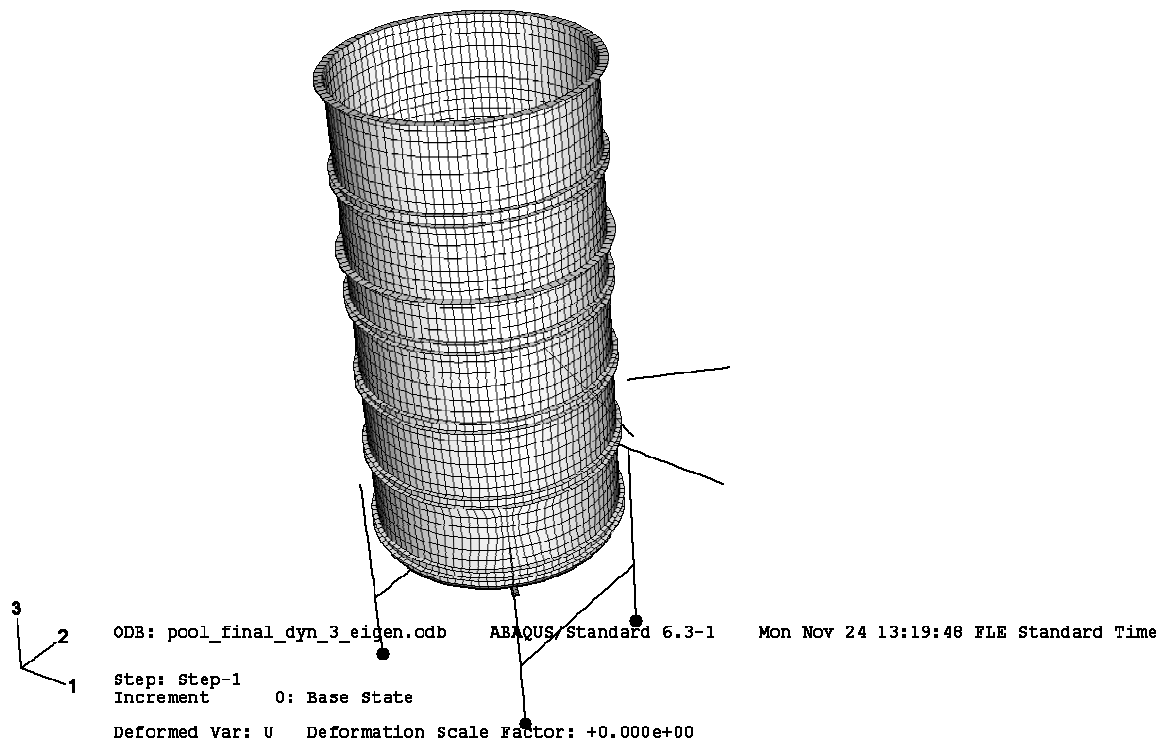
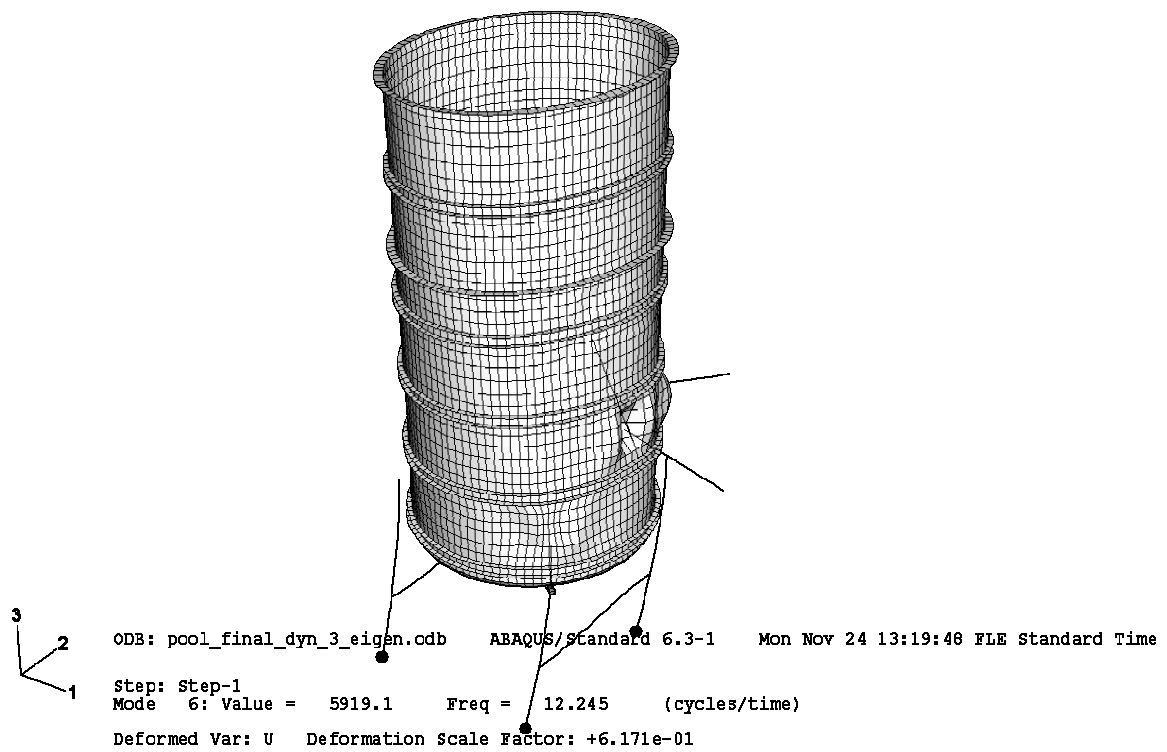*Figure 15. Undeformed shape of the pool.*

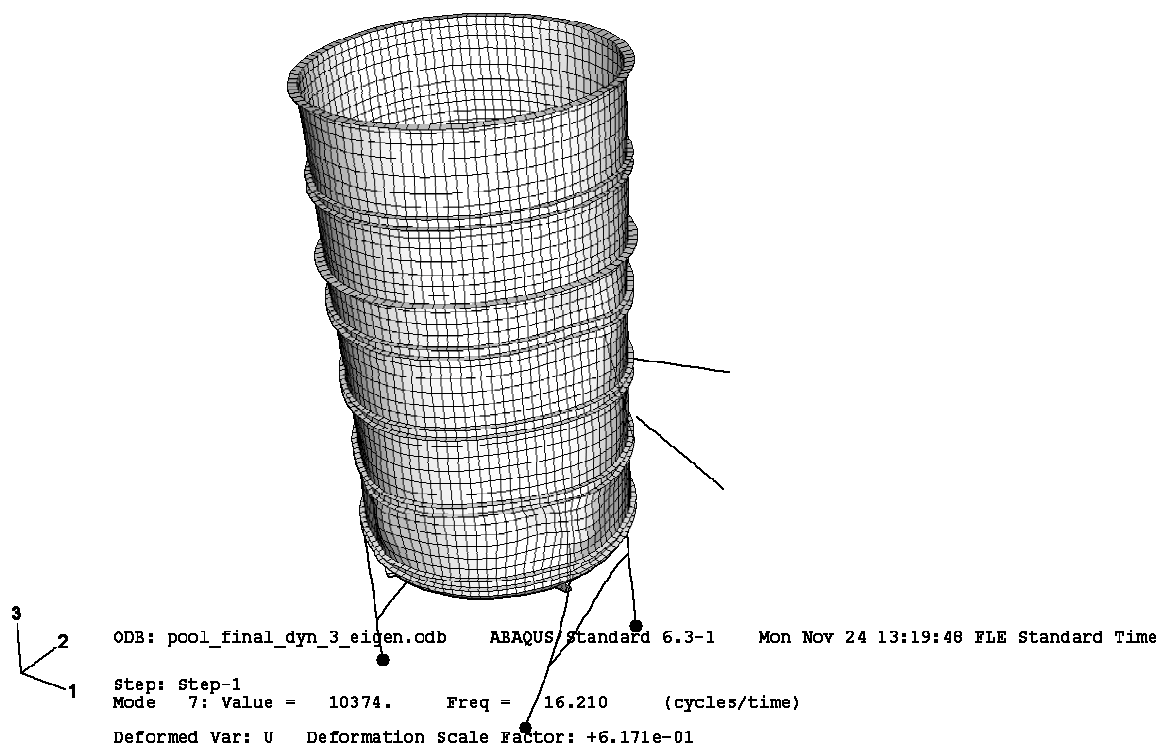*Figure 16. Eigenmode 1 of the pool (Case 1).*

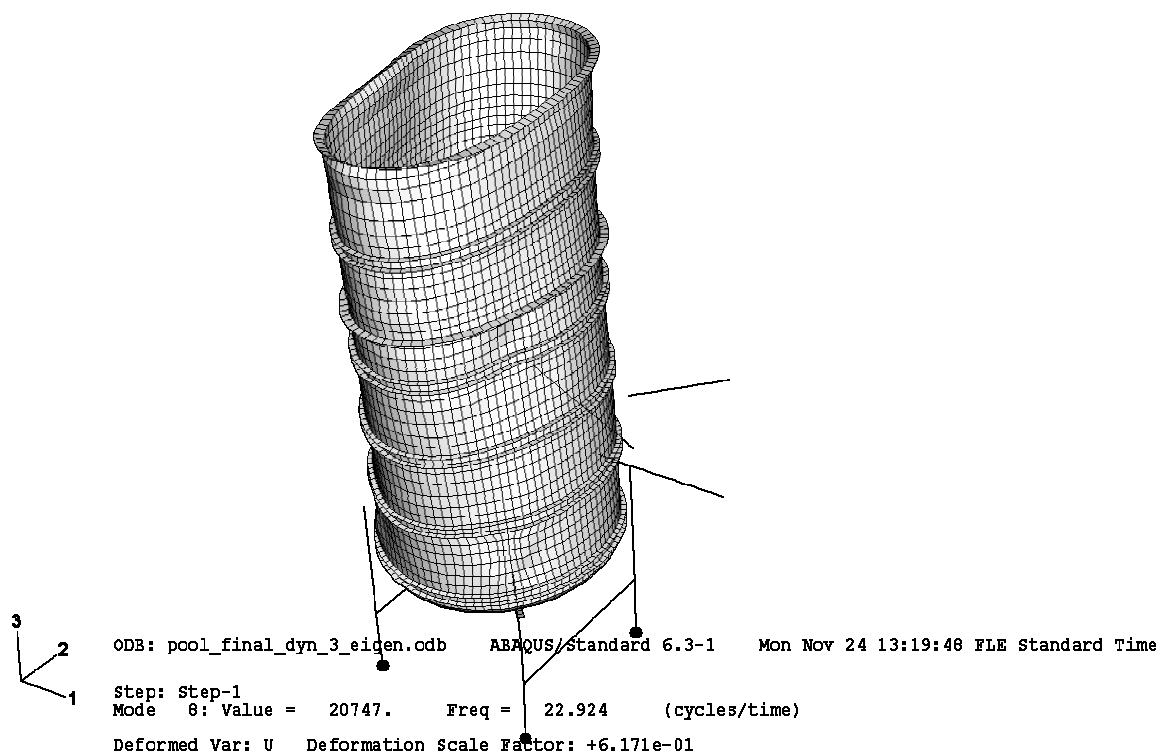*Figure 17. Eigenmode 2 of the pool (Case 1).*

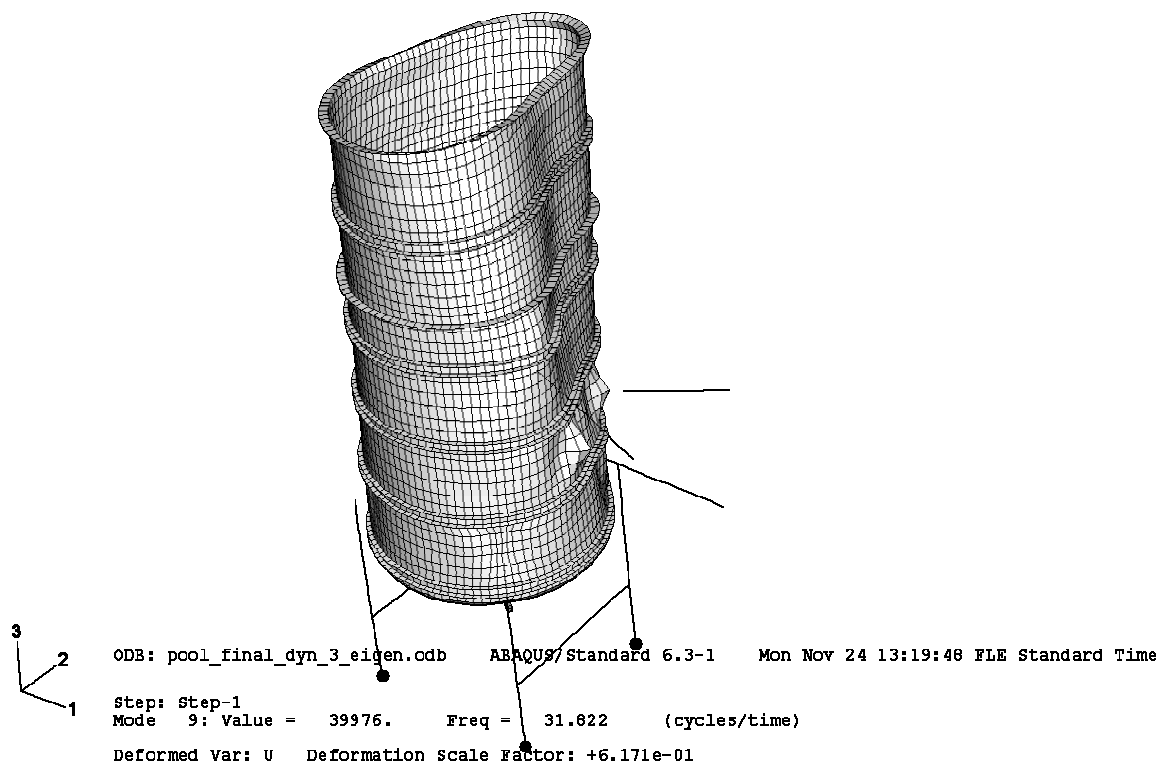*Figure 18. Eigenmode 3 of the pool (Case 1).*

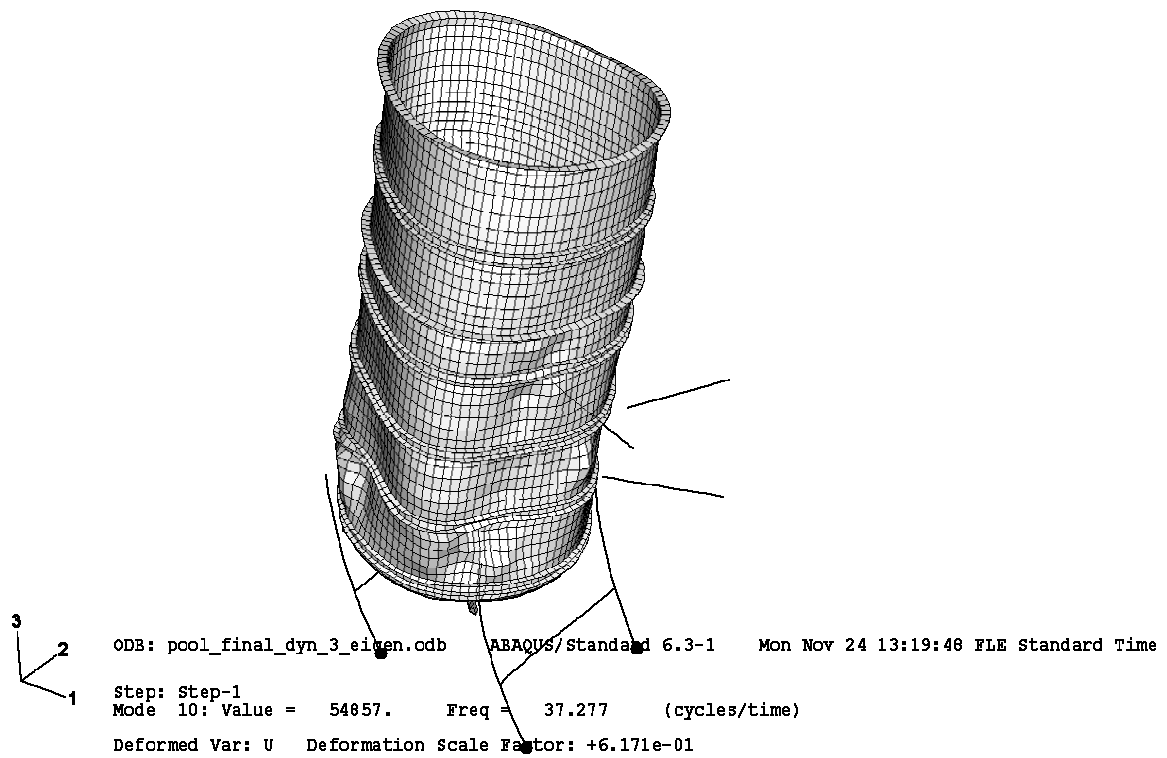*Figure 19. Eigenmode 4 of the pool (Case 1).*

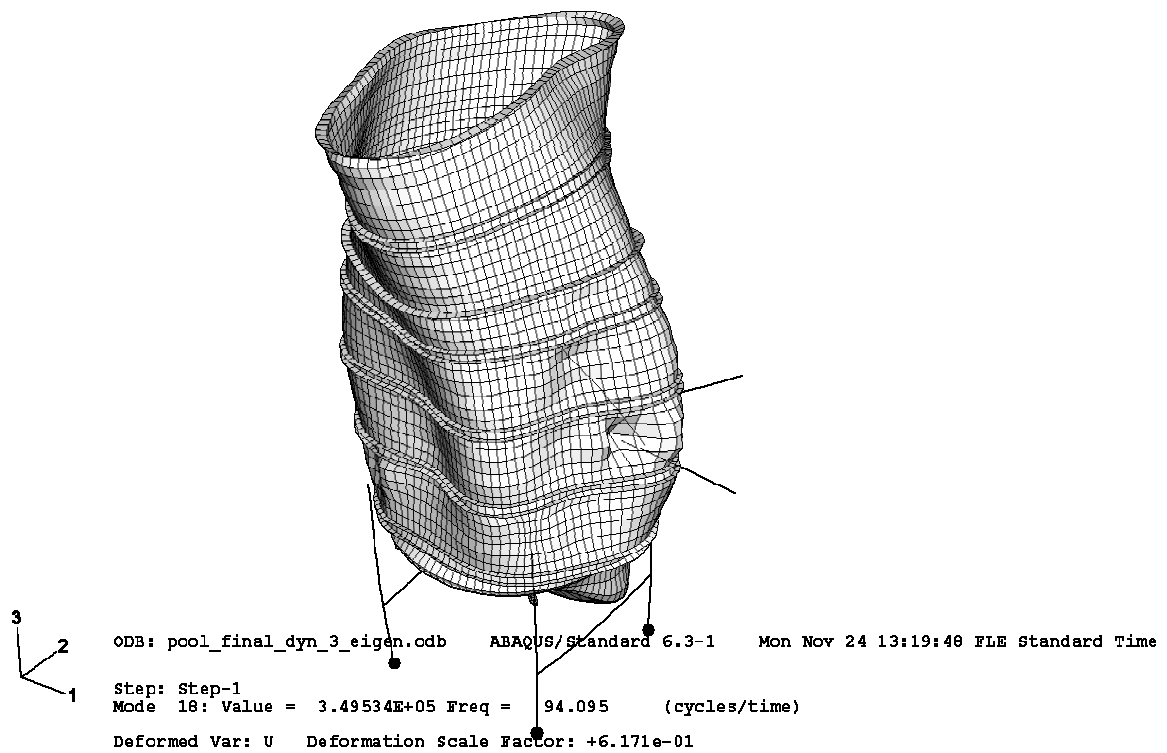*Figure 20. Eigenmode 5 of the pool (Case 1).*

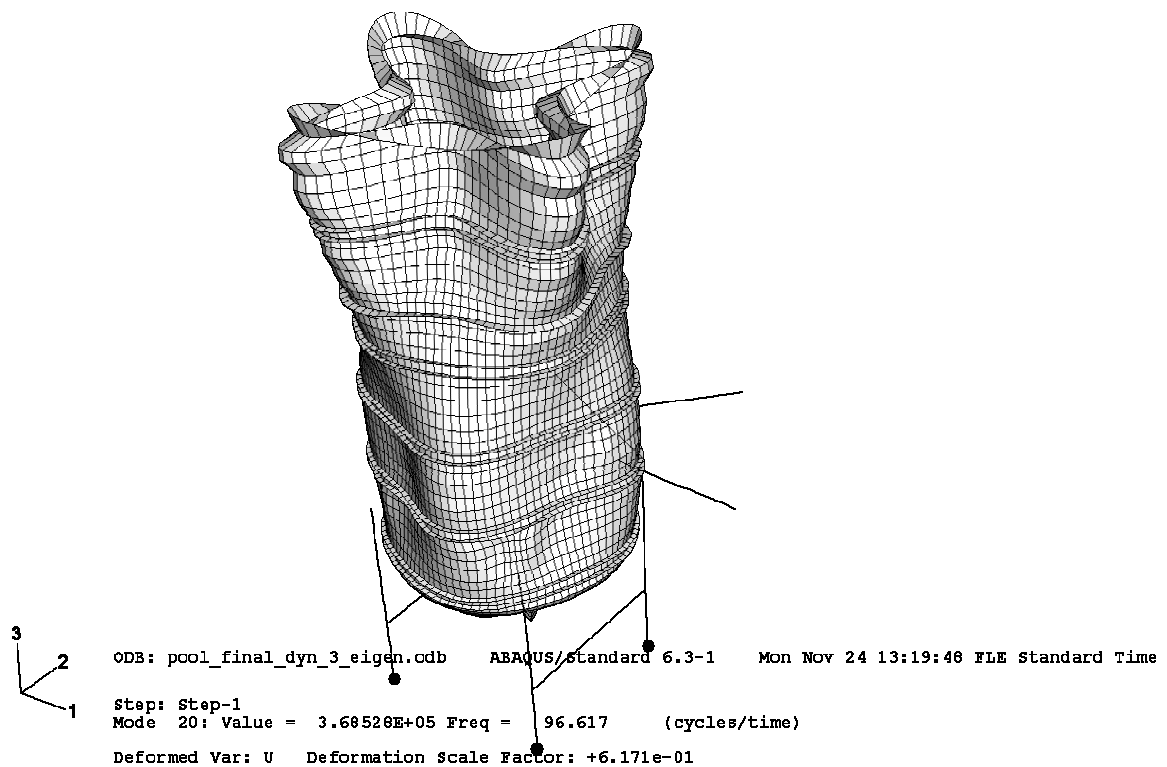*Figure 21. Eigenmode 13 of the pool (Case 1).*

Figure 22. Eigenmode 15 of the pool (Case 1).

In Case 2 the total mass of the model is 14352 kg. Table 8 shows the first 15 eigenfrequencies, the lowest frequency is approximately 5 Hz. Mode 5 (16.373 Hz) is mainly vertical motion of the whole structure due to the springs under the supports. Natural frequency for a mass-spring oscillator calculated according to the mass of the structure and initial stiffness of the springs is approximately 17.22 Hz.

Table 8. Eigenmodes of the pool with mass of water (Case 2).

MODE	FREQUENCY [Hz]	MAIN PARTICIPATION FACTOR	GENERALISED MASS
1	5.064	X- & Y-rotation	7914.350
2	6.284	Z-rotation	10411.500
3	9.997	X- & Y-rotation	3468.710
4	15.052	-	1529.380
5	16.373	Z-translation	11516.300
6	18.517	Y-rotation	2262.010
7	19.457	Y-rotation	1576.230
8	21.841	X-rotation	1760.040
9	24.243	Y-rotation	2389.920
10	25.090	X- & Y-rotation	2557.800
11	29.128	Y-rotation	1550.630
12	30.213	-	1774.840
13	32.994	Y-rotation	1434.610
14	35.668	X- & Y-rotation	1892.610
15	38.306	Y-rotation	1207.200

5.4 Mesh Convergence at Pool Bottom

Sensitivity of the results to mesh refinement at pool bottom is presented with a locally refined mesh shown in Figure 23. It is assumed that the normal mesh is adequate to describe the overall dynamic behaviour of the pool, thus mesh sensitivity is examined only at pool bottom and especially at the rounding, i.e., the joint of pool cylinder wall and pool bottom wall. Only static analyses with hydrostatic pressure corresponding to the water level in CFD calculations were done with the fine mesh. The pool is supported only with the four vertical supports in case of both meshes.

Figures 25 and 26 show von Mises stress distribution in the inner wall of the pool in both cases. Von Mises stress is an equivalent stress, which describes how close to failure a material point in a multi-axial stress state is. In the analyses it is assumed that plastic deformation takes place, when von Mises stress exceeds the yield strength of the material. Maximum stress is located at the bottom rounding. With the normal mesh it is approximately 69 MPa and with the fine mesh approximately 91 MPa. Maximum stresses at the location of welded seam (upper end of the rounding) are approximately 45 and 60 MPa in the inner wall for the normal and fine mesh, respectively. Respective values for the outer wall are 38 and 41 MPa. The large differences are explained by the large element size at the rounding in the normal mesh.

Different stress and displacement values for both cases at corresponding locations are shown in Tables 9 and 10. The locations in Table 9 are shown in Figure 24, locations 1 and 3 are close to the strain gages in the experiments presented in Chapter 7. Stresses differ the most at the rounding centre as expected, von Mises stresses at the rounding are about 68 and 82 MPa for the normal and fine mesh, respectively. The displacements in Table 10 are approximately 8 and 14 % larger for the fine mesh.
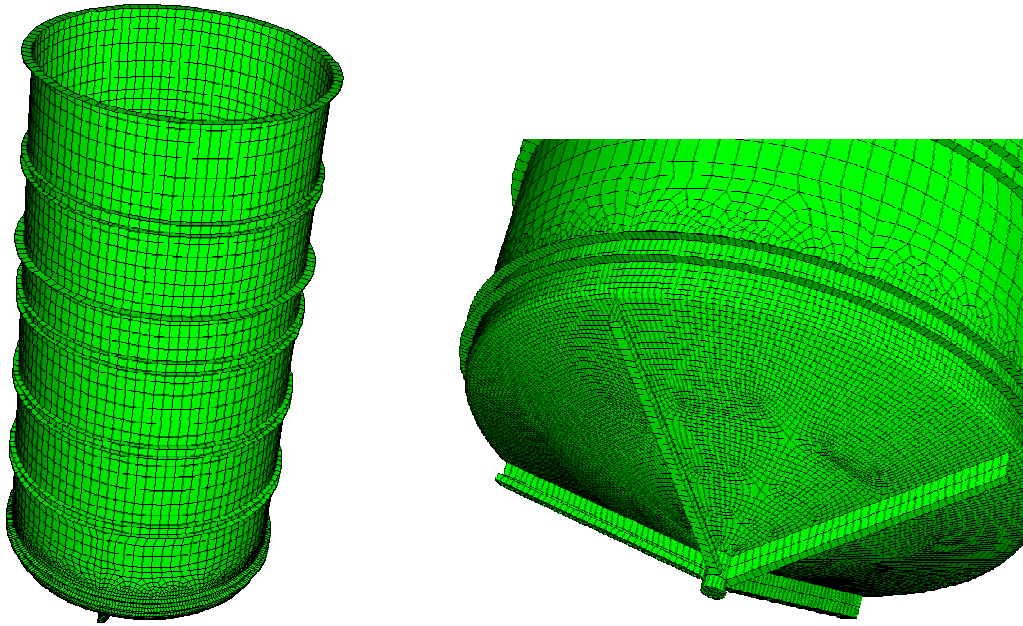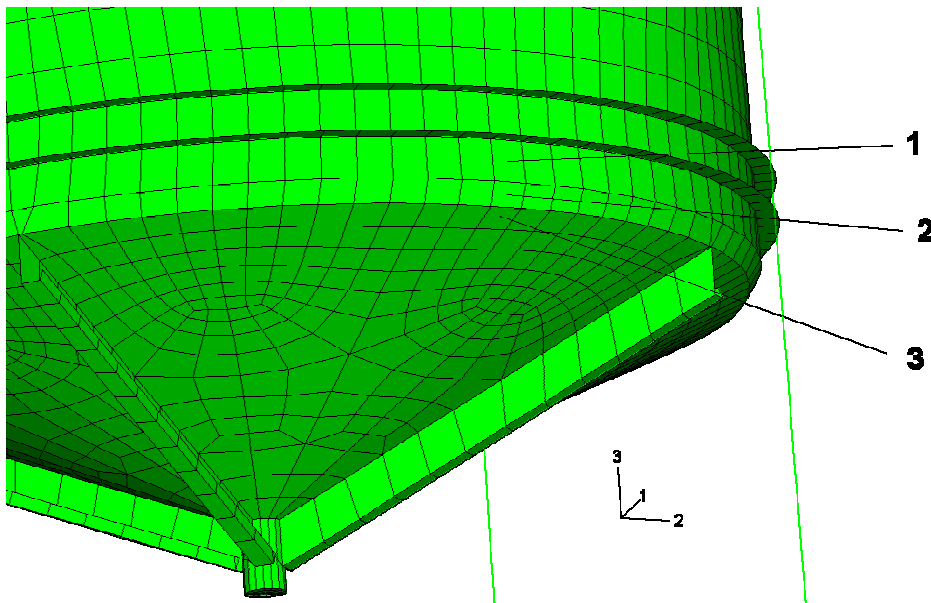

Figure 23. Locally refined pool mesh.
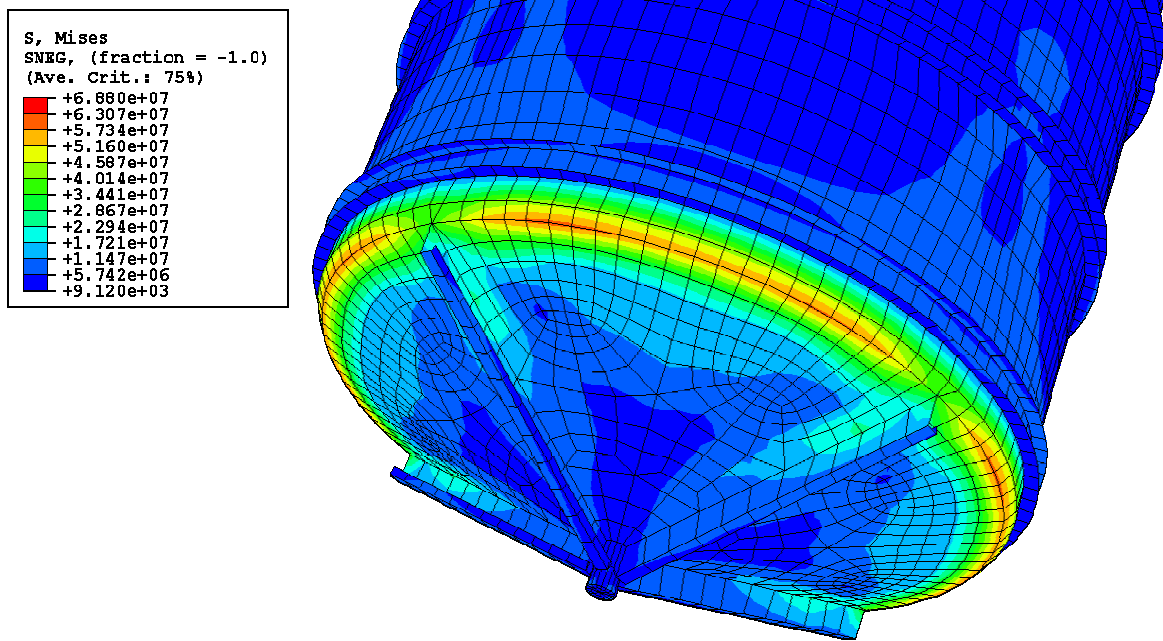

Figure 24. Locations of Table 9.

Figure 25. Von Mises stress (Pascal units in legend) distribution in the inner wall of the pool with hydrostatic pressure (normal mesh). Maximum stress is approximately 69 MPa.
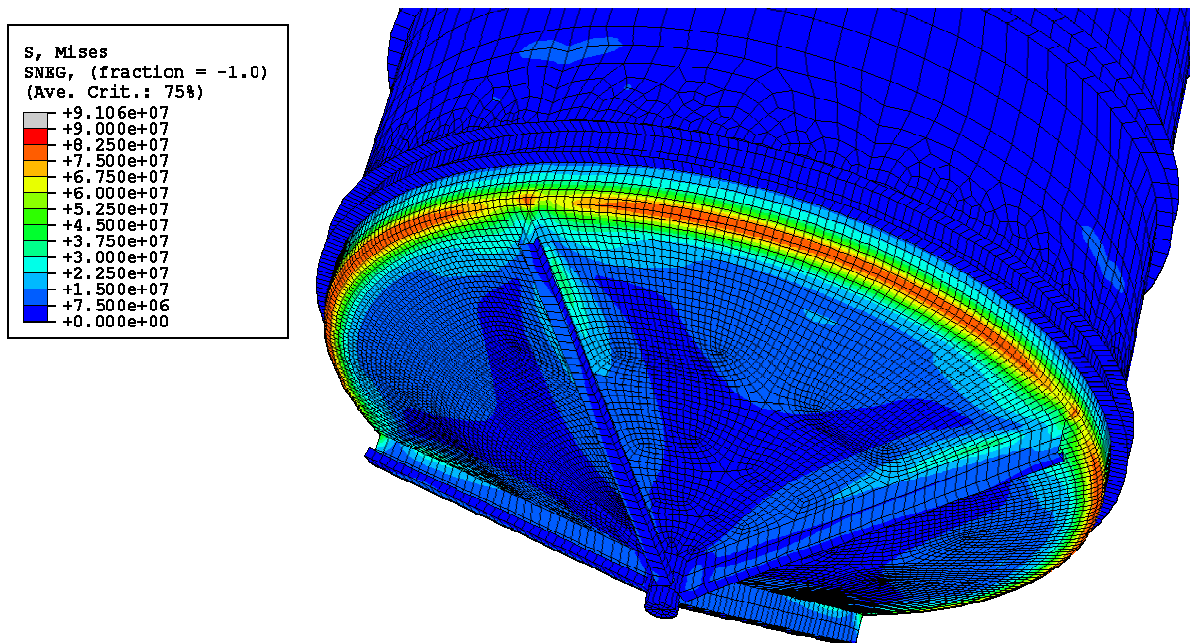

Figure 26. Von Mises stress (Pascal units in legend) distribution in the inner wall of the pool with hydrostatic pressure (fine mesh). Maximum stress is approximately 91 MPa. Notice the different scaling of the stress contours compared to Fig. 25.

Table 9. Different stress values with hydrostatic pressure for both meshes in the inner wall of the pool at the bottom rounding and near it. Positive values are tension and negative compression (1 = above rounding, 2 = at rounding centre, 3 = below rounding). [MPa]

STRESS	LOCATION	NORMAL MESH	FINE MESH
Von Mises	1	19.2	18.5
	2	67.7	82.4
	3	44.6	41.3
Hoop	1	-7.1	-14.9
	2	-19.0	-24.2
	3	30.7	20.6
Axial	1	-21.7	-20.7
	2	55.7	67.6
	3	-20.3	-26.0

Table 10. Vertical displacement of bottom centre and maximum vertical displacement with hydrostatic pressure for both meshes. [mm]

LOCATION	NORMAL MESH	FINE MESH
Bottom centre	-0.57	-0.65
Max.	-0.87	-0.94

5.5 Dynamic Results

Nonlinear dynamic analyses were carried out using ABAQUS/Standard code version 6.3.1 (ABAQUS, 2002). Results of the three cases in Table 5 are introduced and compared with each other in this chapter. Automatic time incrementation with a half-increment residual tolerance of 1 kN was used, while typical nodal force varies between 80 - 800 N during the analyses. Minimum time increment during the analyses is a little over 10 µs (at pressure peak), average time increment is 135 - 205 µs. Duration of the analyses is 32 ms.

Figures 27 - 36 show contour plots of inner and outer wall von Mises stress distribution at different instants of time in Case 1 (without mass of water). Notice the differences in the scaling of the contours and deformations in the legends in Figures 27 - 36. The maximum stress value during the analyses is approximately 211 MPa at 32 ms and it is located in the inner wall at the rounding, i.e., the joint of pool cylinder wall and pool bottom wall. Figure 32 shows the stress distribution in Case 1 in the outer wall at time instant 22.9 ms, the maximum stress value of approximately 203 MPa occurs at the rounding. The outer wall has generally lower von Mises stresses at the rounding. The yield stress of the pool wall material is 200 MPa, which is exceeded during the analyses. The stresses and plastic deformations presented at the rounding should be scaled upwards according to the results presented in Chapter 5.4.

In Case 1 the maximum von Mises stresses at the location of the welded seam (upper end of the rounding) are approximately 155 MPa (inner wall) and 180 MPa (outer wall) during the analyses. Also these stresses are underestimations according to the results presented in Chapter 5.4. Maximum stress around the welded plates of the vertical supports occurs at about 27.4 ms with a value of approximately 120 MPa, but generally the stresses around the plates

stay much lower (see Fig. 35 and 36). With mere hydrostatic pressure, maximum around the plates is only approximately 7.5 MPa.

The stresses and the occurring plastic deformations in the pool would be greatly larger with a static pressure load having the same magnitude as the calculated pressure peak, but the impact-like load reduces the response of the pool. The duration of the pressure peak is very short (only ~0.4 ms, see Fig. 14) compared to the periodic time of the motion of the pool bottom. The response of the bottom in Case 1 and 2 can be seen later in Figure 40.

Contour plots of the equivalent plastic strain at the end of the analyses in Case 1 are shown in Figures 37 and 38. Plastic deformation occurs only at the rounding and near it, maximum equivalent plastic strain is approximately 0.226 % in the inner wall and 0.114 % in the outer wall.
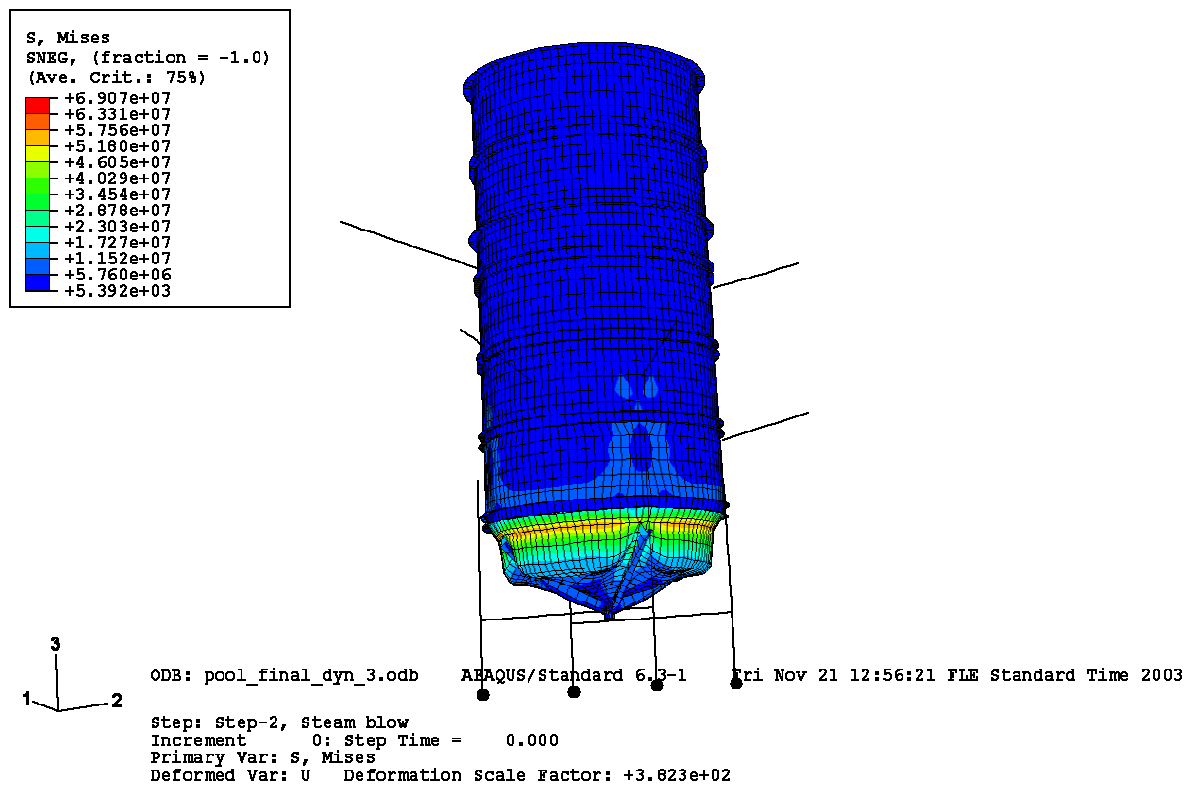
Figure 27. Von Mises stress (Pascal units in legend) distribution in the inner wall of the pool in Case 1 at the beginning of the analyses (only hydrostatic pressure). Maximum stress is approximately 69 MPa. Notice the deformation scale factor in the legend.
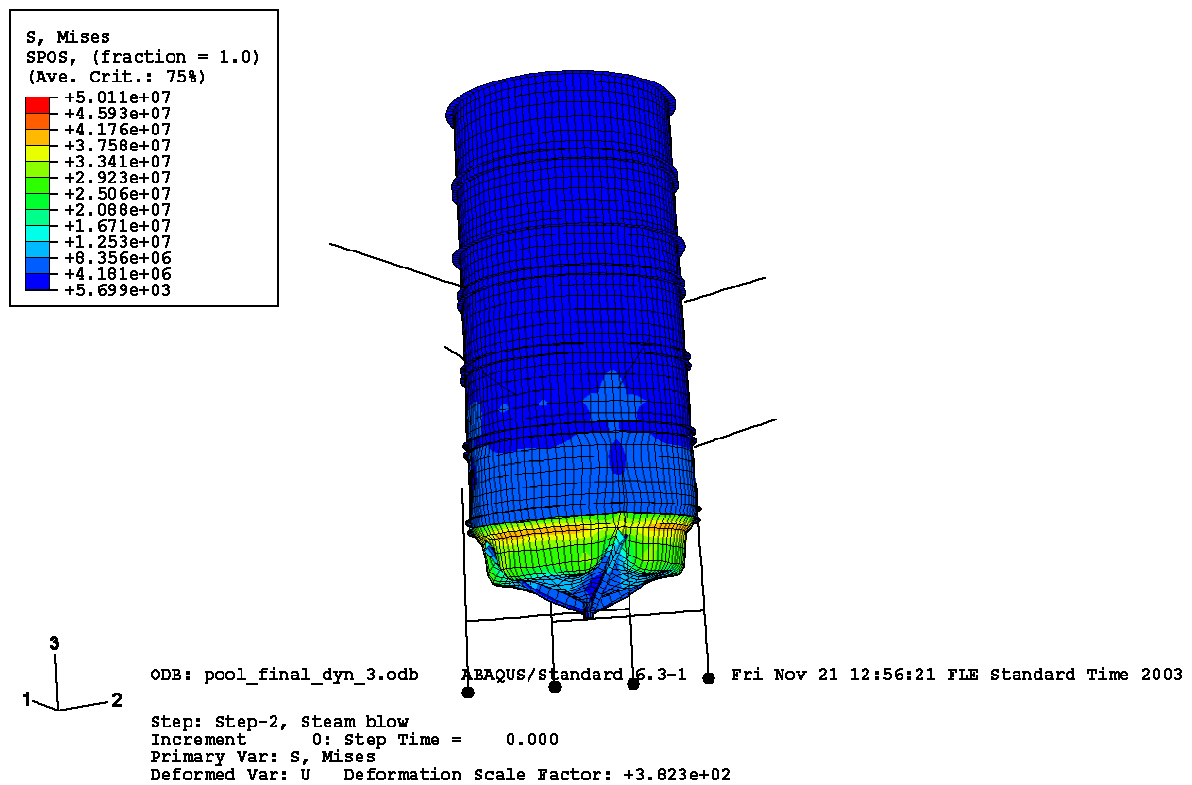

Figure 28. Von Mises stress (Pascal units in legend) distribution in the outer wall of the pool in Case 1 at the beginning of the analyses (only hydrostatic pressure). Maximum stress is approximately 50 MPa. Notice the deformation scale factor in the legend.
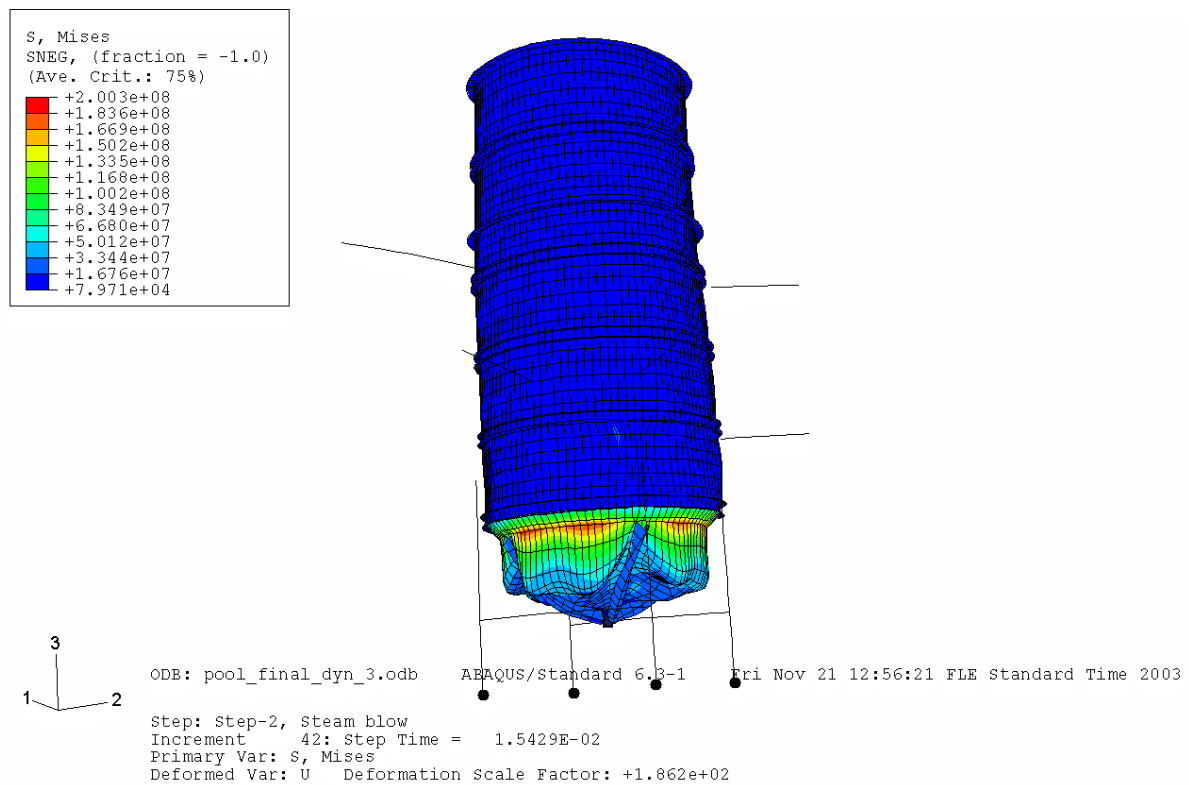
Figure 29. Von Mises stress (Pascal units in legend) distribution in the inner wall of the pool in Case 1. Time instant is approximately 15.4 ms, maximum stress is approximately 200 MPa. Notice the deformation scale factor in the legend.

Figure 30. Von Mises stress (Pascal units in legend) distribution in the inner wall of the pool in Case 1. Time instant is approximately 19.4 ms, maximum stress is approximately 127 MPa. Notice the deformation scale factor in the legend.

Figure 31. Von Mises stress (Pascal units in legend) distribution in the inner wall of the pool in Case 1. Time instant is approximately 22.9 ms, maximum stress is approximately 206 MPa. Notice the deformation scale factor in the legend.

Figure 32. Von Mises stress (Pascal units in legend) distribution in the outer wall of the pool in Case 1. Time instant is approximately 22.9 ms, maximum stress is approximately 203 MPa. Notice the deformation scale factor in the legend.
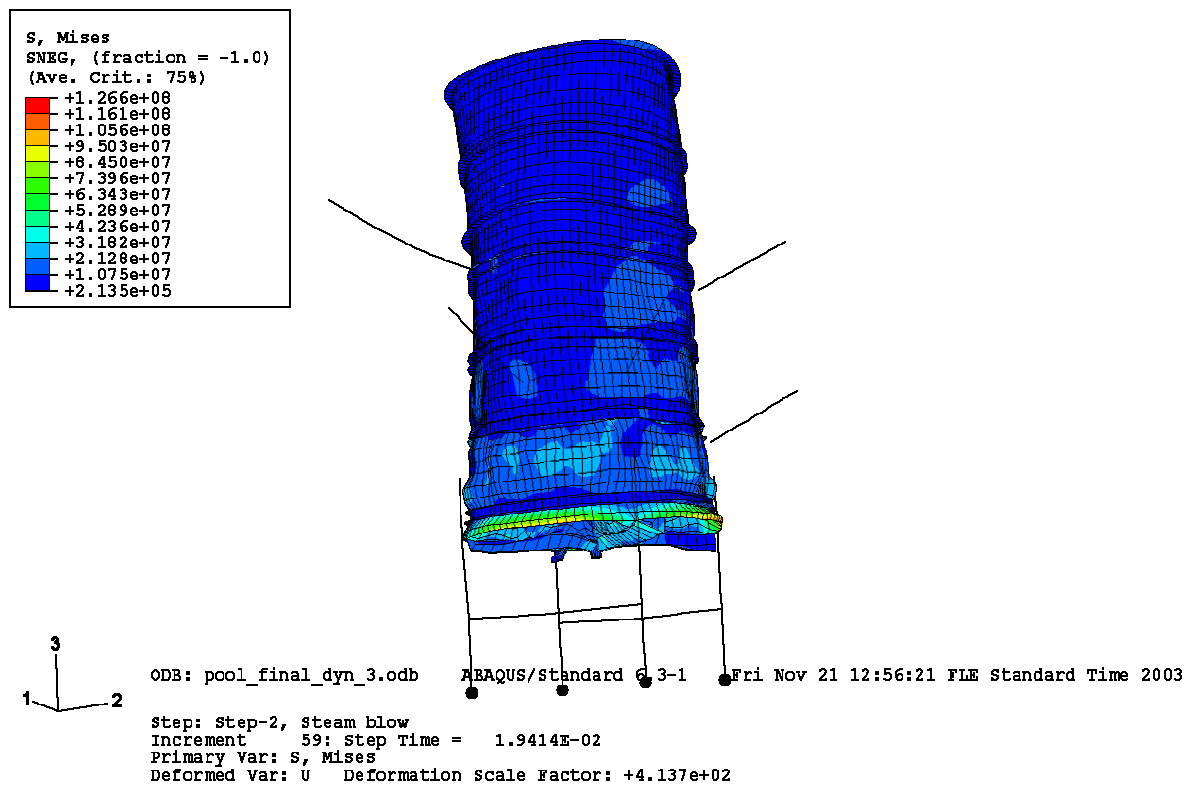
Figure 33. Von Mises stress (Pascal units in legend) distribution in the inner wall of the pool in Case 1. Time instant is approximately 28.8 ms, maximum stress is approximately 161 MPa. Notice the deformation scale factor in the legend.
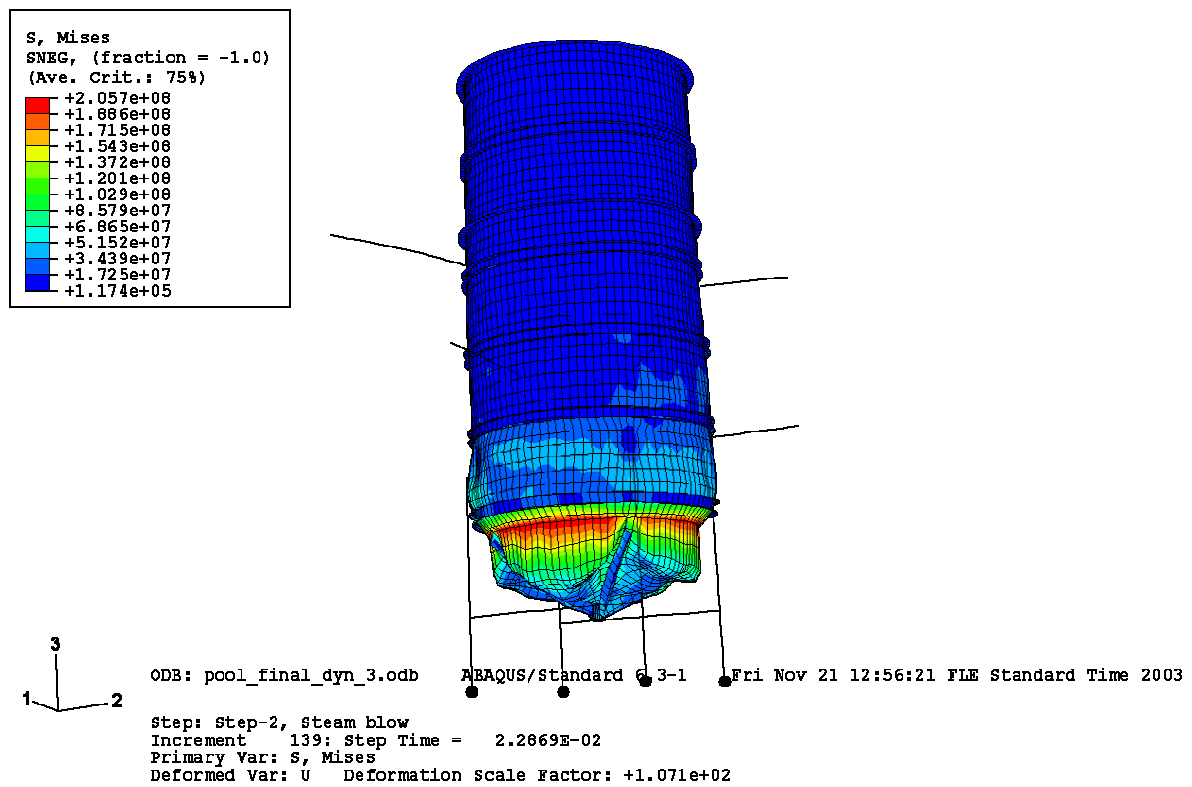

Figure 34. Von Mises stress (Pascal units in legend) distribution in the inner wall of the pool in Case 1. Time instant is approximately 31.9 ms, maximum stress is approximately 211 MPa. Notice the deformation scale factor in the legend.
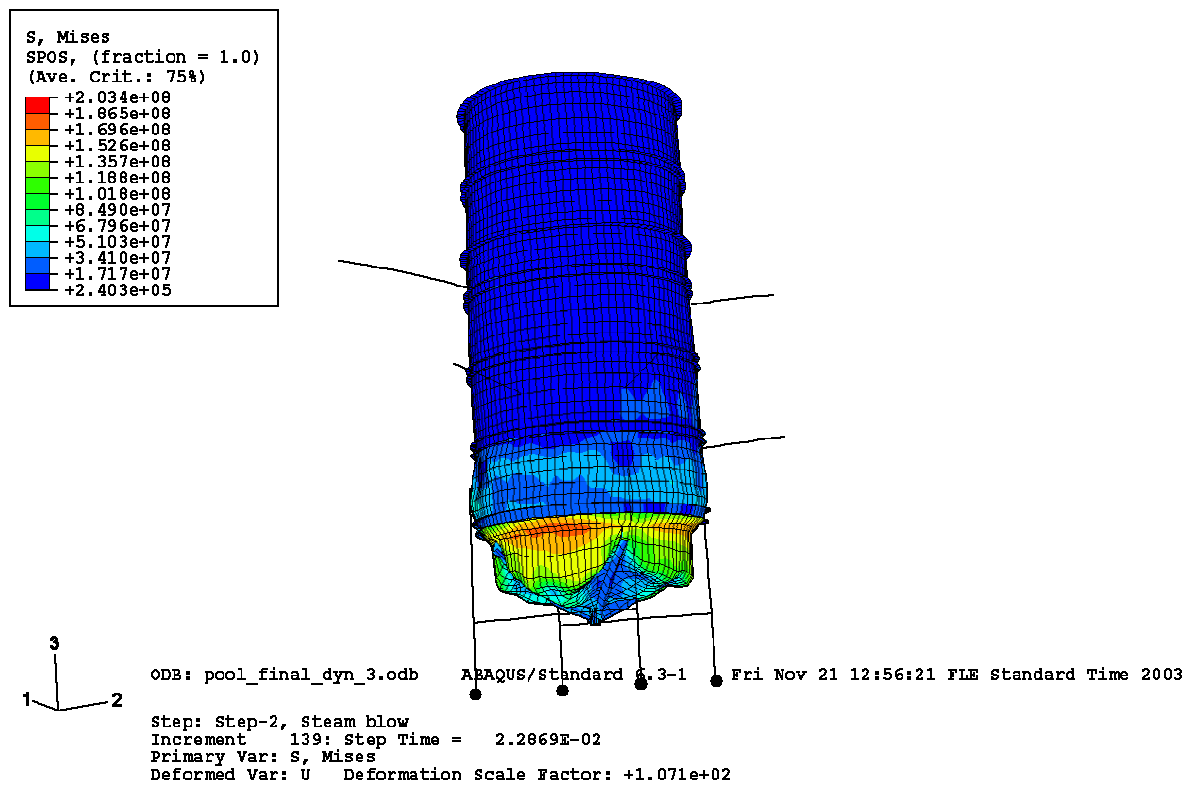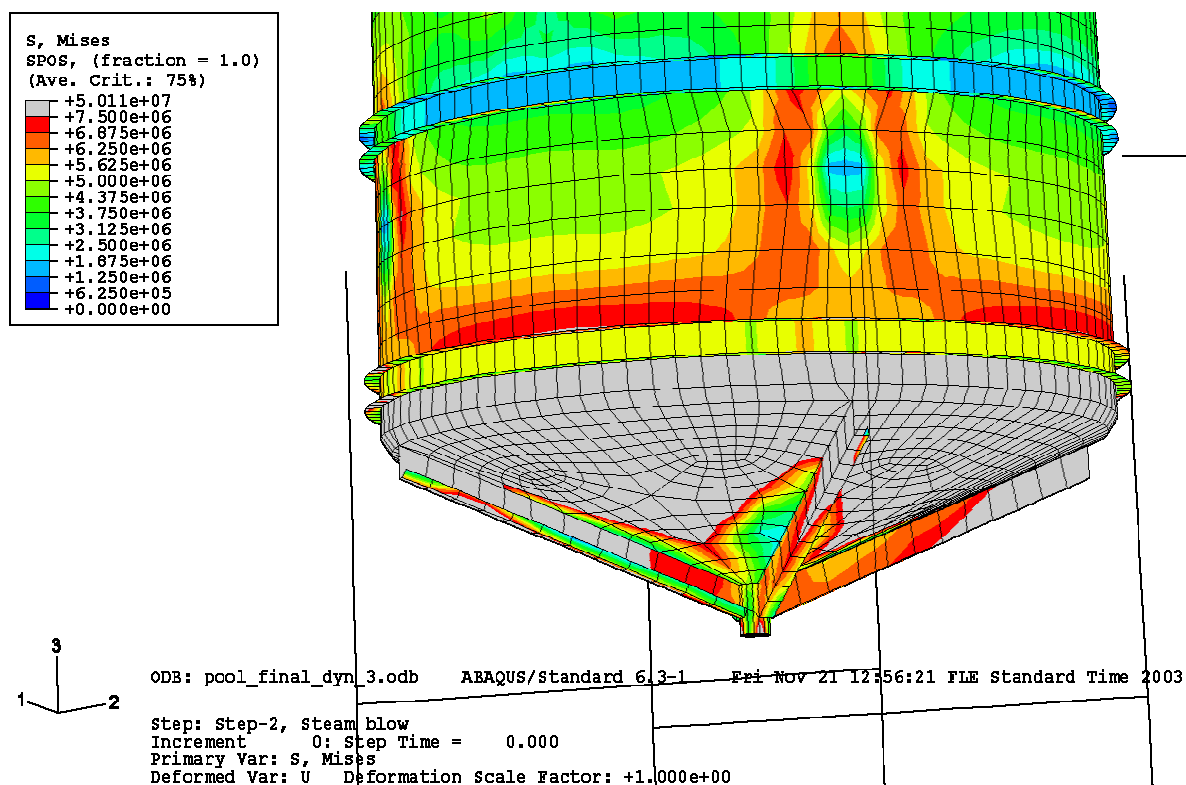
Figure 35. Von Mises stress (Pascal units in legend) distribution in the outer wall of the pool in Case 1 at the beginning of the analyses (only hydrostatic pressure). Maximum stress around the welded plate is approximately 7.5 MPa.
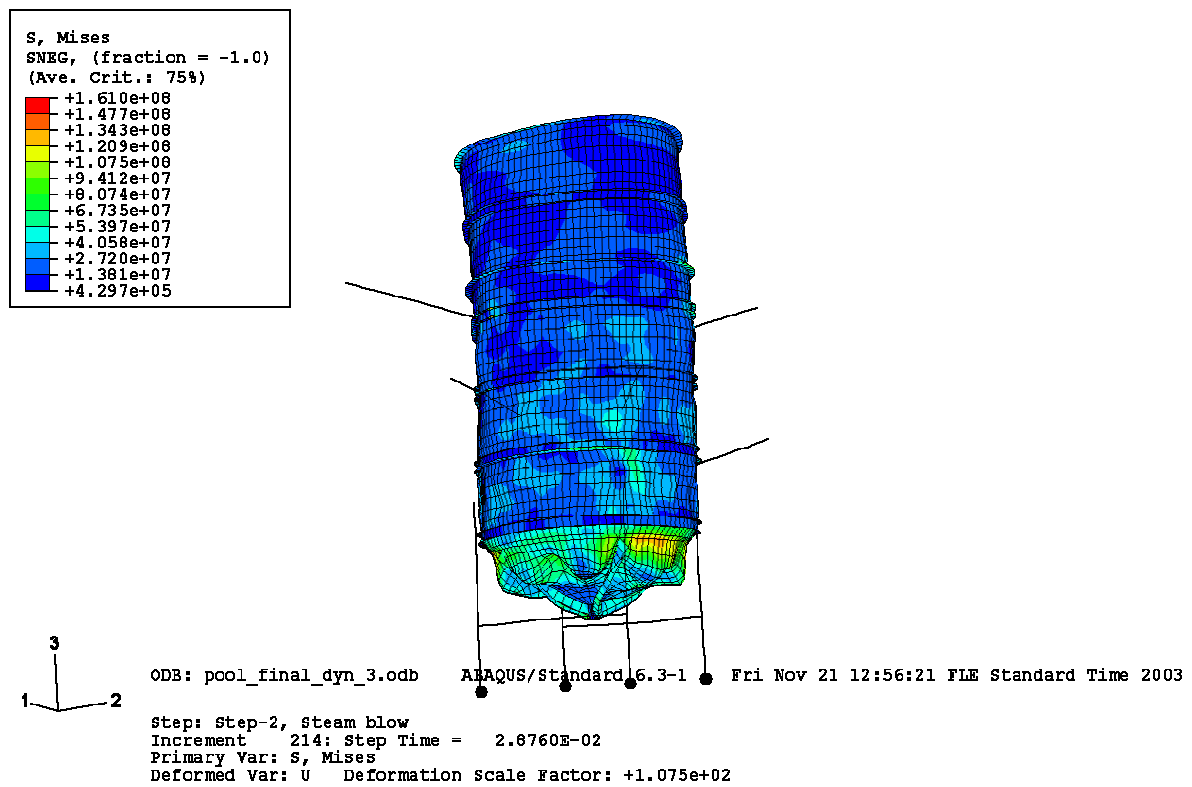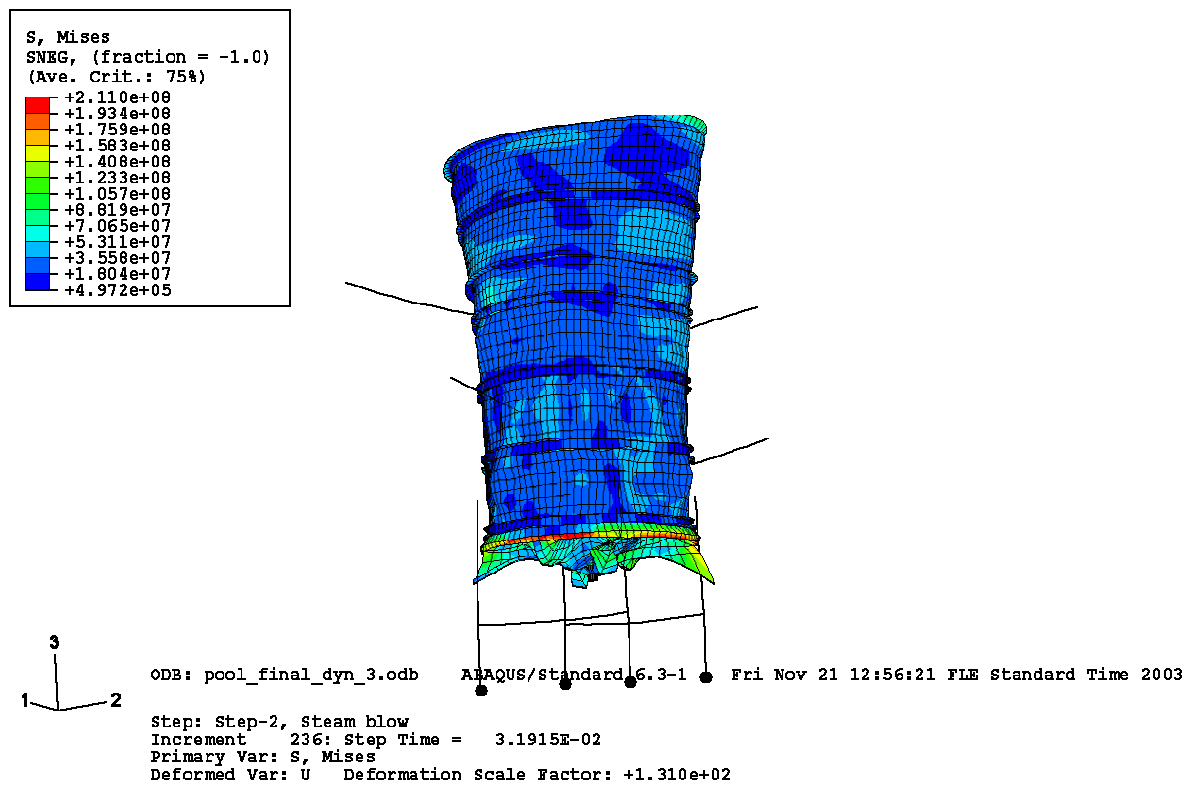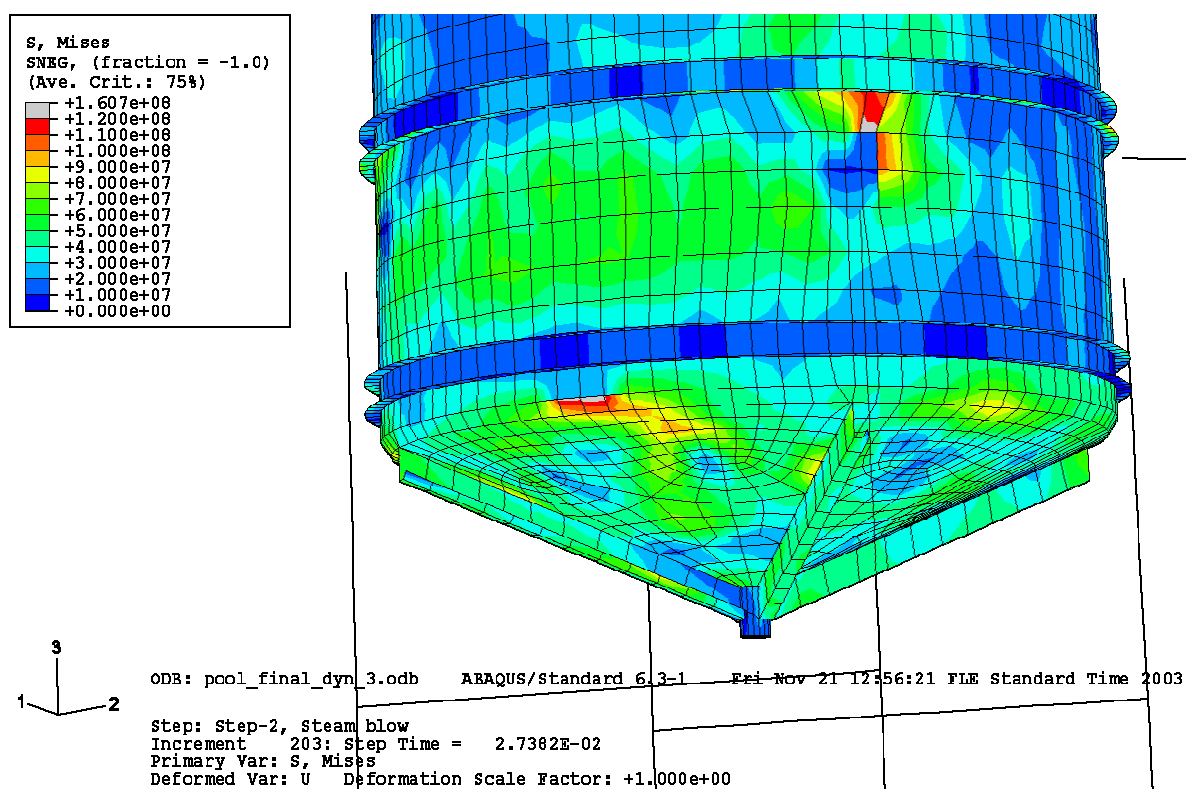

Figure 36. Von Mises stress (Pascal units in legend) distribution in the inner wall of the pool in Case 1. Time instant is approximately 27.4 ms. Maximum stress around the welded plate is approximately 120 MPa.

Figure 37. Equivalent plastic strain distribution in the inner wall of the pool at the end of the analyses in Case 1. Time instant is approximately 31.9 ms. Maximum equivalent plastic strain is approximately 0.226 %.

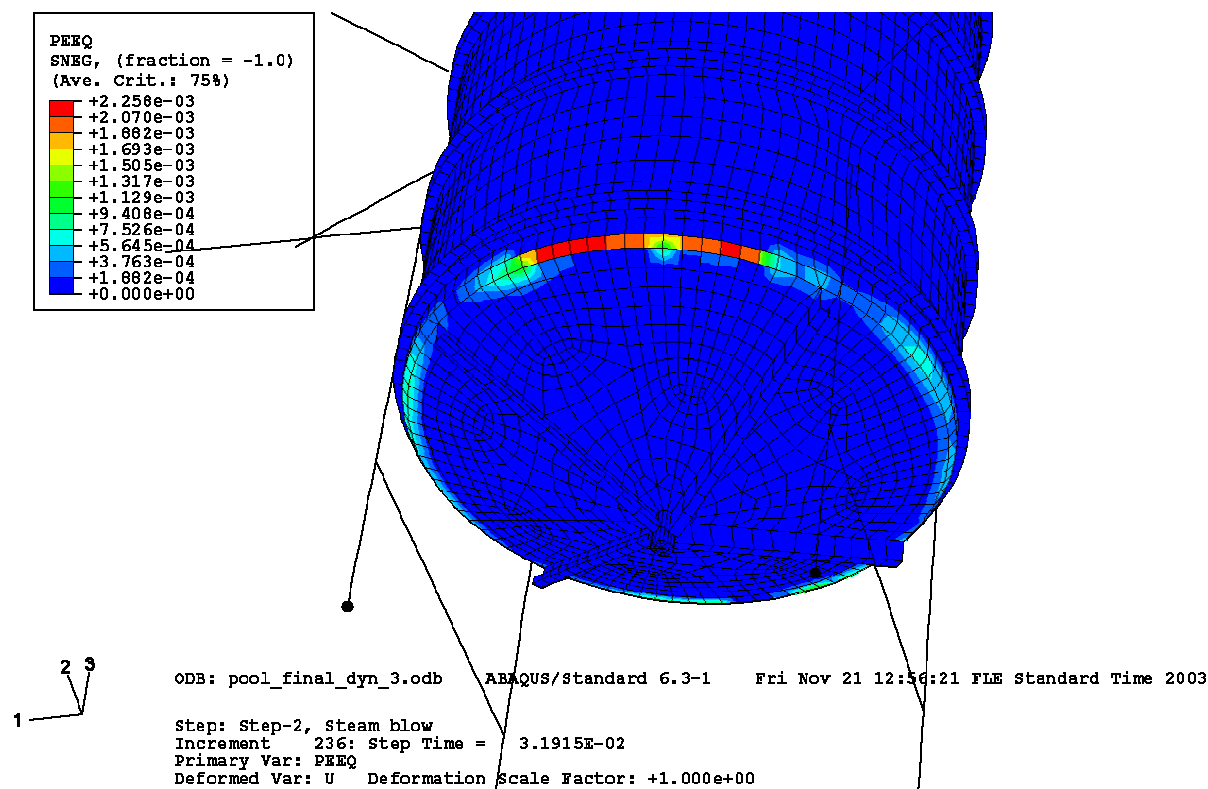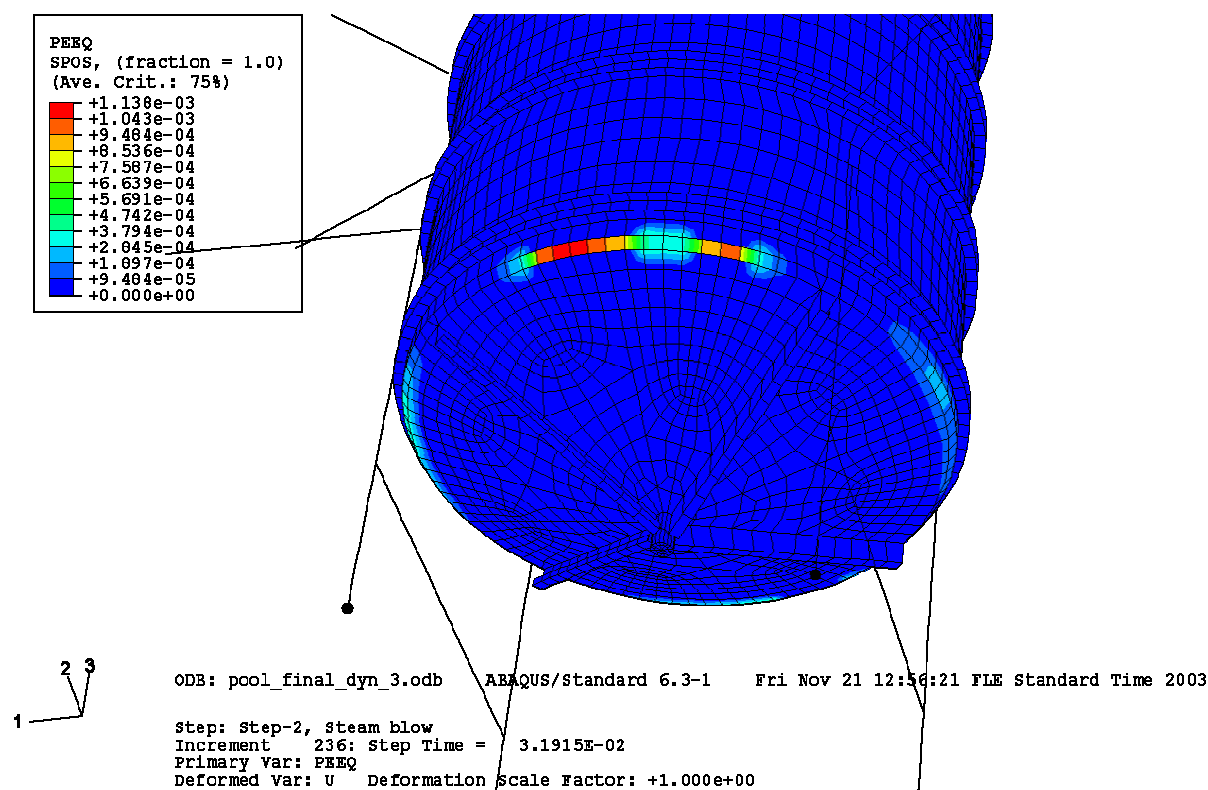*Figure 38. Equivalent plastic strain distribution in the outer wall of the pool at the end of the analyses in Case 1. Time instant is approximately 31.9 ms. Maximum equivalent plastic strain is approximately 0.114 %.*

Figure 39 shows plastic dissipation together with strain energy for whole model in both cases. Plastic deformation initiated at the rounding at 14.8 ms in Case 1 (without mass of water, only less than 0.1 J from 14.8 to 21 ms) and at 26 ms in Case 2 (mass of water included). In Case 1 maximum strain energy is approximately 930 J, while plastic dissipation at the end of the analyses is approximately 100 J. Corresponding values for Case 2 are 670 and 61 J.
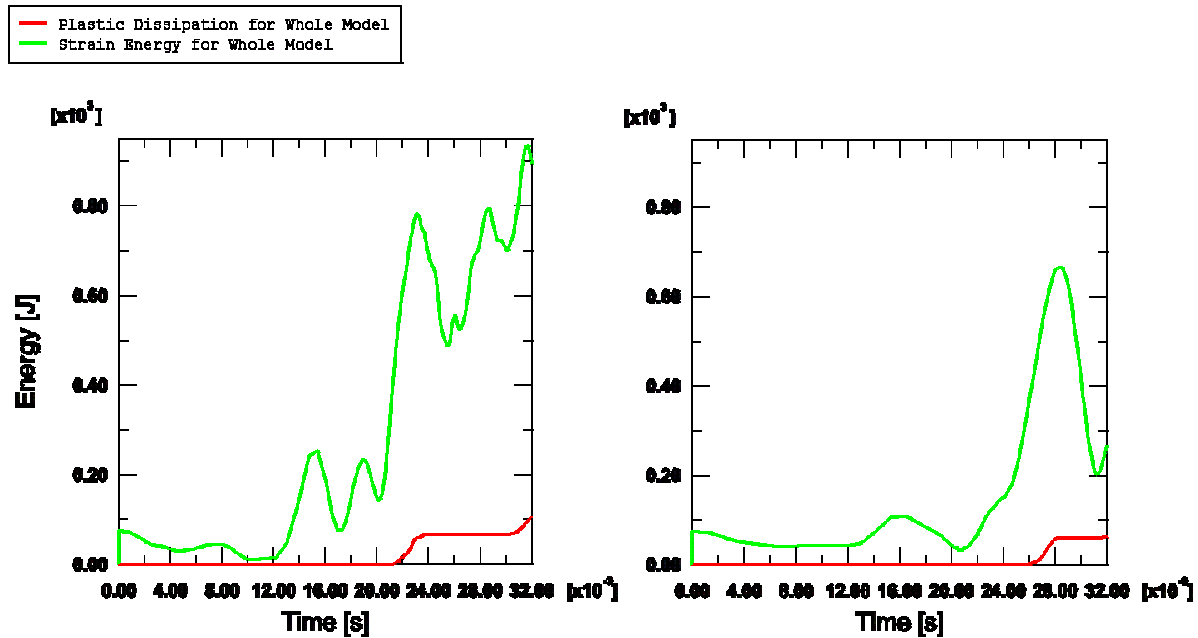

Figure 39. Plastic dissipation and strain energy as a function of time for whole model. Case 1 on the left, Case 2 on the right. In Case 1 maximum strain energy is approximately 930 J, while plastic dissipation at the end of the analyses is approximately 100 J.

Figure 40 shows the vertical displacement of the pool bottom centre, lower ends of the vertical supports and 4 opposite locations (90 degrees intervals) at the top of the pool. The maximum displacements of the pool bottom are approximately 4.1 mm downwards in Case 1 and 3.3 mm in Case 2, but this displacement is in part due to vertical motion of the whole structure. Maximum displacement of the pool bottom centre due to the strain of the wall alone is about 2.5 mm downwards. Maximum vertical displacement of the whole pool is over 2 mm. Vertical motion of the whole structure is due to the springs under the vertical supports. The peaks are higher without the mass of water. The peaks coincide with the pressure peaks, but the response of the pool is delayed in Case 2 compared to Case 1. The largest overpressure peak occurred at about 22.3 ms. Figure 40 clearly shows that the amplitude and frequency of the motion of the pool bottom are higher without the added mass. The frequencies estimated from the displacement curves are approximately 140 Hz for Case 1 and 70 Hz for Case 2.

Figure 41 shows the horizontal displacement components (directions 1 and 2 in Fig. 11) of the 4 opposite locations at the top of the pool. The maximum displacements are approximately 3.8 and 1.3 mm for Case 1 and 2, respectively. The maximums are mainly due to the distortion of the shape of the pool (see Fig. 34). Again, the highest peak is in Case 1.
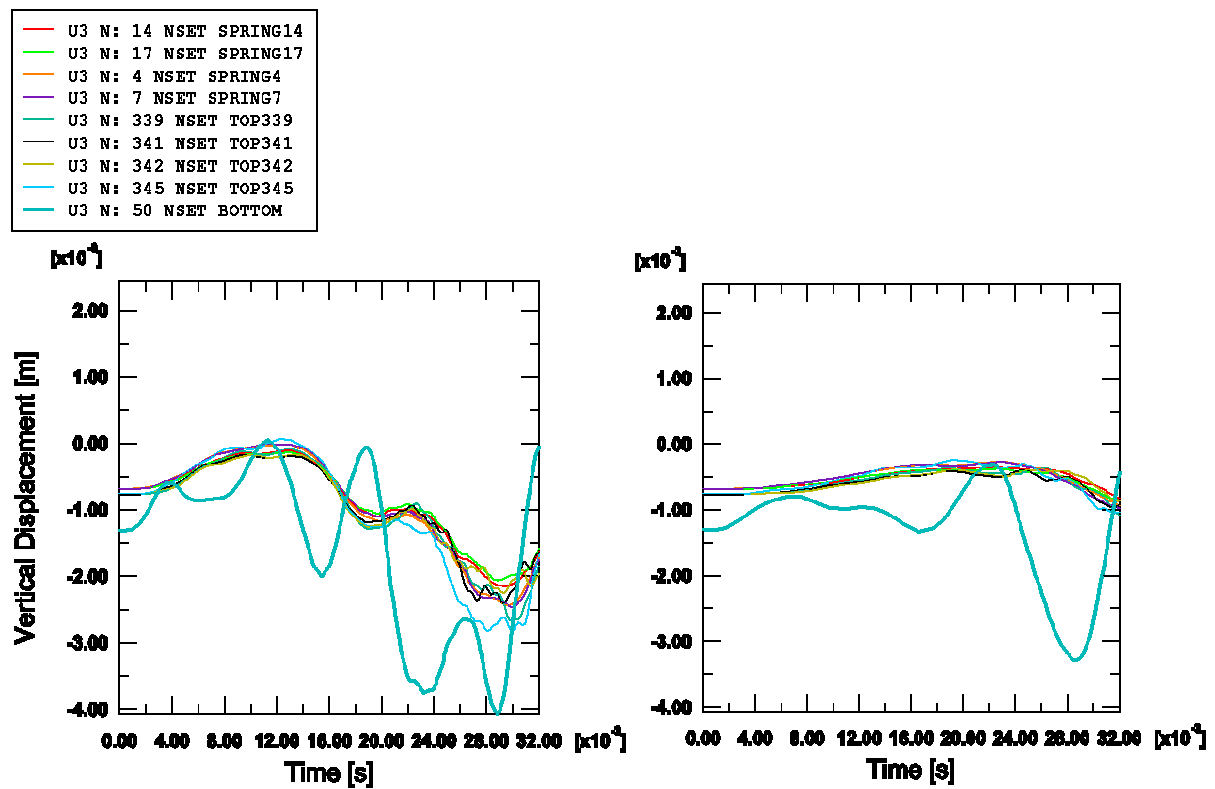
Figure 40. Vertical displacement of the pool bottom centre, lower ends of the vertical supports and 4 opposite locations at the top of the pool as a function of time. Case 1 on the left, Case 2 on the right. Maximum displacement of the pool bottom is approximately 4.1 mm (including the displacement of the whole pool) in Case 1.

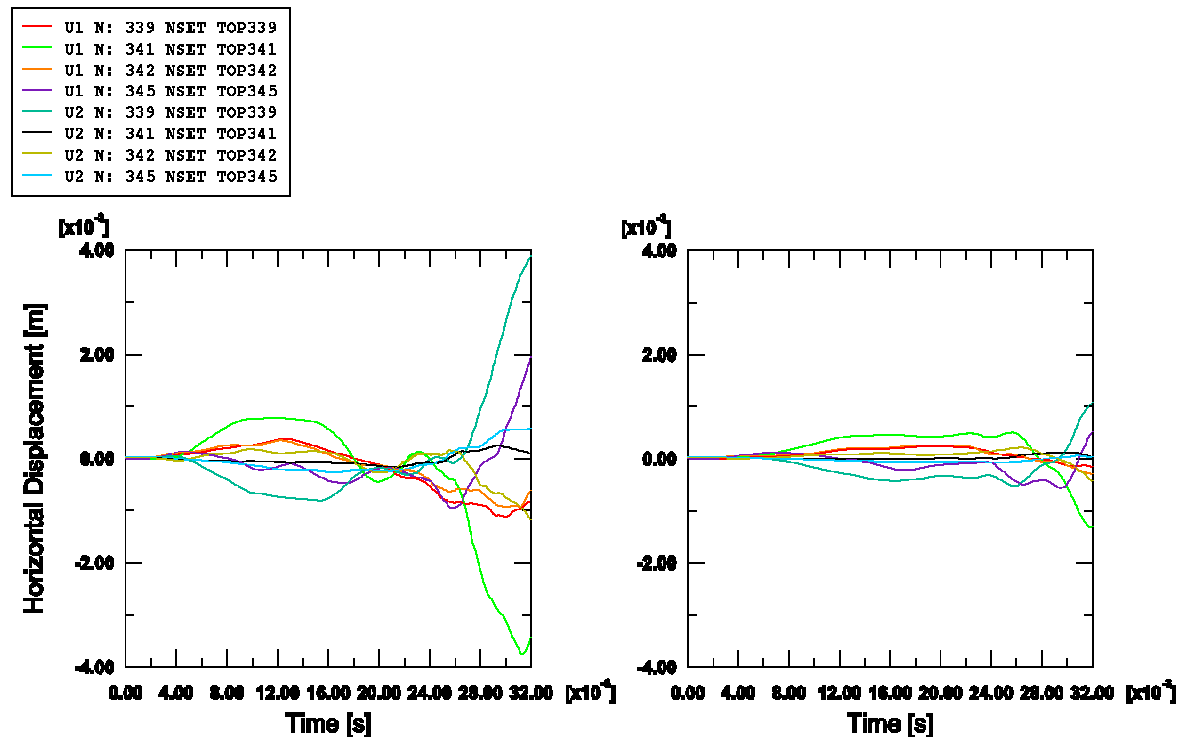*Figure 41. Horizontal displacement components of the 4 opposite locations at the top of the pool as a function of time. Case 1 on the left, Case 2 on the right. Maximum displacement is approximately 3.8 mm (Case 1).*

Figure 42 shows the horizontal displacement components (directions 1 and 2 in Fig. 11) of the vertical support ends from which they are joined to the pool. Magnitudes stay below 0.7 mm in Case 1 and below 0.4 mm in Case 2. Displacements in Case 1 have higher frequency and amplitude.

Figure 43 shows the vertical reaction forces in the springs under the vertical supports. The higher natural frequency of the structure without the mass of water is again clearly visible. Periodic times of the vertical motion of the whole pool calculated by the eigenmodes (see Chapter 5.3) are approximately 25 and 61 ms for Case 1 and 2, respectively. A maximum reaction force of 95 kN occurred in Case 1 after the pressure peak, which is significantly greater than the maximum of 40 kN in Case 2. It can be noted that the reaction forces of all the four springs have very equal magnitudes.

The phenomenon in the analyses are rapid, thus some consideration should be given to the speed of sound in the structure. The dilatational wave speed in steel is approximately 5000 m/s, which means that the time required for such a wave to reach the lower ends of the supports from the pool bottom (distance ~2.5 m) is approximately 0.5 ms. This is a relatively short period compared to the time scale of the fluctuations in Figure 43.

The stresses in the vertical supports are examined by Calonius et al. (2003). Compressive maximum stress in the support due to the force of 95 kN would be approximately 69 MPa.

Figure 44 shows the horizontal reaction force components (directions 1 and 2 in Fig. 11) in the five side stays. Magnitudes stay below 45 kN in Case 1 and below 18 kN in Case 2.
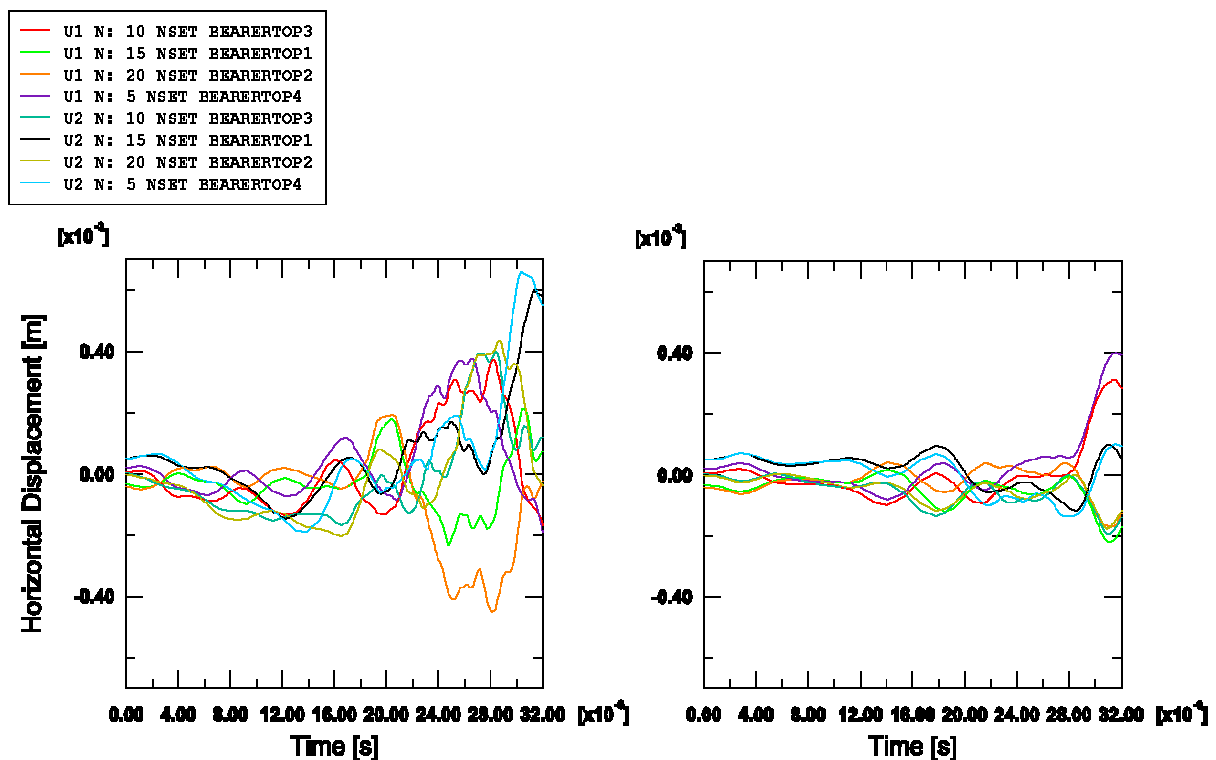
Figure 42. Horizontal displacement components of the upper ends of the vertical supports as a function of time. Case 1 on the left, Case 2 on the right. Maximum displacement is approximately 0.66 mm (Case 1).

Figure 43. Vertical reaction forces in the springs as a function of time. Case 1 on the left, Case 2 on the right. Maximum reaction force is approximately 95 kN (Case 1).
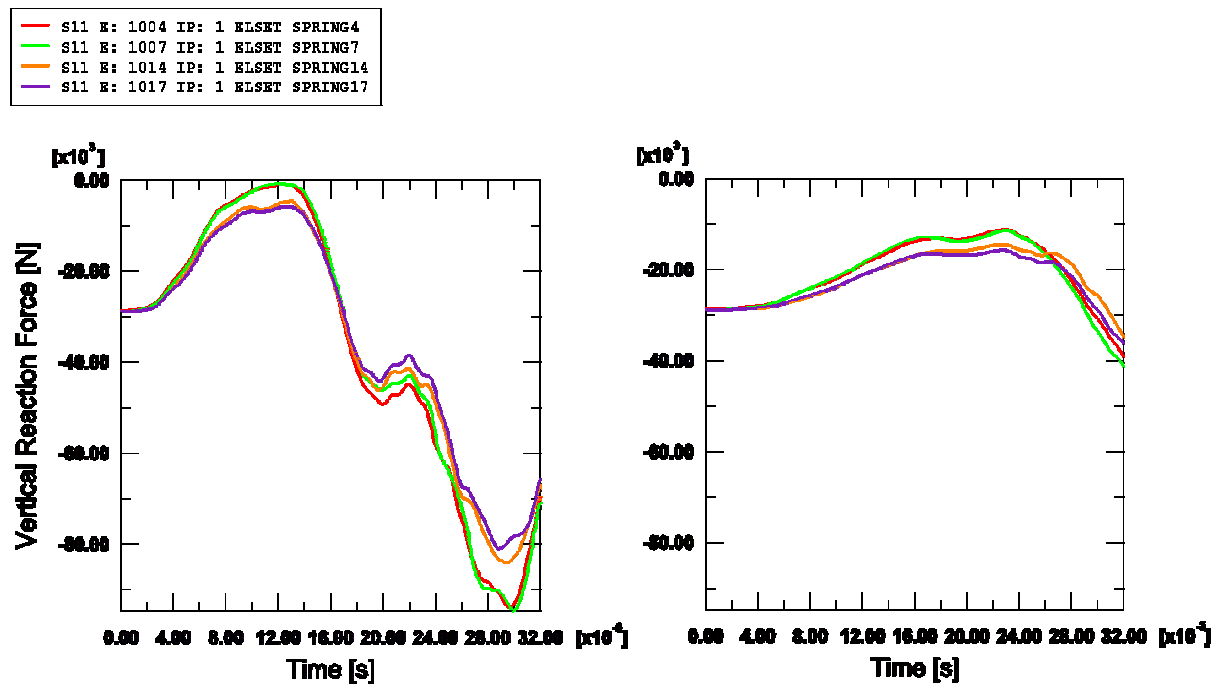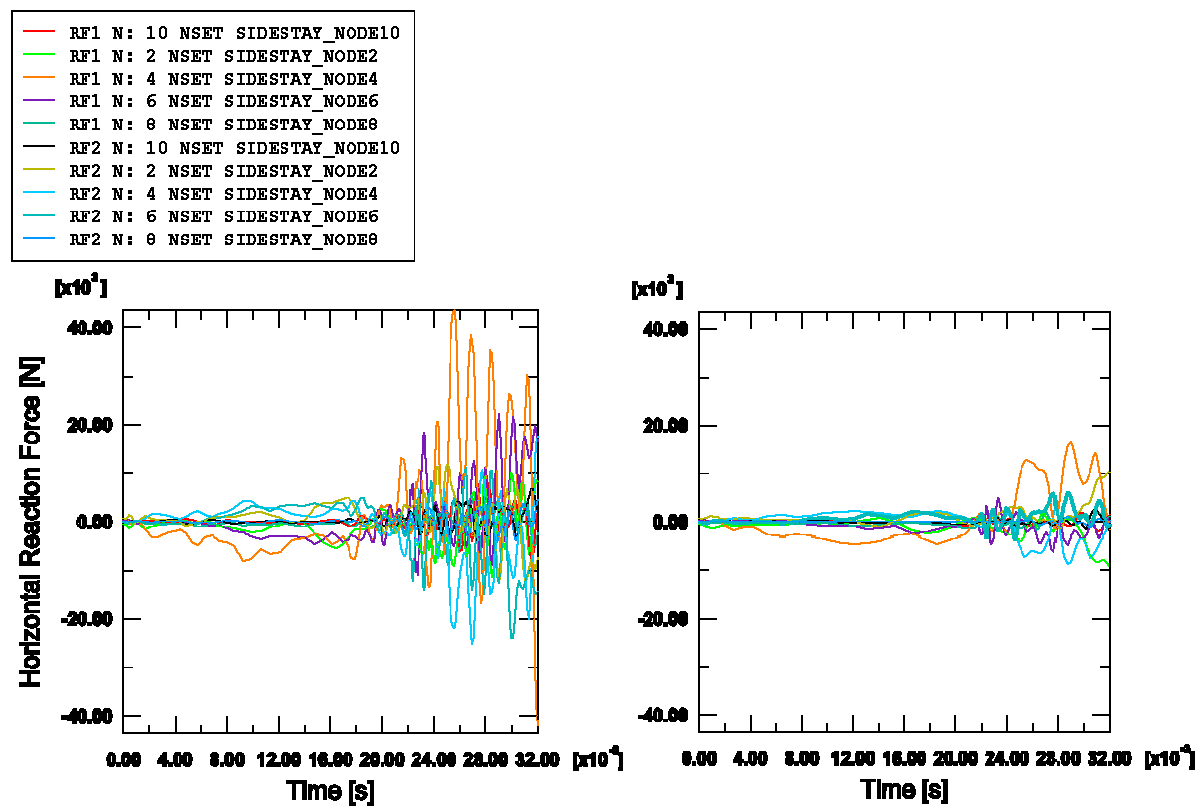

Figure 44. Horizontal reaction force components in the side stays as a function of time. Case 1 on the left, Case 2 on the right. Maximum reaction force component is approximately 44 kN (Case 1).

Figures 45 and 46 show the hoop and axial stresses at the centre of the pool bottom rounding. Hoop stresses are compression at over pressure, and they are higher by magnitude in the outer wall. Hoop stress in the outer wall is initially approximately 50 MPa (compression) and maximum is approximately 208 MPa (compression) at the time of the highest pressure peak. Figure 46 shows the corresponding axial stresses. Initially approximately 50 MPa tension in the inner wall and 50 MPa compression in the outer wall, a maximum stress of 209 MPa (compression) occurs in the outer wall at the time of the pressure peak. Stress curves for locations 1 and 3 (see Fig. 24 in Chapter 5.4) are qualitatively similar to Figures 45 and 46. The yield stress of the material is 200 MPa. The frequencies of the stress fluctuations estimated from the curves are approximately 140 Hz for Case 1 and 70 Hz for Case 2, which are equal to the frequencies estimated for the vertical motion of the pool bottom (see Fig. 40).

Figures 47 and 48 show the effect of the springs on the vertical reaction forces under the supports (notice the reverse direction definition in Case 3) and on the stresses at the rounding. The maximum reaction force in Case 3 is approximately 302 kN, while the reaction forces due to the mass of water alone are only about 28 kN. This in part illustrates the magnitude of the calculated pressure peak. It can be noted that the springs make a great difference on frequency and amplitude of the force fluctuations in the supports, but have very little effect on frequency and amplitude of the rounding stresses. The effect of the springs on the stresses might be somewhat larger if fluid-structure interaction was accounted for.

The stresses in the vertical support are examined by Calonius et al. (2003). Compressive maximum stress in the support due to the force of 302 kN would be approximately 220 MPa.
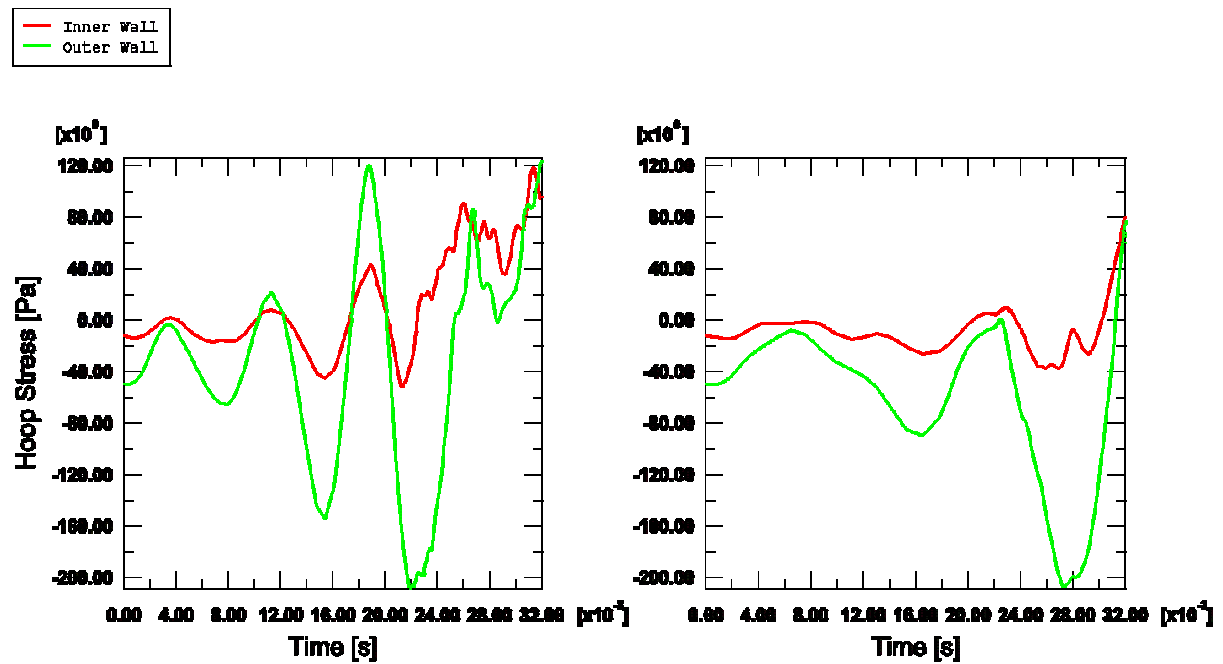
Figure 45. Hoop stresses in the pool bottom rounding as a function of time. Case 1 on the left, Case 2 on the right. Initially compression on both sides of the wall. Maximum magnitude is approximately 208 MPa (compression) in the outer wall in Case 1.
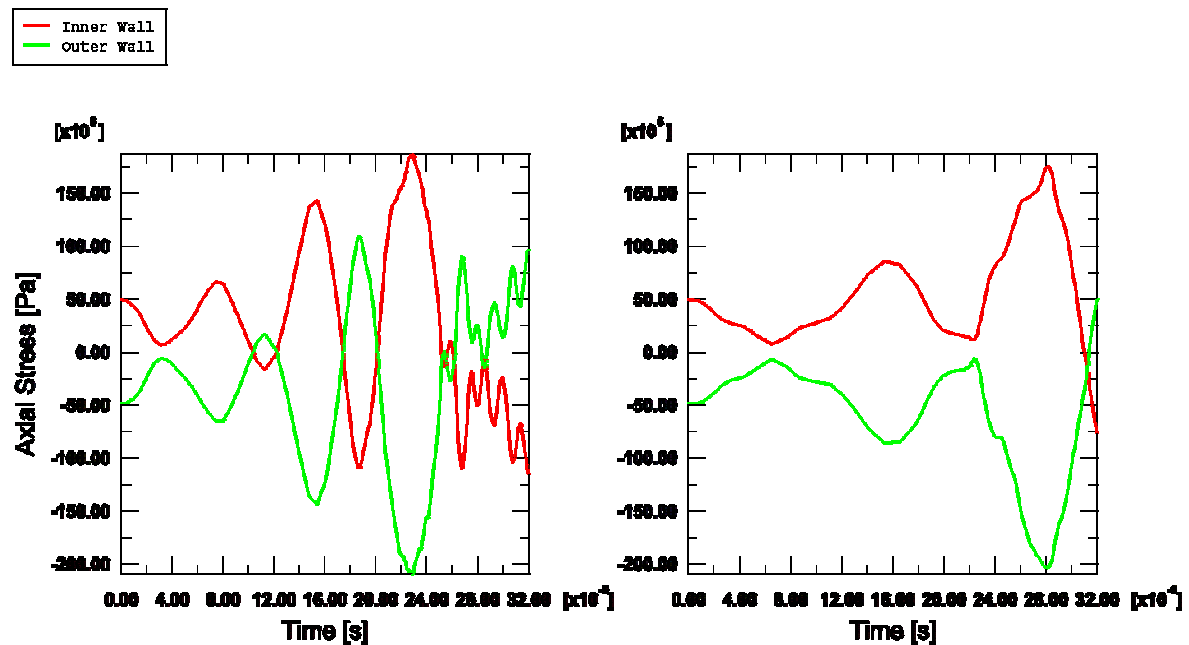
Figure 46. Axial (meridian) stresses in the pool bottom rounding as a function of time. Case 1 on the left, Case 2 on the right. Initially tension in the inner wall, compression in the outer wall. Maximum magnitude is approximately 209 MPa (compression) in the outer wall in Case 1.

Figure 47. Vertical reaction forces under the vertical supports as a function of time. Case 1 on the left, Case 3 (no springs) on the right. Maximum reaction force in Case 1 is approximately 95 kN and in Case 3 approximately 302 kN. Notice the reverse direction definition in Case 3.
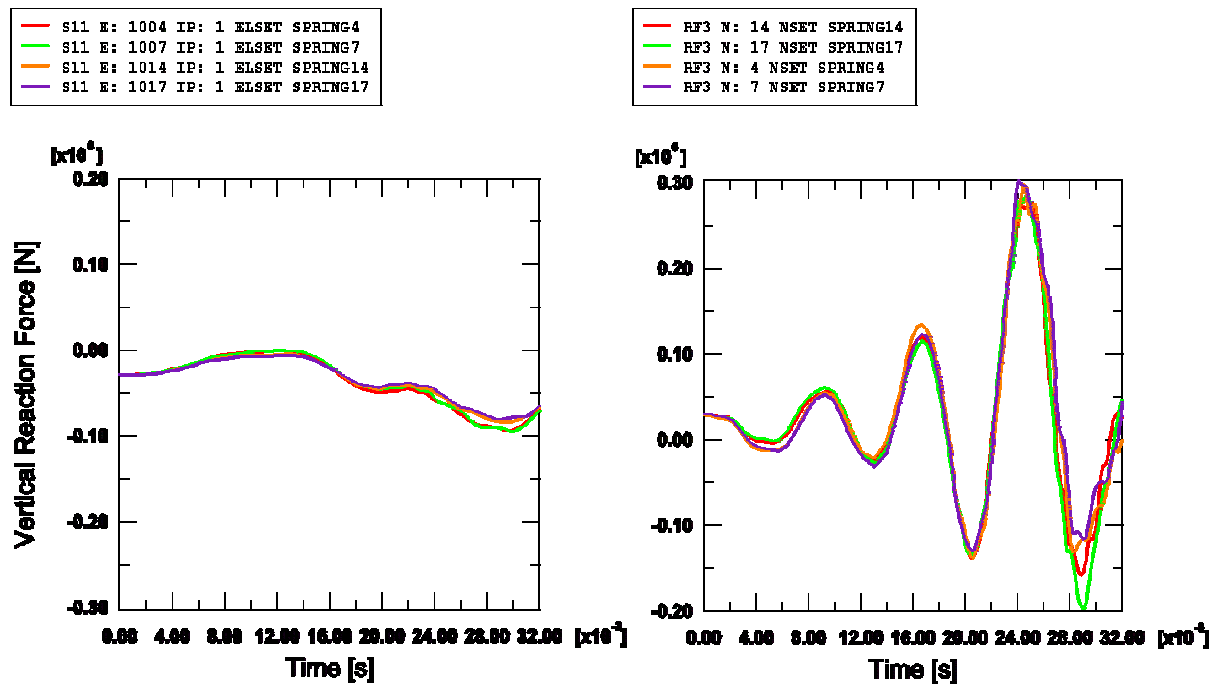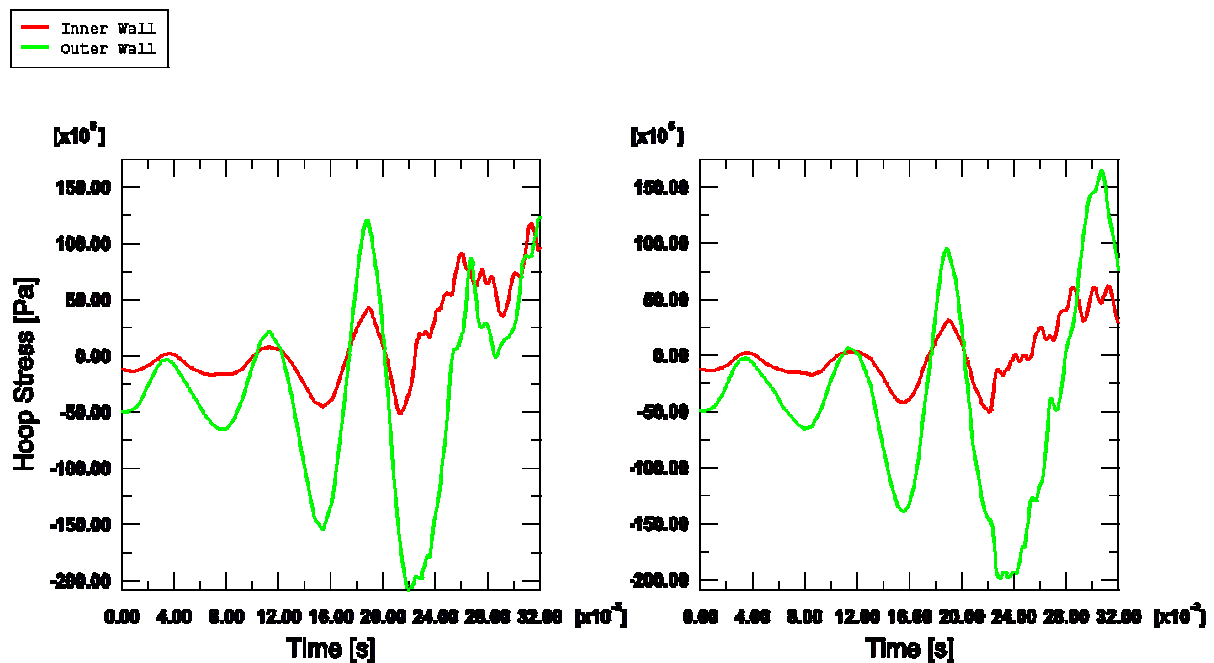

Figure 48. Hoop stresses in the pool bottom rounding as a function of time. Case 1 on the left, Case 3 (no springs) on the right.

6 Bi-directional Fluid-structure Interaction

Typically, as also in this work, the CFD analyses are carried out with rigid boundaries of the fluid domain. However in reality, the deformations of the flexible boundaries due to the pressure load affect the flow or pressure field. In order to predict realistically the structural response in cases where the deformations are relatively large, modelling of the fluid-structure interaction (FSI) is necessary. In this project, Star-CD is used for the flow analyses and ABAQUS for the structural problems. In the following, different alternatives for solving fluid-structure interaction problems are considered for these programs.

6.1 MpCCI Library

A common method for FSI is to couple CFD and FE codes during analyses. The Mesh-based parallel Code Coupling Interface (MpCCI) library written at the Fraunhofer Institute (MpCCI Team, 2002a; 2002b) employs this method. The MpCCI library has been built on top of the MPI Message Passing Standard (Snir et al., 1996), which defines the interfaces for sending and receiving messages between two computer programs. In practise, the MpCCI has to be used with the portable MPICH (Gropp and Lusk, 1996) implementation of the MPI standard.

The advantage of MpCCI is that the full properties of the two coupled analyses codes can be used. Therefore, one can take advantage of the full capabilities of both the fluid dynamics and the structural analyses codes, which enables accurate description of the physical phenomenon.

The MpCCI library enables, in principle, coupling of two mesh based codes, such as CFD and structural analyses codes (Ahrem and Krüger, 2000). The codes exchange coupling data, such as pressure, velocity and temperature on a meshed coupling surface. MpCCI provides tools for interpolation of the coupling data from the mesh of the sending code to the mesh of the receiving code. Bi-directional coupling of the codes via a moving coupling surface is also supported by MpCCI. Each code performs its usual iterations during the simulation. The CFD code sends the load on the coupling surface to the structural analyses code. The structural analyses code resolves the deformation of the structure and passes the result to the CFD code. Then, the cycle is repeated.

Most important vendors of the commercial CFD and structural analyses codes have been working on coupling their codes by using the MpCCI library. The CFD codes include CFX-5, FLUENT and Star-CD. The structural analyses codes include ABAQUS, ANSYS and MSC.Marc (Anon., 2001, 2002). Experiments have been performed on coupling CFX with the MSC/Marc (Menter, 2001) and with ANSYS (Kuntz, 2002) structural analyses codes. FLUENT has been coupled with ANSYS, where ANSYS was used for solving magnetic fields and FLUENT for calculating the plasma flow (Stammberger, 2001). Star-CD has been coupled with the PERMAS structural analyses code (Wintergerste, 2001). Some support on MpCCI is expected in the next commercial version Star-CD 3.2, which is released in the end of year 2003 (Larriau, 2002).

In the present work, MpCCI has only been used for one-directional coupling of Star-CD and ABAQUS. In bi-directional coupling, it would be necessary to move the CFD mesh by using Pro-Star, the pre-processor of Star-CD. This is done routinely in simulations of diesel engines where the moving piston is modelled. In these simulations, however, the motion of the piston is pre-determined. The motion of the piston is implemented by using the macro language of Pro-Star.

6.2 ES-FSI

Another alternative for coupling CFD and structural analyses codes is the ES-FSI code developed by CD adapco Group. ES-FSI is run together with the Star-CD code, and additionally an FE code is used for pre- and post-processing. The ES-FSI method is limited to problems, where the structure has linear material and geometric behaviour. ES-FSI can be used together with at least Permas, ANSYS and Nastran FE codes, but so far it has been unable to exchange data with ABAQUS. The analyses with ES-FSI can be divided into three basic steps, *pre-processing*, *analyses* and *post-processing*.

In *pre-processing*, the structural and fluid flow meshes, which need not to be fully compatible, are formed. The nodes of the structural model lying on the coupling surface, and possibly certain other nodes, are defined as Master Degrees Of Freedom (MDOF). A substructure analyses is performed by using the FE code to calculate reduced structural model matrices, which relate only the displacements of the MDOF. These reduced matrices are sent from the FE code to ES-FSI.

The *analyses* consist of moving mesh Star-CD analyses. The load calculated with Star-CD is used for moving the CFD mesh by using the structural information obtained from the pre-processing. The mesh is moved by the ES-FSI with the aid of the Pro-Star pre-processor of Star-CD. The ES-FSI is implemented as the user defined subroutine POSDAT in Star-CD. The displacements of the MDOF due to the pressure load are solved during the analyses. Since the structural problem is linear, the extra computational cost due to this is relatively small. Once the MDOF displacements at a given time step are computed, an interpolation method is used to calculate a new shape for the CFD surface mesh. The internal mesh is then revised accordingly. The flow field and pressure are solved again at the next time step, and the cycle is repeated.

In the final *post-processing* step, the FE code is used for solving the strains, stresses, etc. in the structure through time. Output from ES-FSI to be read by the FE code can be the displacements of the MDOF or wall pressures. If the pressures are read, standard dynamic FE analyses may be conducted. The frequency at which these data are written during the CFD analyses is specified by the user.

6.3 Direct Coupling of Star-CD and ABAQUS

Implementing direct coupling between Star-CD and ABAQUS will be possible in near future (Clerides, 2003). This would mean running Star-CD simultaneously preferably in the same computer. The structural analyses would be performed at each time step or at certain intervals during the CFD analyses by running ABAQUS. At the moment it is unclear, whether the same mesh should be used both in the CFD and structural analyses on the coupling surface.

6.4 Comparison of the Coupling Methods

The advantage of MpCCI is that it is not limited to linear structural problems. If the deformations are large, it will however be necessary to perform re-meshing, which is not yet supported by MpCCI. The implementation based on message passing between the CFD and structural analyses code also allows running the codes on different computers. This property has not, however, been tested in the experiments performed with MpCCI, and it is not clear

that it would work in the present environment where several firewalls separate the computers. On the contrary, it was observed that in a multiprocessor workstation the message passing failed when the computer was loaded with several other CPU intensive processes. The library is also fairly complicated, and some familiarity with the MPI standard is necessary for using it. An additional disadvantage is the extra license needed for using MpCCI.

Apparently, the direct coupling of Star-CD and ABAQUS would have the same advantages as using the MpCCI library. The analyses is not limited to linear structural problems, but presumably the changes in the CFD mesh can not be very large. Another advantage may be avoiding the extra licence fee of MpCCI or ES-FSI. The disadvantage is the need to perform the analyses simultaneously on the same computer.

The main advantage of ES-FSI is that the analyses can be split into three separate stages, which can be performed separately on different computers and at different times. This allows more flexibility for executing the analyses. The approach is also computationally less costly than the full nonlinear analyses. The main disadvantage is the limitation to linear structural problems. For the present task this is not, however, considered too restrictive. Another disadvantage is the extra license needed for ES-FSI.

Collaborative work with CD adapco Group has been initiated, in which an ABAQUS compatible implementation of ES-FSI is realised and the new implementation is verified against the experiments at Lappeenranta University of Technology. The condensation induced water hammer analysed in this report is used as the test case. In order to allow ABAQUS usage, ES-FSI is extended to exchange data with ABAQUS.

7   Analyses of Experiments

A set of preliminary tests with steam has been performed in the POOLEX project at Lappeenranta University of Technology. The tests have been carried out to investigate the capabilities of the test rig and the needs for the instrumentation. So far the steam generator pressures from 2 to 20 bar have been used. Steam has been blown into water through two different blow down pipes, DN80 (88.9x2.0 mm) and DN100 (114.3x2.0 mm). The sampling rate for most of the measured quantities in these tests was only 20 Hz per signal, which is clearly too low for the examined phenomenon.

Some results from the experiments are presented in this chapter. The results are from a test case where the steam generator pressure was 20 bar and the blow down pipe was DN80. Water level in the pool was 3.78 m, i.e., nearly a meter higher compared to the simulations. Measurement instrumentation and the results are discussed in more detail in Laine (2003).

7.1 Visual Data

Two 25 fps video cameras were used to gather visual data of the phenomenon inside the pool. As the injection of steam was initiated, the water plug inside the blowdown pipe was expelled from the pipe. This caused visible vibrations to the pool structures. During the first 520 seconds as the steam flow rate was high, the condensing of the steam at the pipe outlet was smooth. The steam jet formed a stationary conical pattern at the pipe outlet. The chugging phenomenon started after 520 s, and steam bubbles began to form at the pipe outlet. The collapsing of the bubbles at the pipe outlet appeared as instantaneous. The diameters of the

bubbles were approximately two times the diameter of the blowdown pipe. Some steam bubbles forming at the pipe outlet during the chugging phenomenon can be seen Figure 49, the images are from period 1370-1450 s. (Laine, 2003)
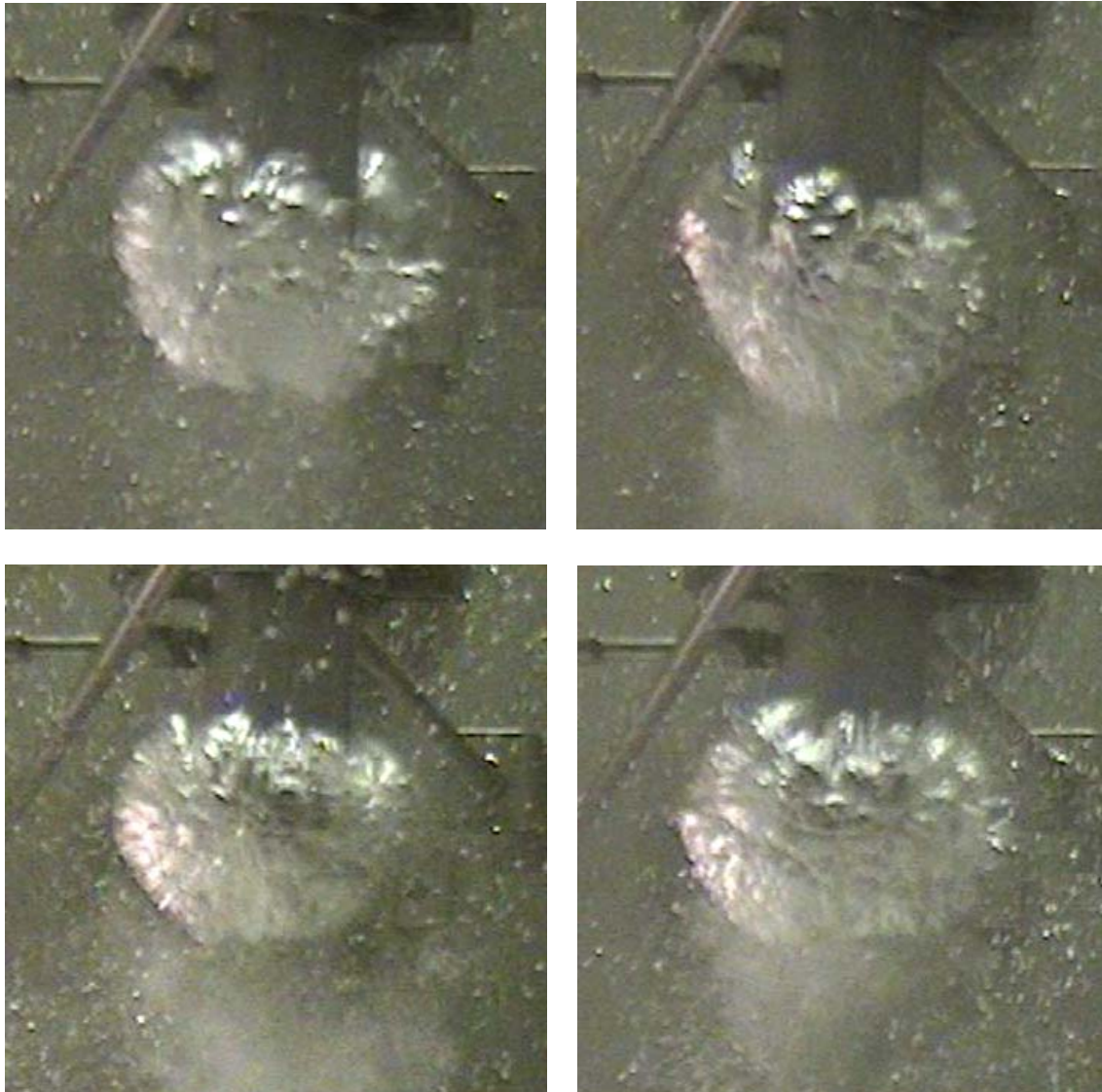
Figure 49. *Steam bubbles forming at the blowdown pipe outlet during a steam blow test.*
Laine (2003)

7.2 Pressure Measurements

Three pressure transducers were used to measure absolute pressure inside the blowdown pipe. Two transducers were also used at the pool wall and inside the pool at the level of the blowdown pipe outlet. Figure 50 shows the measured pressures as a function of time. The readings of P1, P2 and P3 (inside the blowdown pipe) start to oscillate after 520 s due to the chugging phenomenon. The maximum amplitude of the pressure fluctuations inside the pipe during the chugging phenomenon is approximately 50 kPa. Transducers P4 and P5 (inside the pool) show small oscillations at the start of the test as the water plug is expelled from the blowdown pipe. The maximum amplitude is 10 kPa. These oscillations die away after five seconds. During the chugging phenomenon the maximum amplitude of P4 and P5 is 5 kPa. (Laine, 2003)

Figure 50. Pressures inside the blowdown pipe and inside the pool as a function of time in a steam blow test (P1, P2, P3 = inside the blowdown pipe; P4 = at the pool wall at the level of the blowdown pipe outlet; P5 = inside the pool at the level of the blowdown pipe outlet). (Laine, 2003)

7.3 Strain Measurements

Four strain gages were used at the outer wall some centimetres above and below the bottom rounding to measure the hoop and axial strains (locations 1 and 3 in Fig. 24). A thermocouple was also used to measure the temper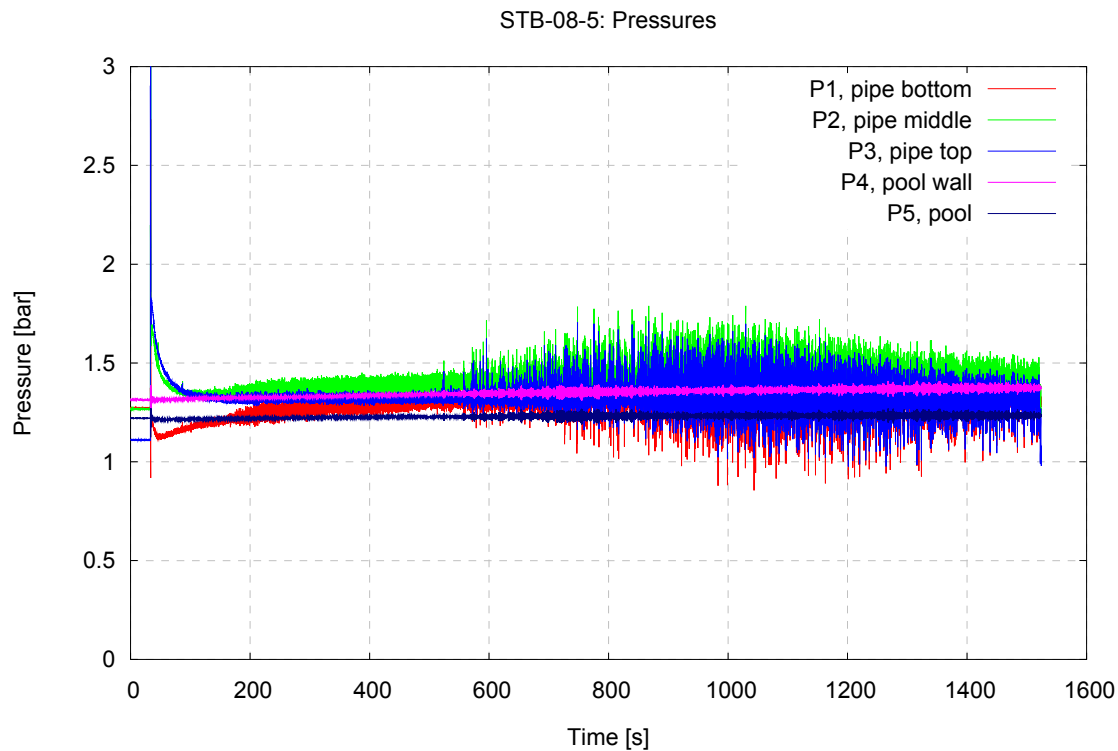ature of the pool outer wall near the strain gages. Figure 51 shows the strains and pool wall temperature as a function of time. The strain gages were set to zero after the pool had been filled, thus the initial strains are due to temperature rise before the test start. A maximum amplitude of 75 μm/m was measured by strain gage ST3 (below rounding, hoop direction) at the start of the blowdown as the water plug hit the pool bottom. The oscillations due to the first hit die away in about five seconds. The rise of the strains during the test is mainly explained by the temperature rise of the pool outer wall. The temperature of the wall rose from 28°C to 51°C during the test. During the chugging phenomenon (after ~500 s, see Fig. 51) the maximum amplitude was approximately 50 μm/m, again measured by ST3. (Laine, 2003)

The strain amplitude 75×10^{-6} corresponds to approximately 15 MPa of stress. The results with the dense mesh presented in Chapter 5.4 show that with hydrostatic pressure the maximum hoop stress (at the centre of the rounding) in the outer wall is approximately twice the hoop stress at the location of the strain gage ST3. Also, maximum von Mises stress at the rounding is approximately three times the hoop stress at the location of the strain gage ST3. According to these values together with a rough linear approximation the maximum von Mises stress amplitude at the rounding during the test could be about 45 MPa. The maximum von Mises stress at the rounding with hydrostatic pressure corresponding to the water level

3.78 m is approximately 120 MPa. A repeated loading, where the mean value is 120 MPa and the amplitude is 45 MPa, is notable for the pool wall. Strain gage ST3 measured a maximum strain amplitude of 50×10^{-6} when the chugging phenomenon occurred. This corresponds to approximately 10 MPa of stress. Thus the corresponding repeated loading during the chugging phenomenon could be about 120 ± 30 MPa by the same approximation.

The frequency of the strain gage signals at the beginning of the test is approximately 10 Hz, this can be seen in Figure 52. Accordingly the number of cycles during the chugging phenomenon in the test could be approximately 10 000. The curves in Figure 52 however show signs of aliasing due to the too low sampling rate (20 Hz) of the measurements. This means that the actual frequency and hence also the number of cycles could be in reality higher. Aliasing can produce results, in which the actual frequency of the investigated phenomenon is many times higher than the one calculated from the measured signal. In the dynamic FE analyses the frequency of the vertical motion of the pool bottom and the frequency of the stress fluctuations at the bottom rounding were approximately 140 Hz (Case 1, without mass of water) and 70 Hz (Case 2, mass of water included).

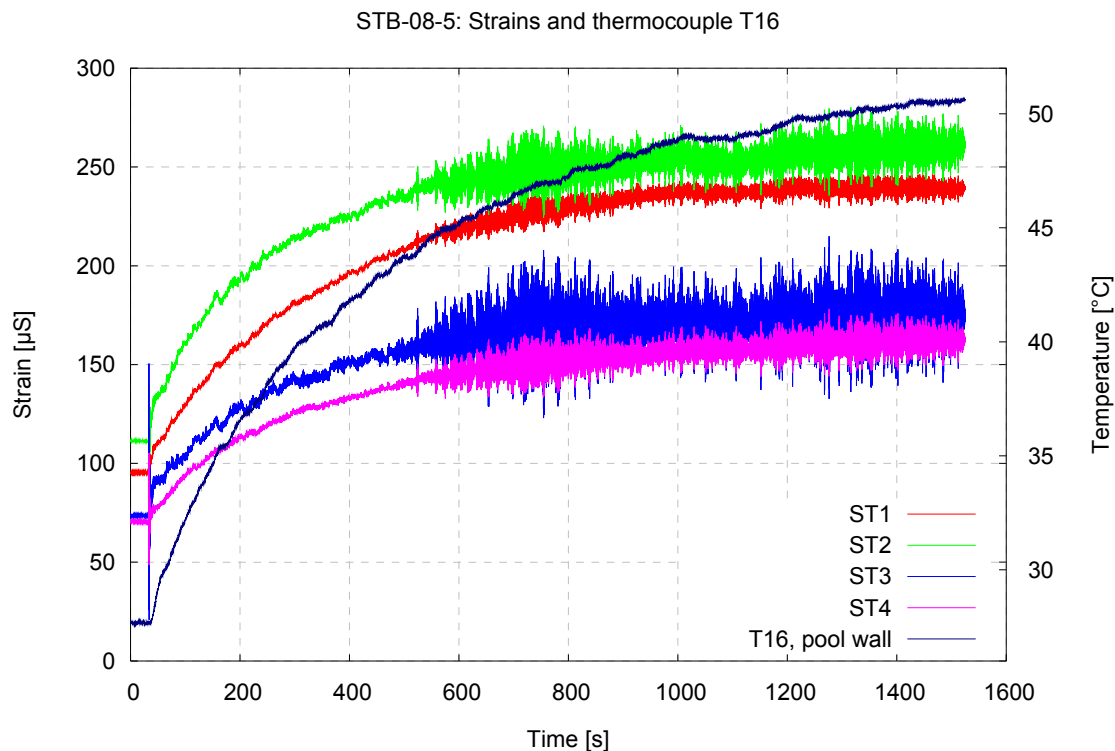*Figure 51. Strains ($\times 10^{-6}$) and pool wall temperature (°C) as a function of time in a steam blow test (ST1 = above rounding, hoop direction; ST2 = above rounding, axial direction; ST3 = below rounding, hoop direction; ST4 = below rounding, axial direction; T16, pool wall = pool wall temperature near the strain gages). (Laine, 2003)*
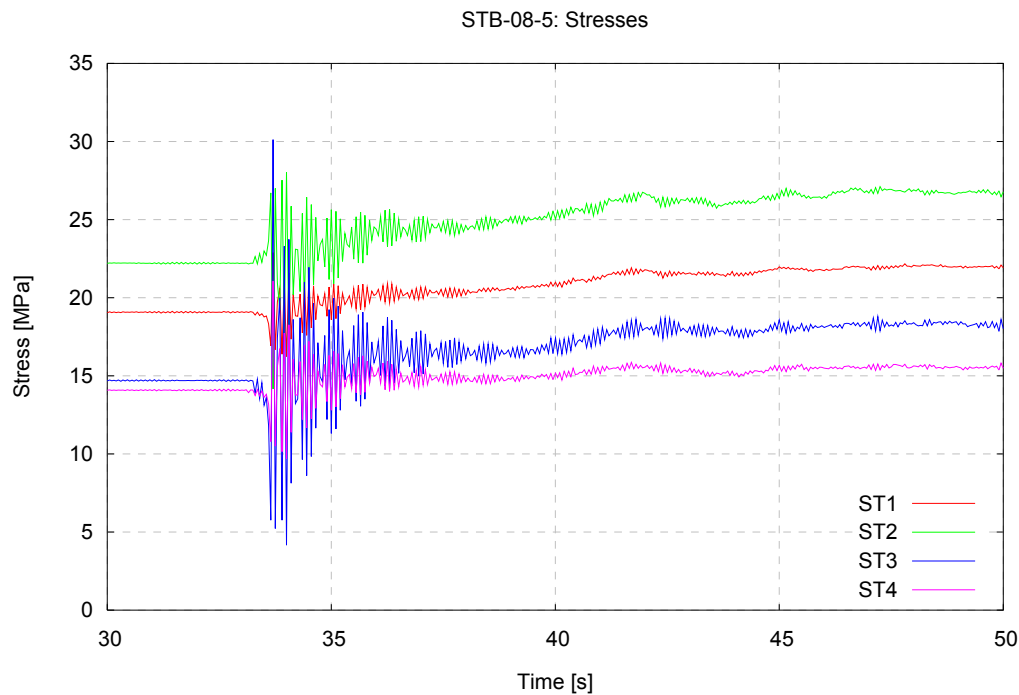
Figure 52. Stress values (MPa) calculated from strain gage readings in period 30 - 50 s in a steam blow test (ST1 = above rounding, hoop direction; ST2 = above rounding, axial direction; ST3 = below rounding, hoop direction; ST4 = below rounding, axial direction). (Laine, 2003)

7.4 Displacement Measurements

The horizontal and vertical movements were measured at two opposite locations at the top of the pool. An optical system, where the movements are registered on a video camera, was used. The maximum displacements were few millimetres and they were detected at the start of the test as the water plug hit the pool bottom. After about five seconds the oscillations due to the first hit died away. The movements during the rest of the experiment, including the period of the chugging phenomenon, stayed too small to be measured accurately with the present system. The measured maximum displacements are of the same order as the ones presented in FE results, but they are due to a different phenomenon, i.e., a water plug hit in the experiments and a water hammer induced by a condensing steam bubble in the simulations. (Laine, 2003)

8 Summary and Conclusions

The structural effects caused by the water hammer induced by a large condensing steam bubble were examined with single-phase CFD calculations and structural analyses. The CFD and structural analyses were coupled one-directionally, i.e., the motion of the pool wall was not taken into account in the CFD calculations. In the CFD calculations, the rapid collapse of a steam bubble with a diameter of 20 cm was considered. The collapse was modelled with a mass sink determined from the potential theory for incompressible fluid. The collapse time of the bubble was about 25 ms. In the water hammer initiated by the collapse, the maximum pressure on the pool wall was about 300 kPa, and the load lasted about 0.4 ms.

In the present CFD analyses, it was assumed that the diameter of the bubble is 20 cm, which is roughly equal to the size found by Laine et al. (2003) in the preliminary experiments with steam. This is not, however, the maximum size for the bubbles that can occur in the experiments as can be seen from earlier experiments performed with air by Laine et al. (2002), where air bubbles with a diameter of about 1.3 m were observed. Rapid collapse of a so large bubble could lead to much higher loads than was found in the present analyses. The loads caused by bubbles with larger diameter than 20 cm could not be calculated with the present method, where a single-phase model was used. In the under pressure stage of the collapse, it would be necessary to take into account the cavitation occurring in the low pressure regions of the pool.

In addition to the bubble size, the pressure difference causing the collapse of the bubble is another important parameter of the present CFD analyses because it determines the collapse time of the bubble. It was assumed that the pressure difference is $\Delta p_B = 12.5$ kPa, which lead to the collapse time of about 25 ms. According to the analytical results, the collapse time is inversely proportional to the square root of the pressure difference. Therefore, a larger pressure difference of $\Delta p_B = 125$ kPa would lead to a collapse time of only 9 ms. A smaller pressure difference of $\Delta p_B = 1.25$ kPa would lead to a collapse time of about 80 ms. Presently, the pressure difference has to be estimated from the collapse times observed in experiments for different pool temperatures and steam flow rates and properties.

The structural effects caused by the condensation induced water hammer were examined with different FE analyses. The stresses of the pool wall exceeded the yield point and some plastic deformation took place. The maximum von Mises stresses during the analyses were approximately 210 MPa. They were expectedly located at the rounding between the pool cylinder wall and the end plate. In the case of mere hydrostatic pressure, the maximum stress was approximately 70 MPa. Thus, the calculated pressure transient had a significant structural effect. The maximum equivalent plastic strain at the end of the analyses was approximately 0.226 %. The stress fluctuations in the pool wall corresponded to the pressure load at some degree, despite the fact that the frequency of the pressure load was very high compared to the decisive eigenfrequency of the structure. Maximum stress at the location of the welded seam of the rounding was approximately 180 MPa and around the welded plates approximately 120 MPa. Based on these values, the welds, where there are discontinuity, more material defects and residual stresses, are also critical locations in case of repeated loading having the same pressure amplitude. Mesh sensitivity studies showed that the presented stresses at the rounding should be scaled up, the presented maximum von Mises stresses should be scaled up by approximately 32 %. Accordingly, plastic deformations would also be larger. It should be noted that the strain rate dependency of yield strength was not taken into account in the analyses.

The maximum compressive stresses in the vertical supports were not critical in spite of the high pressure peak. The springs under the supports had a great effect on these stresses because the maximums were approximately 70 MPa with the springs and 220 MPa without them. The forces in the five side stays were not critical in terms of the beam cross section. However, the real side stays consist of nested profiles with modest welds, which were not analysed.

The addition of mass of water to the pool wall had a significant effect on the structural response in these analyses. This is due to the rapid variation of the pressure load. The amplitudes and frequencies of the structural response were higher without mass of water. The motion of the pool wall was small and localised, i.e., no swaying of the pool occurred. In this sense the model with the added mass could be a less accurate approximation. The largest

displacements were approximately 4 mm without mass of water and they occurred at the bottom of the pool (vertical) and at the top of the pool (horizontal).

According to the strain gage measurements and a rough approximation, the maximum von Mises stress amplitude at the bottom rounding in the preliminary steam blow tests could have been approximately 45 MPa. The mean value at corresponding location with the water level used in the tests is approximately 120 MPa, thus the maximum stress could have been 165 MPa. Based on these values the pool might not withstand much higher water level or stronger pressure peaks without clear plastic deformation. The repeated loading during the chugging phenomenon could have been approximately 120 ± 30 MPa by the same approximation. These values and the approximation presented in Chapter 7.3 can be used in estimating need of fatigue analyses in case of higher loadings.

In the future experiments, strains should also be measured at a few locations at the centre of the rounding for better resolution of the structural response and monitoring of the maximum stresses. The strains due to hydrostatic pressure should also be measured for comparison of the experimental and numerical results. In CFD modelling, accurate data of the sizes and collapse times of the steam bubbles would be essential.

In future work, fluid-structure interaction will be taken into account with the ES-FSI code together with Star-CD and ABAQUS. Possibilities of using multiphase models in the CFD analyses will be tested. The structural model will be revised according to the real structure in the future tests. The pool mesh will be refined at the bottom and at the welds for better accuracy and valid comparison of the strain gage measurements.

References

ABAQUS Theory Manual. 2002.Version 6.3. Hibbit, Karlsson & Sorensen Inc. RI.

Abramowitz, M. and Stegun, I.A., 1972. Handbook of mathematical functions, Dover Publications, New York, p. 258.

Ahrem, R. and Krüger, M., 2000. Simulationen koppeln mit MpCCI, GMD-Spiegel 1–2, p. 32–34.

Anon., 1977. Description of the test facility. The Marviken full scale containment experiments, second series, Marviken, Sweden, Report MXB-101.

Anon., 2001. MpCCI 2nd User Forum, February 8th, 2001, Book of abstracts.

Anon., 2002. MpCCI 3rd User Forum, February 27–28, 2002, Book of abstracts.

Antony-Spies, P., 1979. Bubble collapse and fluid structure interaction, Transactions of the American Nuclear Society, 31, p. 87–89.

Calonius, K., Pättikangas, T. and Saarenheimo, A., 2003. Numerical analyses of a water pool under loading caused by large air and steam bubbles, VTT Industrial Systems, Project Report BTUO72-031106, Espoo, Finland, 43 p.

Clerides, D., 2003. Personal communication.

Davidson and Schüler, 1960. Bubble formation at an orifice in an inviscid liquid. Trans. Inst. Chem. Engrs. 38, 335-342.

Giencke, E., 1979. Pressure distribution due to steam bubble collapse in a BWR suppression chamber, Transactions of the 5th international conference on structural mechanics in reactor technology, Berlin, Germany, 13–17 August, 1979, B 7/1.

Giencke, E., 1981. Pressure distribution due to a steam bubble collapse in a BWR pressure suppression pool, Nuclear Engineering and Design 65, p. 175–196.

Gong, E.Y., Alexander, E.E., McMaster, W.H. and Quinones, D.F., 1979. PELE-IC Test Problems. UCRL-52835.

Gropp, W. and Lusk, E., 1996. User's guide for *mpich*, a portable implementation of MPI, Argonne National Laboratory, Mathematics and computer science division, ANL/MSC-TM-ANL-96/6.

Huber, P.W., 1979. 1st international seminar on fluid-structure interaction in LWR systems, Berlin, Germany, 20–21 August, 1979, p. 89–100.

Kuntz, M., 2002. Code coupling with CFX software, in MpCCI 3rd User Forum, February 27–28, 2002, Book of abstracts, p. 8.

Laine, J., 2002. Condensation pool experiments with non-condensable gas, Lappeenranta University of Technology, Research Report TOKE-2/2002, 46 p. + app. 14 p.

Laine, J., 2003. Condensation pool preliminary experiments with steam, Lappeenranta University of Technology, Research Report POOLEX-04/2003, 24 p. + app. 7 p. (To be published.)

Lamb, H., 1975. Hydrodynamics, sixth edition, Cambridge University Press, p. 122.

Landram, C.S., 1982. Steam chugging calculations with the PELE-IC code. Nuclear Engineering and Design 70, p. 411-421.

Larriau, L., 2002. Star-CD and MpCCI, in MpCCI 3rd User Forum, February 27–28, 2002, Book of abstracts, p. 10.

McMaster, W. H. and Gong, E.Y., 1979. User's Manual for PELE-IC: A Computer Code for Eulerian Hydrodynamics. UCRL-52609.

McMaster, W.H., Gong, E.Y., Landram, C.S., and Quinones, D.F., 1981. Fluid Structure Coupling Algorithm,Computers and Structures, Vol. 13, pp. 163-166, NESC0865/01.

McMaster, W.H., Norris Jr. D.M., Goudreau, G.L., Quinones, D.F., Gong, E.Y., Moran, B. and Macken, N.A., 1979. Coupled Fluid-Structure method for Pressure Suppression Analysis, NUREG/CR-0607.

Meier, M., 1999. Numerical and experimental study of large steam-air bubbles injected in a water pool. Dissertation ETH no 13091, ETH, Zürich, Switzerland. URL: http://www.lkt.mavt.ethz.ch/~meier/work.html.

Menter, F., 2001. Fluid-structure interaction with CFX, in MpCCI 2nd User Forum, February 8th, 2001, Book of abstracts.

Moody, F.J., 1986. Dynamic and thermal behavior of hot gas bubbles discharge into water. Nuclear Engineering and Design 95, pp. 47–54.

MpCCI Team, 2002a. Mesh-based parallel Code Coupling Interface, User's guide of MpCCI version 1.3, Fraunhofer Institute for Algorithms and Scientific Computing, Sankt Augustin, Germany, 27 p.

MpCCI Team, 2002b. Mesh-based parallel Code Coupling Interface, Specification of MpCCI version 1.3, Fraunhofer Institute for Algorithms and Scientific Computing, Sankt Augustin, Germany, 125 p.

Nichols, B.D. and Hirt, C.W., 1979. Hydroelastic phenomena in boiling water reactor suppression pools, Transactions of the 5th international conference on structural mechanics in reactor technology, Berlin, Germany, 13–17 August, 1979, B 7/2.

Pättikangas, T., Raussi, P., Pokela, H. and Huttunen, M., 2000. Two-dimensional CFD simulation of water hammer in a pool, VTT Energy, Research Report ENE6/26/00, Espoo, Finland, 22 p. + app. 4 p.

Pättikangas, T. and Pokela H., 2003. Wall-loadings caused by large air bubbles injected in a water pool, VTT Processes, Project Report PRO4/T7534/02, Espoo, Finland, 28 p.

Raussi, P., 2001. Behaviour of steam bubbles in a condensation pool, VTT Energy Reports 35/2001, Espoo, Finland, 17 p.

Saarenheimo, A., Calonius, K., Pättikangas, T., Raussi, P. and Pokela H., 2000. Numerical analyses of axisymmetric structures under water hammer loading. VTT Manufacturing Technology, Research Report BVAL64-011091, Espoo, Finland, 34 p.

Sargis, Stuhmiller and Wang, 1978. A Fundamental Thermal Hydraulic Model to Predict Steam Chucking Phenomena", Proceedings of ASME 1978 Winter Meeting. Topics in Two-Phase Heat Transfer and Flow, pp.123-133.

Silde, A. and Pättikangas, T. D2A version 1.0, 2001. Interface between the DET3D and ABAQUS codes, VTT Energy, Report ENE4-PD-3/01, 5 p. + app. 27 p.

Snir, M., Otto, S., Huss-Lederman, S., Walker, D., Dongarra, J., 1996. MPI: The complete reference, MIT Press, Cambridge, Massachusetts.

Stammberger, H., 2001. Coupling for arc simulations at MOELLER, in MpCCI 2nd User Forum, February 8th, 2001, Book of abstracts.

Wintergerste, T., 2001. Fluid-structure interaction and the use of MpCCI at Sulzer, in MpCCI 2nd User Forum, February 8th, 2001, Book of abstracts.

Wood and Sun, 1980. Determination of Pressure Fields in a BWR Suppression Pool by Means of Green's Function and Comparison with Method of Images and a Finite Difference Solution. NED 61 153-161.

Appendix: Transfer of Pressure Loads from Star-CD to ABAQUS

Previously pressure loads have been transferred from Fluent and DET3D to ABAQUS by using the interpolation programme D2A, which interpolates the pressure or temperature loads from the CFD mesh to the structural analyses mesh. D2A is based on the Mesh-based parallel Code Coupling Interface (MpCCI) subroutine library, which enables coupling of two mesh based codes. In principle, MpCCI could also be used for bi-directional coupling of the CFD and structural analyses. In D2A, only one-directional transfer of the load from the CFD code to the structural analyses is implemented.

In D2A, the surface mesh of the CFD analyses ("cfd_mesh.neu") and structural analyses ("struct_mesh.neu") are needed as input. In addition, the pressure data written from the CFD analyses to the file "cfd_data.neu" is needed. The result of the interpolation is written in the file "abaqus_data.neu". In addition to D2A, one needs the subroutines that write the CFD data into the file "cfd_data.neu" in the proper format during the CFD analyses. These subroutines are specific to each CFD programme: Fluent, DET3D and Star-CD.

In this work, transfer of loads from Star-CD to ABAQUS was tested and improved. In the following, the necessary steps for transferring pressure loads from Star-CD to ABAQUS are summarised:

1. The common simulation geometry for Star-CD and ABAQUS should be defined in the Gambit meshing programme. Using the same geometry in the CFD and structural analyses is important for successful interpolation. The geometry of the coupling surface is transferred in the ACIS format from Gambit to ABAQUS. Using ICEM Hexa for meshing of the CFD model leads to difficulties in exporting the surface meshes needed in the interpolation.

2. The CFD model is meshed in Gambit. The mesh is then deleted except the mesh of the coupling surface, which is written in the file "cfd_mesh.neu".

3. The structural model is meshed and the mesh on the coupling surface is written in the file "struct_mesh.neu".

4. Star-CD simulation is performed by using the "posdat.f" user defined subroutine. During the first iteration, the surface mesh file "cfd_mesh.neu" is read. Conversion table between the numbering of the nodes and elements in Gambit and in Star-CD is done.

5. During the following iterations, the wall pressure at the Gambit wall elements is written into the file "pressure.dat" by using the conversion table.

6. After the Star-CD simulation, the interpolation programme D2A is compiled and linked with proper maximum numbers for nodes, elements, and time steps.

7. Interpolation is performed by running D2A. The files "cfd_mesh.neu", "struct_mesh.neu" and "pressure.dat" are used as input. The pressure load in the ABAQUS format is written in the file "abaqus_data.neu".

8. ABAQUS analyses is performed by using the load in the file "abaqus_data.neu".

Title	Numerical analyses of a water pool under loadings caused by a condensation induced water hammer
Author(s)	Antti Timperi, Timo Pättikangas, Kim Calonius, Jari Tuunanen, Juha Poikolainen & Arja Saarenheimo
Affiliation(s)	VTT Industrial Systems, Finland
ISBN	87-7893-154-1 *(Electronic report)*
Date	March 2004
Project	NKS_R_2002_01 (BTUO72-031198 VTT)
No. of pages	65
No. of tables	10
No. of illustrations	52
No. of references	40

Abstract	Three-dimensional simulations of a rapidly condensing steam bubble in a water pool have been performed by using the commercial computational fluid dynamics (CFD) code Star-CD. The condensing bubble was modelled by using a mass sink in a single-phase calculation. The pressure load on the wall of the pool was determined and transferred to the structural analyses code ABAQUS. The analyses were done for a test pool at Lappeenranta University of Technology.
	The structural integrity of the pool during steam experiments was investigated by assuming as a test load the rapid condensation of a steam bubble with a diameter of 20 cm. The mass sink for modelling the collapse of the bubble was determined from the potential theory of incompressible fluid. The rapid condensation of the bubble within 25 ms initiated a strong condensation water hammer. The maximum amplitude of the pressure load on the pool wall was approximately 300 kPa. The loads caused by the high compression waves lasted only about 0.4 ms. The loadings caused by larger bubbles or more rapid collapse could not be calculated with the present method.

Key words	Condensing steam bubble, structural analysis, Star-CD, ABAQUS